RICE UNIVERSITY

Photoassociative Spectroscopy of 87Sr

By

Joshua Cartwright Hill

A THESIS SUBMITTED
IN PARTIAL FULFILLMENT OF THE
REQUIREMENTS FOR THE DEGREE

Doctor of Philosophy

APPROVED, THESIS COMMITTEE

Thomas Killian

Thomas Killian
Dean, Wiess School of Natural Sciences
Professor of Physics and Astronomy

Randall G Hulet

Randall Hulet
Fayez Sarofim Professor of Physics and Astronomy

Matthew Jones
Assistant Professor of Chemistry and Materials Science and NanoEngineering

HOUSTON, TEXAS

April 2021

Rice University

Photoassociative Spectroscopy of ^{87}Sr

by

Joshua C. Hill

A Thesis Submitted
in Partial Fulfillment of the
Requirements for the Degree

Doctor of Philosophy

Approved, Thesis Committee:

Thomas C. Killian, *Chair*
Dean, Wiess School of Natural Sciences
Professor of Physics
and Astronomy

Randall G. Hulet
Fayez Sarofim Professor of Physics and Astronomy

Matthew R. Jones
Assistant Professor of Chemistry and
Materials Science and NanoEngineering

Houston, Texas
April 30, 2021

Abstract

Photoassociative Spectroscopy of ^{87}Sr

by

Joshua C. Hill

This dissertation describes experiments demonstrating photoassociation (PA) in samples of trapped ultracold fermionic ^{87}Sr atoms. The single-photon PA process utilized promotes pairs of ground-state atoms to bound states on the excited $^1\Sigma_u^+$ $5s^2\,{}^1\mathrm{S}_0$ - $5s5p\,{}^1\mathrm{P}_1$ molecular potential. Binding energies up to approximately 314 GHz red detuned from the atomic asymptote for a series of molecular states on the excited potential were fit with the semiclassical LeRoy-Bernstein model. Similar measurements and analysis were performed for the bosonic isotopes ^{84}Sr and ^{86}Sr, allowing a combined analysis of the long-range portion of the excited-state potential and determination of the $5s5p\,{}^1\mathrm{P}_1$ atomic state lifetime of 5.20 ± 0.02 ns. Additionally, PA resonance strengths are compared to predictions based on a reflection approximation and the ground-state wave function calculated using the known $^1\Sigma_g^+$ $5s^2\,{}^1\mathrm{S}_0$ - $5s^2\,{}^1\mathrm{S}_0$ ground potential.

Ultracold Sr gases are currently studied for a wide range of applications including precision metrology, quantum simulation of many-body phenomena, quantum information, and Rydberg physics. Despite this, no PA resonances had been reported in ^{87}Sr, and no PA resonances on the molecular potential employed in this work had been reported for ^{84}Sr.

These are the two isotopes most often used. This work enables accurate prediction of photoassociative transition frequencies and rates in these isotopes, and can inform experiments using PA spectroscopy as a probe of ^{87}Sr in optical lattices.

ACKNOWLEDGEMENTS

I am grateful to my many friends and colleagues at Rice for their support over the years. Their camaraderie, advice, leadership, and perspectives have taught me as much as any class or research project. The combined intellectual and social community at the university is unique, and I will miss it greatly. Valhalla and the Graduate Student Association have been twin pillars in my PhD experience, allowing me to meet an incredible diversity of other talented students, faculty, staff, and Rice community members. Participation in their activities (and occasional antics) were crucial to maintaining the stamina that earning a PhD demands; they overlaid a rich cyclicality atop the slow and unpredictable nature of research. Rice staff members have been valuable partners during this time, particularly those in Student Activities, the Center for Career Development, the Association of Rice Alumni, Graduate and Postdoctoral Studies, the Doerr Institute for New Leaders, and the Office of International Students and Scholars. These collaborations taught me a great deal about what is required to be successful beyond the laboratory. I am thankful for the unprecedented personal, professional, and leadership development opportunities Rice provides.

I am also grateful to Tom Killian for his long ranging research vision, and willingness to change it when things didn't work as planned. This broader-picture leadership is even more impressive when coupled with his

ability and willingness to help solve challenges at an impressively fine level of detail across multiple rooms brimming with hardware. I have benefited greatly from his attention to detail and insistence on precision when communicating. Past and present Killian lab members were also essential for generously sharing their deep knowledge and experience regarding the myriad topics necessary for conducting atomic physics research.

My somewhat circuitous route to graduate school via a GED and community college allowed me the opportunity to experience a broad range of mentorship and instruction styles. I am particularly grateful to the professors of Thomas Nelson Community College as well as William and Mary. They laid the foundations for my understanding of, and a large part of my interest in, the subjects that lead to this degree. I hope to remain in touch during a lifelong quest to better understand nature's beautiful nuances.

Finally, I want to thank my family for their unwavering support and inspiration [36] [37].

To my family

Contents

List of Figures

List of Tables

CHAPTER 1

Introduction and Motivation

Studying the behavior of complex systems based on the well understood properties of their constituents is a hallmark of modern reductionist science, and has been a fruitful technique in chemistry, biology, and physics. The approach is ubiquitous in atomic physics as well, in which study of many-body systems benefit from precise knowledge, diagnostics, and control of interparticle interactions and dynamics. Many exciting new research directions build on these fundamental advances to enable higher resolution, more precise control, or a bottom-up approach to systems of ever increasing complexity. Photoassociation (PA) is a technique for converting scattering atoms into bound molecules that has both benefited from, and contributed to, these topics at the intersection of physical chemistry and physics. This thesis will

- Introduce photoassociation, and motivate its use in strontium (Sr)
- Describe the experimental sequence for sample preparation and interrogation
- Highlight hardware changes to key subsystems
- Present results from performing PA in ^{84}Sr, ^{86}Sr and ^{87}Sr
- Characterize resonance amplitudes, and compare to numerical predictions

- Calculate parameters for a particular application: ^{87}Sr PA in an optical lattice
- Conclude and outline possible next steps

1.1 What is Photoassociation?

Photoassociation is a process where two colliding atoms are resonantly promoted, via a photon of the appropriate energy, from scattering states to a bound molecular state confined to an excited interatomic potential (see figure 1.1) [54]. The most basic PA variant uses a single photon to connect the ground and excited states ("free-to-bound"), resulting in the creation of dimer molecules [18].

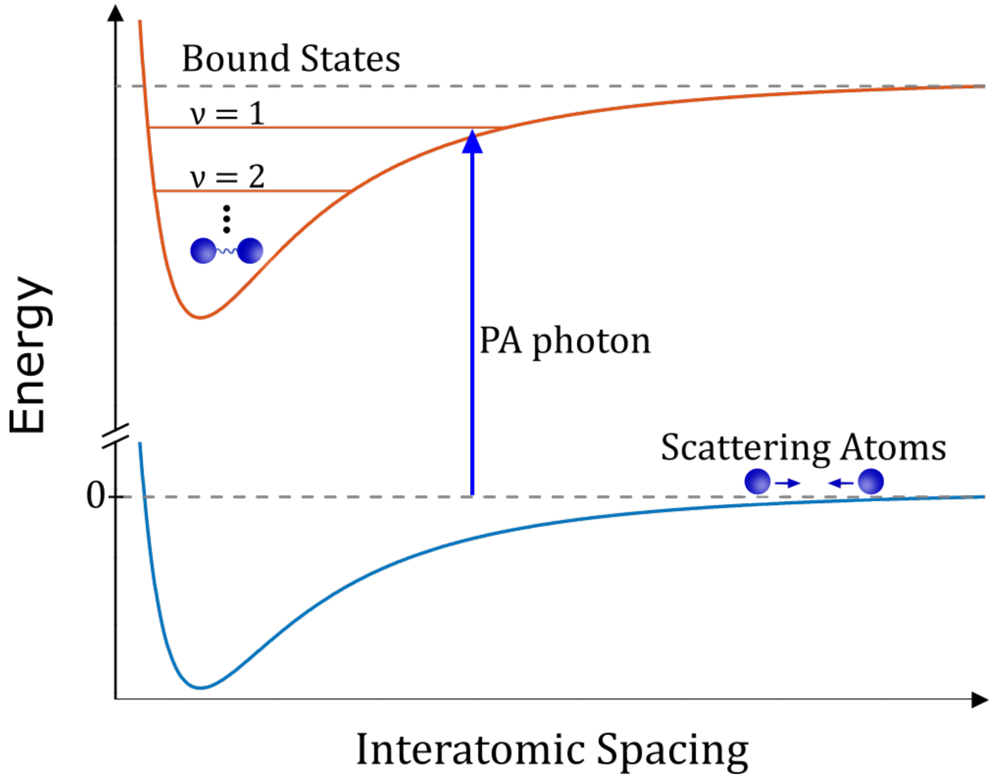

Figure 1.1: Simplified diagram of the photoassociation process showing the photon-mediated excitation of two scattering atoms to a bound molecular state.

On resonance, the photon's energy is equal to the difference between that of the ground and excited states ($E_e - E_g$), minus the initial relative kinetic energy of the colliding pair E_{kin}. In other words, for a photon of frequency ω, $\hbar\omega + E_{kin} = E_e - E_g$. Typically, the excited-state is one "rung" in a progression, or ladder, of discrete vibrational states supported by the excited potential. By varying the photon energy via a tunable light source (e.g. laser), it is possible to spectroscopically measure the binding energies and transition rates. As will be described, this information can be used to measure fundamental quantities such as the interaction strength between colliding atoms, and to produce ultracold ($T \lesssim 1\,\mathrm{mK}$) molecules as part of other experimental protocols.

Photoassociation has a long history, and is well described in the literature [94] [116] [27] [120]. Its foundation is the vast amount of information available concerning spectroscopy of diatomic molecules [48] [47] [64]. The development of PA paralleled that of techniques using lasers to trap and cool atoms, thereby reducing the thermal spread in the energy of the colliding atoms [93] [77]. This ultracold regime also reduces broadening in the spectra due to the spread in the energy in the center-of-mass motion of the colliding pair, and increases the PA technique's resolution by orders of magnitude over studies of thermal beam samples. The wide variety of atomic physics tools and procedures currently available (e.g. isotope-selective trapping, spin manipulation, and tunable geometry traps) give the experimenter unprecedented control over both the "reactants" being photoassociated, and the environment in which the "reaction" occurs.

1.2 Photoassociation Applications

Producing cold molecules: Although great progress has been made in the last decade, directly laser cooling molecules still presents a formidable challenge due to the large number of degrees of freedom involved [7] [73] [11]. Various photoassociation schemes provide an alternate route for the precise creation of ultracold molecules [120] [72]. One example of such a technique is using PA to produce extremely weakly bound molecules with internuclear separations well beyond the classical turning points. We used two-photon PA to create such "halo" molecules confined to the least-bound ($E_{binding} \sim$ 80kHz binding energy) ^{86}Sr$_2$ ground-state potential to study universal dependence on the s-wave scattering length [5] [60]. Two photon PA has also been used to create cold polar molecules, including those in the rovibrational ground-state [88] [122]. Such molecules can posses large permanent electric dipole moments that provide strong anisotropic interactions. This anisotropy is advantageous when, for example, searching for new fundamental physics or studying quantum many body phenomena [88] [8] [12] [61].

Measuring and modifying the interactions between atoms: Photoassociation typically probes the long range portion of the molecular potential where neutral atoms interact weakly via Van der Waals forces. At this length scale, and ultracold temperatures, the atomic collisions can be described by a single parameter, the s-wave scattering length [40]. Measurements of the PA spectrum allow precise mapping of the collisional ground-state wave function shape, and extraction of an associated scattering length. This technique for measuring scattering lengths is ubiquitous, and has been used with numerous atomic and molecular species [118] [131] [63].

Optically connecting the state of colliding atoms to a bound molecular state can also induce changes in the wave function for the scattering atoms, and thus the s-wave scattering length. There is interest in using lasers to modify the interaction strength of atoms like Sr with magnetically insensitive closed-shell ground-states [129] [128] [23] [24] [13] [59]. The aim is to optically mimic the powerful magnetic Feshbach resonance technique, with photoassociation acting as the mechanism for tuning the collision channels. Similar work has extended the technique to systems with more degrees of freedom such as heteronuclear species and Rydberg molecules [10] [114] [32].

Understanding fundamental properties of cold collisions: Detailed knowledge about excited molecular potentials in various atomic species helped develop and refine the techniques for laser trapping and cooling them [54]. Furthermore, measurements of the dispersion coefficients characterizing the interactions lays a valuable foundation of knowledge for experiments confining atoms in an optical lattice, optical tweezers, or in the vicinity of nanophotonic structures [102] [67] [115] [95].

1.3 Why Strontium?

Access to narrow intercombination transitions, a magnetically insensitive groundstate, and long-lived metastable triplet states in alkaline-earth elements has driven interest in their laser cooling and characterization at ultracold temperatures [62] [96] [6] [125] [39] [29] [52]. PA spectroscopy in the alkaline earth elements has most often been employed to characterize interactions in neutral trapped samples of Ca [30] [121] [117] and Sr [58] [132] [85], along with elements sharing a similar electronic structure such as Yb [44] [113] [59].

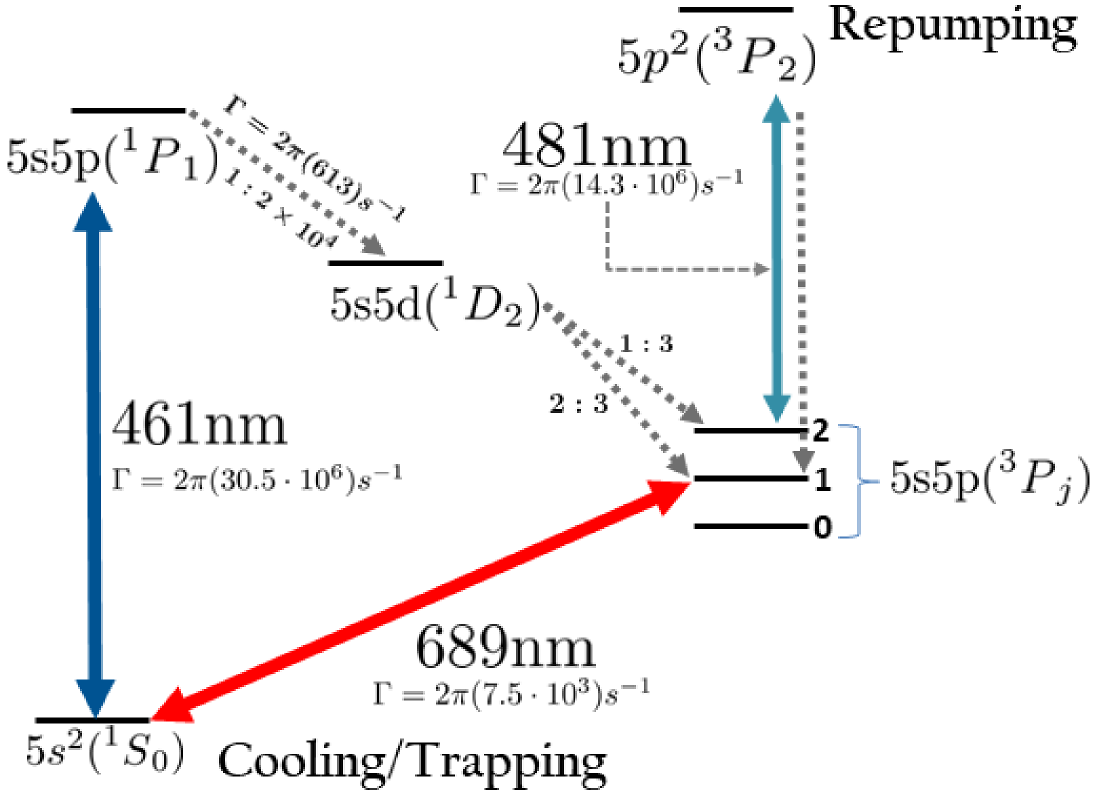

Figure 1.2: Relevant low-lying energy levels of bosonic (zero nuclear spin) Sr with select approximate transition wavelengths in nm and spontaneous decay rates Γ. Fermionic ^{87}Sr has a nonzero nuclear spin that gives rise to a hyperfine structure, as shown in figure 2.2.

In addition to the electronic properties described previously (and schematically shown in figure 1.2), Sr offers a range of available scattering lengths spanning three orders of magnitude across four stable isotopes. Moreover, methods for cooling all four isotopes to quantum degeneracy are readily available [58]. The large nuclear spin (nuclear magnetic quantum number $I = 9/2$) of the fermionic isotope ^{87}Sr leads to a tenfold degenerate ground-state who's magnetic field dependence is determined by the, comparatively small, nuclear magnetic moment. This presents an SU(N) symmetric system to explore under well controlled conditions, with N being the number of magnetic M_F states populated in the system. In ^{87}Sr, optical pumping techniques can tune N from one to ten [56]. This makes the isotope a promising platform for a wide variety of experiments at the forefront of research into quantum many-body physics, quantum information science, and precision metrology [71] [102] [22] [28] [89] [90] [83] [104] [91] [45].

For many of the Sr applications mentioned, samples are trapped in optical lattices to prevent atom-atom interactions or introduce spatial periodicity for quantum simulation of materials. PA spectroscopy is a well-established and useful technique for probing ultracold gases in optical lattices and can be used to detect double occupancy of lattice sites. The quantity and production rate of these "doublons" provides a measurement of sample temperature and probe of quantum phase transitions [99] [91] [126] [112] [111]. The possibility of applying the technique to SU(N) symmetric ^{87}Sr samples confined to a lattice was a particular motivation for our characterization of PA resonances in this isotope.

1.4 State of the Field for Sr Photoassociation

Prior to the work outlined in this thesis, single-photon PA had been demonstrated in Sr on potentials that connect asymptotically to the $5s5p\,^1\mathrm{P}_1$ state for large internuclear separations in ^{88}Sr [85] [130] and ^{86}Sr [81]. The technique had also been performed on potentials that connect asymptotically to the $5s5p\,^3\mathrm{P}_1$ state in ^{88}Sr [132] [129], ^{86}Sr [15], and ^{84}Sr [98] [108]. No PA resonances had been reported in ^{87}Sr, and no PA resonances on the molecular potential employed in this work had been reported for ^{84}Sr. These are the two isotopes most often used in Sr ultracold gas experiments. PA spectroscopy in isotopes with a similar electronic configuration to ^{87}Sr, such as fermionic ^{173}Yb [44] and ^{171}Yb [38] had been performed. These similar works served as a helpful guide when beginning our study of ^{87}Sr.

This thesis describes our results characterizing PA resonances in ^{87}Sr on the $^1\Sigma_u^+$ $5s^2\,{}^1\mathrm{S}_0$ - $5s5p\,{}^1\mathrm{P}_1$ molecular potential, as well as resonances on the same potential in bosonic ^{84}Sr and ^{86}Sr [49]. The results include extraction of a value for $^1\mathrm{P}_1$ excited-state lifetime via fits to the semiclassical LeRoy-Bernstein model, as well as measurements of the two-body collision rate and comparison to numerical calculations of Frank-Condon factors using a reflection approximation.

Chapter 2

Trapping and Photoassociation Procedure

This chapter will introduce the general techniques and experimental sequence we use to transform a chunk of purified Strontium metal into a laser-trapped, isotopically-pure, $\sim 1\mu$K gaseous sample. Then, the specifics used to perform photoassociation spectroscopy in these samples will be described.

2.1 Introduction to Strontium Trapping

Laser trapping and cooling strontium atoms is a well-established process and all four stable isotopes have been cooled to quantum degeneracy [58]. Up to the point of evaporative cooling in an optical dipole trap, our lab's sequence for producing trapped T$\sim 1\mu$K is largely similar for all isotopes. An exception to that similarity is that the additional complexity introduced by the hyperine structure of fermionic ^{87}Sr, as will be described. Atomic transitions may be identified using the shorthand of labeling them by their wavelength; see figure 1.2 for more details. The hardware and procedure developed for Sr trapping and cooling are well-documented in various theses from the Killian research group [4] [20] [79] [34]. This section will serve as a brief overview.

2.1.1 Atomic Beam

The atoms begin as solid strontium inside an oven with a directed output aperture. Resistance heaters bring the metal to approximately 400 °C at which the Sr vapor pressure is sufficiently high to create a thermal flux of atoms. The velocity of this beam is reduced by Zeeman slowing with counter propagating Doppler cooling light ($\lambda \sim 461\,\text{nm}$) and a spatially varying magnetic field. Both the cooling light and magnetic field are parallel to the thermal beam's propagation axis. This beam is then collimated by Doppler cooling, again using the dipole-allowed primary cooling 461 nm transition, along the axis transverse to its largest velocity component (perpendicular to the Zeeman slower).

Figure 2.1: Purified strontium metal (natural isotopic abundance) in a protective intert gas enclosure prior to reloading the Sr source in one of the lab's experimental stations.

2.1.2 ^{1}S$_0$ - ^{1}P$_1$ MOT, Magnetic Trap, and Repumping

After Zeeman slowing and transverse collimation, the atoms enter a main trapping volume under ultrahigh vacuum (UHV) with a base pressure less than 1×10^{-9} Torr. The center of this volume is the zero point of a quadrupole magnetic field. This field acts as the magnetic gradient for a magneto-optical trap (MOT) operating on the 5s^2 ^{1}S$_0$ - 5s5p ^{1}P$_1$ transition that both cools and confines the atoms in the center of the vacuum apparatus [40]. This 461 nm MOT is the first of two MOT stages, and takes advantage of the transition's comparatively large 30.5 MHz linewidth (732 μK and 0.512 μK Doppler and recoil temperatures respectively) for effective capturing and cooling of atoms with a broad set of velocities from the thermal beam. The frequency of the laser used in this MOT is locked onto resonance with a particular isotope via an error signal derived from saturated absorption spectroscopy in a Sr-filled heat pipe.

For laser cooling to be effective, a closed loop of energy excitation and subsequent decays needs to be available so that atoms can repeatedly absorb momentum in a manner preferential for reducing their velocity. Trapping, in a MOT for example, requires that an appreciable number of atoms are not lost to states that accumulate atoms without participation (on relevant timescales) in the cycle of photon absorption and emission. The $5s5p\,^1$P$_1$ state excited to by the 461 nm light primarily decays back to the $5s^2\,^1$S$_0$ ground-state, as desired. However about 1 in 60,000 atoms instead indirectly decays to the metastable $5s5p\,^3$P$_2$ state (see figure 1.2), with a lifetime much longer than that of a typical three to thirty second experimental cycle [26].

The negligible magnetic moment of the Sr ground-state, determined by only the nuclear moment's contribution, makes trapping it in a magnetic trap impractical. However, the $5s5p\,^3$P$_2$ state metastable state does have a experimentally useful magnetic moment ($m_j = 2$ moment $\sim 200\,\mu$K/G), and the the associated low-field seeking states can be trapped in the magnetic field of the 461 nm MOT [86]. Atoms accumulate in those states, and a 481 nm pulse from a repumping laser then excites them to the doubly-excited $5p^2\,^3\mathrm{P}_2$ state from which they then decay indirectly back to the ground-state on an experimentally relevant timescale. Other Sr repumping schemes have been explored in the past, however, the current 481 nm scheme is effective and simple to implement (requires a single diode laser source) [80]. The magnetic trap is also a valuable aid in simultaneous trapping of multiple isotopes, however, the work in this thesis is restricted to one at a time and multi-species schemes will not be discussed further.

2.1.3 $^1\mathrm{S}_0$ - $^3\mathrm{P}_1$ MOT

At the end of the 461 nm MOT stage the atomic sample has a temperature on the order of one mK. However, lower temperatures are required for effective loading into the final confining stage, an optical dipole trap. To accomplish this, we implement a second MOT stage operating on the dipole-forbidden $5\mathrm{s}^2\ ^1\mathrm{S}_0$ - $5s5p\,^3\mathrm{P}_1$ transition ($\lambda \sim 689\,\mathrm{nm}$), which has a comparatively narrow 7.5 kHz linewidth ($0.180\,\mu$K and $0.229\,\mu$K Doppler and recoil temperatures respectively). However, even at 461 nm MOT temperatures, the thermal distribution of atomic velocities makes efficient capture by the narrow 689 nm system nontrivial [107]. A number of steps, such as frequency dithering, are taken to better match the second stage MOT's light to the sample's condition at the end of the first stage MOT [33]. Lastly, the frequency dither is reduced and this 689 nm MOT is ramped into a single frequency regime with lower optical powers to achieve typical temperatures of $1 - 2\mu\,$K.

The hyperfine structure of fermionic ^{87}Sr (see figure 2.2), with nuclear spin quantum number I= 9/2, presents additional complexity regarding the operation of the 689 nm MOT. The $^1\mathrm{S}_0$ ground-state has a significantly different magnetic field dependence than that of the $^3\mathrm{P}_1$ excited-state [56]. This difference leads to unfavorable energy level shifts that can allow anti-trapping transitions to occur where the photon absorption recoil kicks the atom *away* from center of trap, making it unstable. Simultaneous application of a “trap” beam exciting to the upper F= 11/2 state, and a “stir” beam exciting to the F= 9/2 state can mitigate this issue [84]. The $F = 9/2$ state’s approximately 1/4.5 smaller magnetic field dependence (vs that of the $F = 11/2$) allows the atom being illuminated to scatter more photons before leaving the spatial region of resonance dictated by its velocity and the MOT’s magnetic field geometry. This additional photon scattering randomizes the occupied m_F levels such that, on average, the excitation of trapping transitions are favored and a stable trap can be achieved. The relative transition probabilities can be determined by the Clebsch-Gordon coefficients that parameterize the respective transition matrix elements [79]. The stir beam’s level-randomizing effect is also why, to a good approximation, ^{87}Sr atoms from the 689 nm MOT are equally distributed among the ten available m_F states.

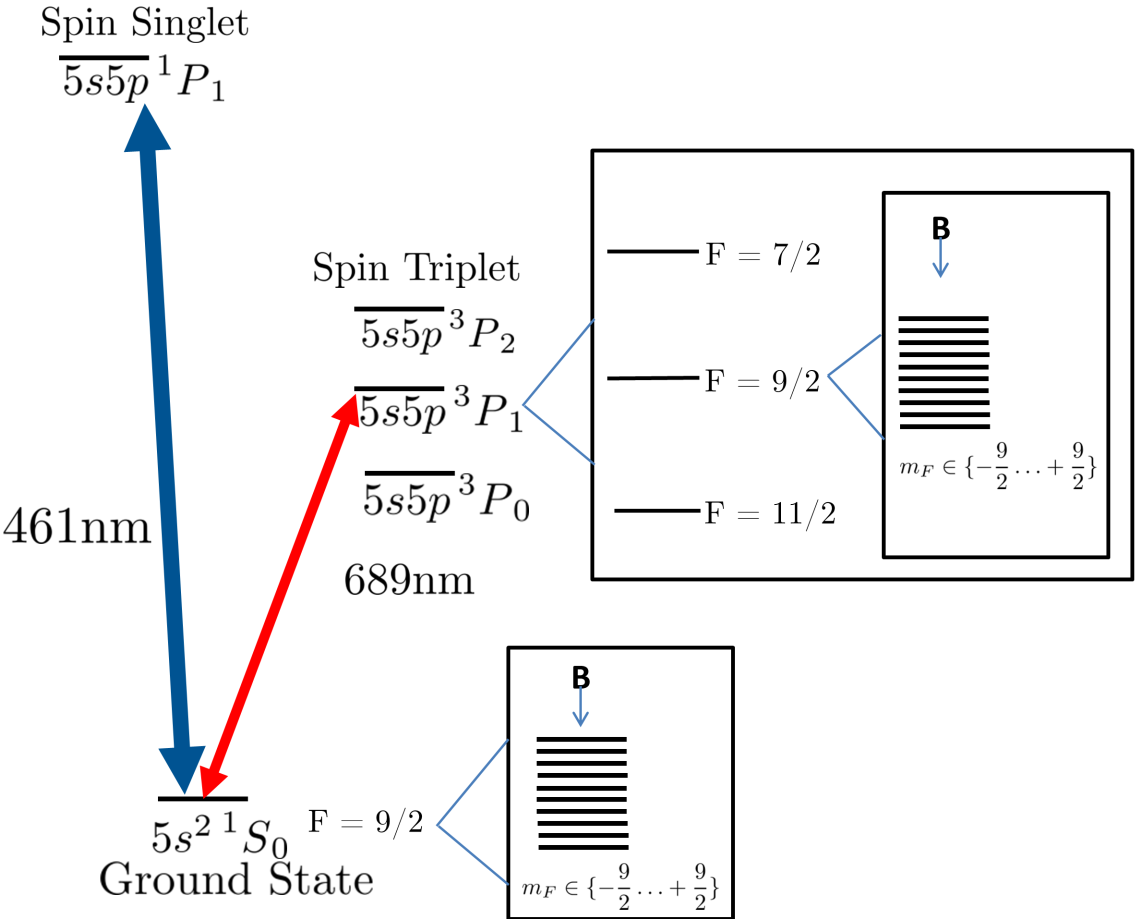

Figure 2.2: Diagram of relevant hyperfine structure for fermionic ^{87}Sr MOT operation. See table 4.1 for quantitative shifts of F levels. The presence of a magnetic field **B** lifts the degeneracy of each manifold with total angular momentum quantum number F. The figure insets give example qualitative representations.

The laser used in creating the 689 nm MOT derives its relative stability from being locked to an ultra low expansion (ULE) optical cavity that is in turn referenced the $^1S_0$ - $^3P_2$ atomic transition via saturated absorption spectroscopy in a Sr-filled heat pipe. The frequency of the repumping laser is also controlled, indirectly, by this system. The repumper and 689 nm beams are overlapped in a dual wavelength optical cavity, and electronics feed back to the 481 nm laser based on the measured difference in cavity resonance peaks between the two wavelengths.

2.1.4 Optical Dipole Trap

Now at temperatures of approximately $1 - 2\mu$K, the atoms in the 698 nm MOT are cold enough for efficient loading into an optical dipole trap. Neutral atoms can be trapped using the intensity gradient of a high-intensity laser with a frequency far from resonance with respect to any strong atomic transition(s). Trapping is enabled by the dispersive interaction between the trapping laser field and an induced electric dipole moment of the atom [41]. An atom's response to an applied light field is often described in terms of a complex polarizability α, where $\mathrm{Re}(\alpha)$ determines the trapping potential, and $\mathrm{Im}(\alpha)$ determines the heating (scattering) [82]. In theory, the polarizability contains contributions from every possible combination of states coupled by the laser. In the case of a single dominant transition, such as the $^1\mathrm{S}_0$ - $^1\mathrm{P}_1$ 461 nm in Sr, this provides the greatest contribution to the polarizability. Therefore, in the description below, all atomic properties and detunings are taken with respect to this transition.

It is possible to engineer an intensity and frequency regime such that the atoms experience a useful confining potential without too much heating as a consequence of scattering. When the beam's frequency ω is detuned ($\Delta = \omega - \omega_0$) sufficiently lower than ("red" of) the dominant transition (ω_0), the confining potential is such that it is energetically preferential for ground-state atoms to move towards the region of highest intensity. For laser beams with a radial Gaussian intensity distribution $I(r)$ (transverse to the beam's propagation axis), this means the atoms experience a force radially inward towards the center of the beam. The potential energy of such a configuration is

$$U = -\frac{Re(\alpha)}{2\epsilon_0 c}\, I(r) \;=\; \left(\frac{3\pi c^2}{2\omega_0^3}\right)\frac{\gamma_{atomic}}{\Delta}\, I(r) \tag{2.1}$$

where γ_{atomic} is the rate of spontaneous decay, ϵ_0 is the vacuum permittivity, and c is the speed of light.

For a Sr atom in the ${}^1\mathrm{S}_0$ ground-state, and a laser frequency of 1064nm, $\alpha = 232.87$ in atomic units [4] [79]. The atomic unit of polarizability is $e^2 a_0^2/E_H$ =1.648×10^{-41} $\mathrm{c}^2\mathrm{m}^2/\mathrm{J}$ where e is the electron's charge, a_0 is the Bohr radius, and E_H is the Hartree atomic energy unit [3]. This sets the scale for an approximate depth of the trapping potential, not accounting for the effects of gravity (see J. Aman's PhD thesis for more detail).

The ODT is a versatile trap that can be configured into different geometries depending on the required application. Allowing the most energetic atoms to escape via an evaporation process by either holding in a static trap or dynamically reducing the trapping potential (forced evaporation) has been a crucial technique in cooling all species of Sr to quantum degeneracy [58]. The required geometry and evaporation process are typically determined by the interaction strength of any isotope(s) under consideration, and the desired final temperature. In this thesis, the trap is formed from the intersection of two elliptical $\lambda = 1064\,\mathrm{nm}$ beams, each with a peak power of about one Watt. See table 4.2 for more information on the specific trap configurations during PA spectroscopy in each isotope.

2.2 PA Experimental Methods

The PA excitation laser is a Toptica SHG Pro system consisting of a laser unit and associated electronics modules. The laser unit is comprised of a $\lambda \sim 922\,\mathrm{nm}$ infrared diode laser (master oscillator) in Littrow configuration which is amplified via a tapered amplifier before being directed into a bowtie cavity. A nonlinear crystal in the cavity converts the light from infrared to visible wavelengths via second harmonic generation (SHG). The cavity is locked to resonance with the highest power mode using the Pound-Drever-Hall technique. Once up and running, the laser's power output is typically stable at between 25-60 mW, though it can be challenging to re-optimize the system to this level after a period of long downtime. The mode-hop-free tuning range is typically about 3.5 GHz (see the appendix for more details). The laser electronics accept an external control voltage which is then amplified and used to adjust the master oscillator's wavelength by mechanical (piezo) tuning of the diffraction grating. This method is how we include programmatic fine changes to the laser's wavelength into our experimental scan software. Moderate wavelength tuning (hundreds of MHz to tens of GHz) is accomplished by changing the master oscillator temperature, while gross tuning (hundreds of GHz) requires manual mechanical (screw) adjustments to the master oscillator's diffraction grating housing.

Light from the PA laser is first directed (see figure 2.3) through an anamorphic prism pair, which helps to circularize the otherwise elliptical beam. From there it passes through a number of shaping lenses for more efficient coupling into two optical fibers. One fiber carries a small amount of light to a wavemeter for monitoring the laser's wavelength (see figure 4.4). The second fiber carries the majority of the light to the main experimental table, where it is applied to the atomic samples. The light sent to the wavemeter is picked off prior to the AOM.

The +1 order of an 80 MHz AOM is used to apply light to the atoms in 10-1000 ms pulses of controlled duration. In conjunction with a photodiode on the output of the fiber, this AOM also serves as a means of stabilizing the optical power through this fiber via a PID feedback loop. A mechanical shutter was used to block any stray 461 nm photons that otherwise may have found their way into the fiber and onto the atoms. Given the photons' comparatively large energy, this is a precaution against unwanted atomic sample heating or distortion. See the appendix for a simple and robust circuit used to drive the shutter.

For these wavelengths, we use Thorlabs P3-488PM-FC fibers between five and thirty meters in length. Given the amount of optical power available from the laser, we only require modest coupling efficiencies for these experiments (50%), but have found that mechanical bending or twisting of the fiber itself can decrease power throughput by as much as 25% relative to the static, optimized, baseline. We also observed an exposure time dependence on the coupling efficiency of light through the higher power fiber for exposure times longer than approximately a few hundred ms. This dependence was most pronounced when operating at higher PA beam powers, and our hypothesis is that a combination of thermal load on the input collimator and stimulated Brillouin scattering within the fiber was the cause. Though these fluctuations reduced the maximum power available incident on the sample, the power control feedback loop was capable of maintaining constant power through the fiber in all applications.

Once transported via fiber to the main experimental table, the PA excitation beam is further shaped via a sequence of lenses before entering the vacuum chamber containing the trapped atomic sample. A polarizing beam splitter (PBS) cube and careful choices of any subsequent reflection angles ensure only horizontally linearly polarized light is incident onto the atoms. Two dichroic mirrors are included in the scheme (DMLP505 and DMSP805). These act as mirrors for the 461 nm light, and transmit 689 nm (existing push-beam) and 1064 nm (existing ODT beam) respectively. The PA laser beam has e^{-2} radii of $w_{\mathrm{horz}} = 850\,\mu\mathrm{m}$ and $w_{\mathrm{vert}} = 440\,\mu\mathrm{m}$ on the atoms, which are 59.75 ± 0.25 cm from the front face of the fiber collimator. The elliptical shape was chosen to better match that of the ODT beams (and thus trapped sample). Depending on the isotope being studied, the intensity at the atoms' location is between 3.6 and 237 $\mathrm{mW/cm^2}$, and exposure times are between 10 and 1000 ms.

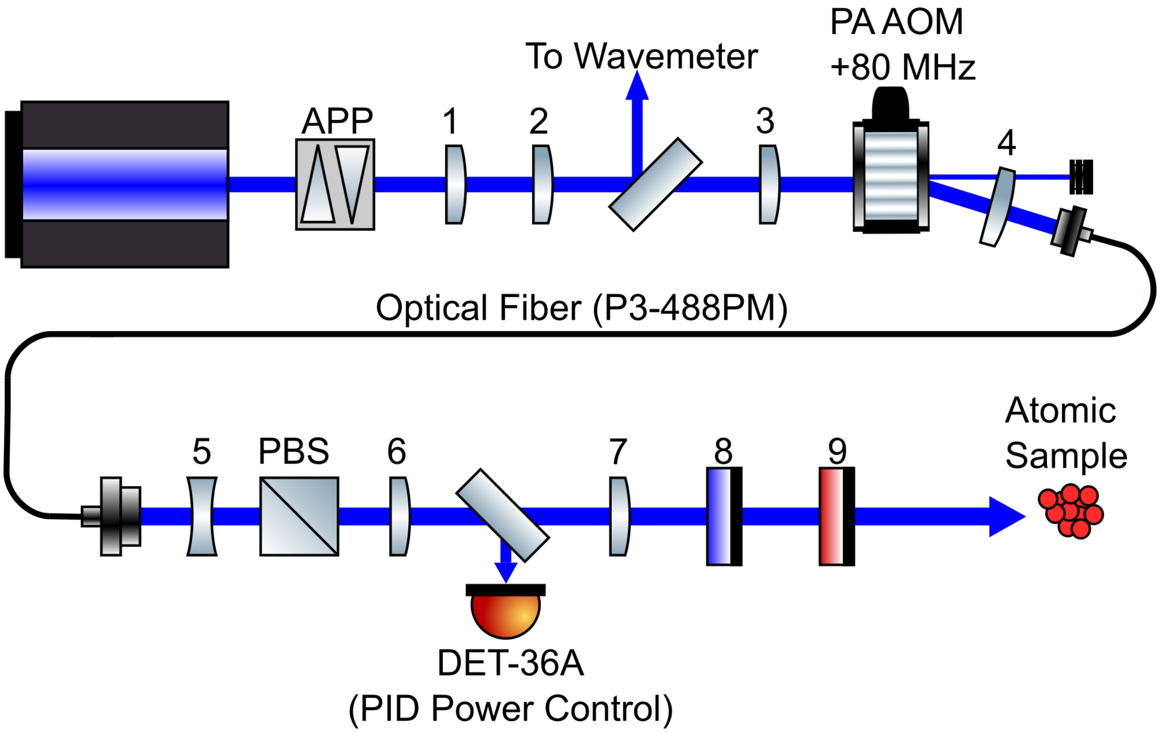

Figure 2.3: Optical path of the PA excitation laser. In ascending order, the numbered components are +250 mm lens, +400 mm vert. cyl lens, +500 mm lens, +500 mm lens, -200 mm lens, +400 mm lens, +1 m lens, DMLP505 dichroic mirror, and DMSP805 dichroic mirror. Lenses are identified by their focal length, and are spherical unless otherwise noted. The APP helps circularize the beam directly from the laser, the shaping optics prior to the fiber allow improved mode-matching into it, the pickoff beam to the wavemeter allows monioring the laser's wavelength. The DET-36A photodiode is part of a PID feedback loop that stabilizes the optical power through the fiber by feeding back to 80 MHz AOM's RF drive amplitude and therefore controlling the amount of light diffracted. The dichroic mirrors allow for a more compact inclusion of the PA optics into a crowded table section with pre-existing beam paths. These two components, eight and nine, reflect 461 nm light and transmit 689 nm and 1064 nm light respectively.

2.2.1 Atom Imaging

Immediately after applying the photoassociation pulse, the atoms are released from the confining dipole trap for time-of-flight imaging. They fall under the influence of gravity for a determined time, and are destructively imaged by shining light resonant with the $^1\mathrm{S}_0$ - $^1\mathrm{P}_1$ transition through the sample onto a detector (camera) [33]. A dual imaging pulse scheme (with and without atoms present) is used to create a reference for artifact removal via a background subtraction in software. Knowing the time between releasing the atoms and their imaging, the recorded pictures can be fit to quantify the trapped sample's number of atoms and temperature [20].

The hyperfine structure of fermionic ^{87}Sr introduces a state dependence to the absorption cross section. Even when set to resonance with a particular excited-state, imaging light for this isotope causes optical pumping among the associated m_F levels. Therefore, the cross section is dependent on the initial distribution of states, and subsequent dynamics. Calculations have shown that, across the full range of initial and final population distributions, the effective ^{87}Sr 461 nm absorption cross section for linearly polarized light can be approximated as half that of the bosonic isotopes [79]. Therefore, we incorporate a factor of two when imaging ^{87}Sr samples.

Chapter 3

Neutral Apparatus Additions

The Killian laboratory group is comprised of multiple experimental subgroups, each with its own set of atom trapping and cooling equipment. In particular, I have worked on two such distinct and independent subgroups, the "Neutral" and "Rydberg" subsystems. As far as the photoassociation experiments described in this thesis are concerned, both subsystems trap and cool atoms via the same sequence of steps, as described in chapter two. All data presented in this thesis were taken using the Rydberg subsystem. This chapter presents experimental hardware modifications to the Neutral apparatus.

3.1 Frequency-Doubled 461 nm Laser System

The Neutral apparatus generates 461 nm light for the $^1S_0$ - $^1P_1$ trapping and cooling stages by frequency-doubling 922 nm light in optical cavities containing a potassium niobate nonlinear medium. There are two such cavities and one is dedicated solely to producing light for the Zeeman slower. The other "MOT" cavity generates light that is used for the 461 nm MOT, transverse collimation, saturated-absorption spectroscopy, and atomic absorption imaging [4].

When properly aligned and optimized, each doubling cavity is capable of producing 100 - 150 mW of 461 nm light. However, the parameter space for optimizing the 461 nm power is large. Additional complexity is introduced by the need to amplify the 922nm master laser's approximately 20 mW output, to the 250-300 mW necessary for achieving the necessary amount of frequency-doubled power. Each cavity has a dedicated tapered amplifier (TA) associated with it to achieve this.

In late 2019 the MOT cavity subsystem had degraded such that it's 461 nm power was down to approximately 60 mW (roughly half of it's optimized peak), and none of the standard techniques were successful in restoring it. The system was also suffering from bursts of noise approximately four times the normal background, at a rate of around once every few seconds. In the search for a root cause of this issue, we optimized a number of optical paths as follows.

3.1.1 922 nm Fiber Coupling

After exiting the 922 nm Littrow-configuration ECDL head, the beam passes through two optical isolators before being coupled into a pigtailed optical fiber (see figure 3.4). The coupling efficiency through this fiber was sub-optimal at around 45 mW/90 mW = 50%. We also suspected that in spite of the isolators, a back reflection into the master laser was causing frequency instability. This instability was manifesting as noise on the frequency doubling cavity locks. Therefore, we profiled various beams to understand what distances and shaping optics could better mode-match fiber's optimal input.

Figure 3.1 is a profile of the beam exiting the ECDL laser head (hereafter, "the head"). Zero distance in the plot corresponds to the output face on the white external housing of the head. In this measurement there are no shaping lenses in the path, and the beam passes through one OFR IO-3-922-HP model Faraday optical isolator between the output and the first data point. The plot is of geometric distance only and the dependent variable is the beam's e^{-2} intensity radius.

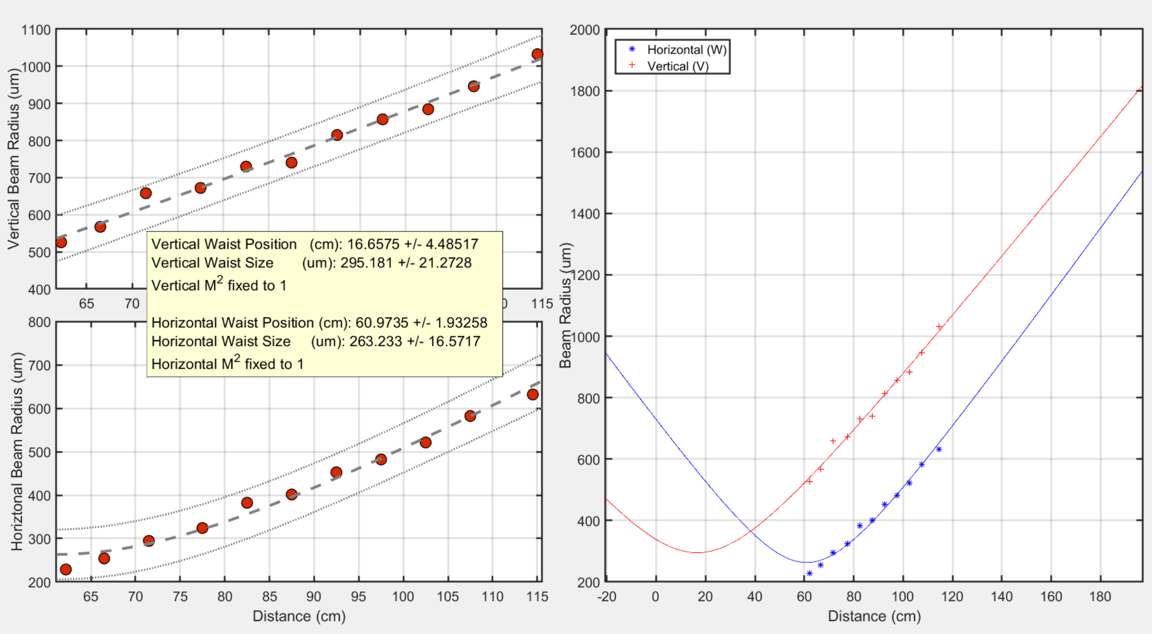

Figure 3.1: Gaussian profile of the 922nm beam exiting the head. Zero distance in the plot corresponds to the output face on the white external housing of the head. In this measurement there are no shaping lenses in the path, and the beam passes through one OFR IO-3-922-HP model Faraday optical isolator between the output and the first data point. The plot is of geometric distance only.

Now understanding the beam to be coupled into the fiber, we need to know what mode the fiber and its input collimator support to obtain the maximum light throughput. To do this, we profiled the small amount of light propagating backwards out of the input fiber collimator; light that originated from the un-seeded TA. That measurement is pictured in figure 3.3 and the zero-distance reference point pictured in figure 3.2.

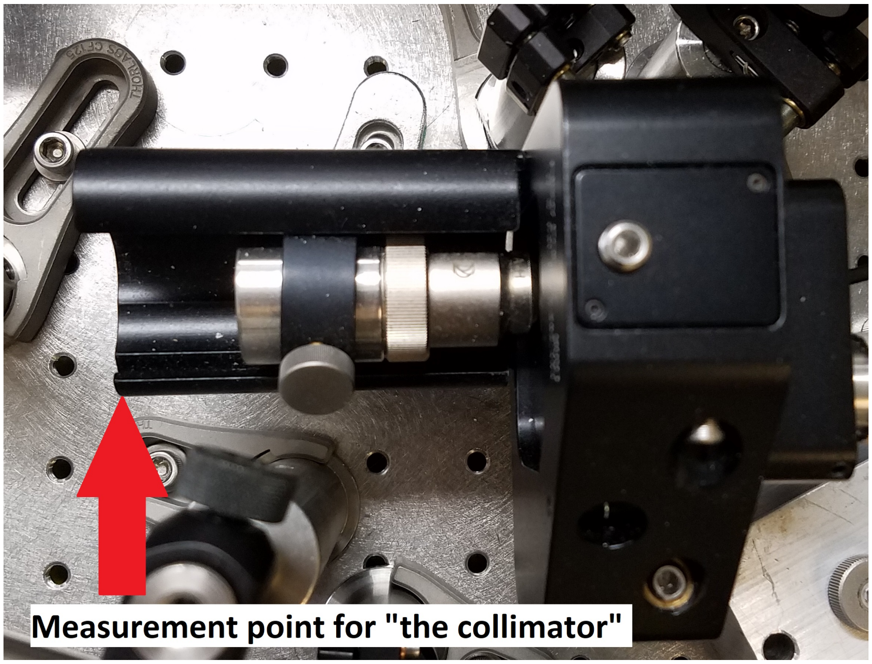

Figure 3.2: Depiction of the 922 nm input collimator and its mount. The point indicated is the measurement reference point (0 cm) in figure 3.3.

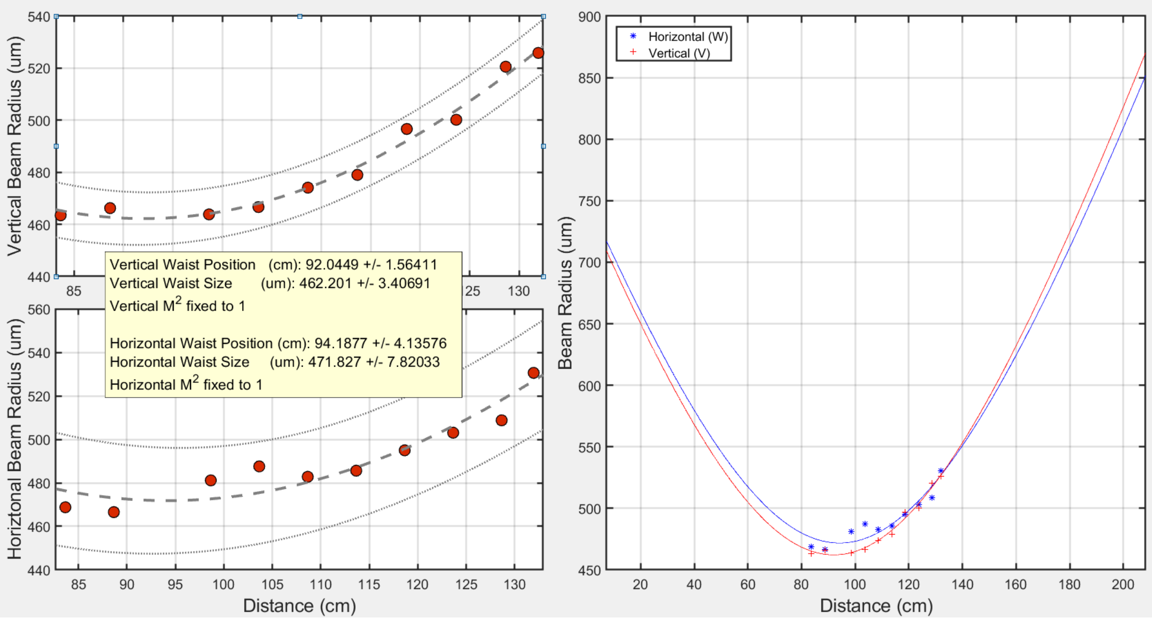

Figure 3.3: Gaussian profile of a 922 nm beam propagating backwards from the TA, through the fiber towards the ECDL head. The edge of the fiber collimator (pictured in figure 3.2) is located at 155.9 cm, and beam propagation is in the direction of decreasing distance. This is done in order to have a single coordinate system for all plots of the fiber mode matching.

An ideal mode-matching solution would overlap the waist sizes and locations of the beams profiled in figures 3.1 and 3.3. To achieve this matching we use a +500 mm *spherical* lens and judicious adjustments of the path length to mode-match the ECDL beam's vertical axis to that of the fiber, then circularize the input beam with a +500 mm *cylindrical* lens acting on the horizontal axis.

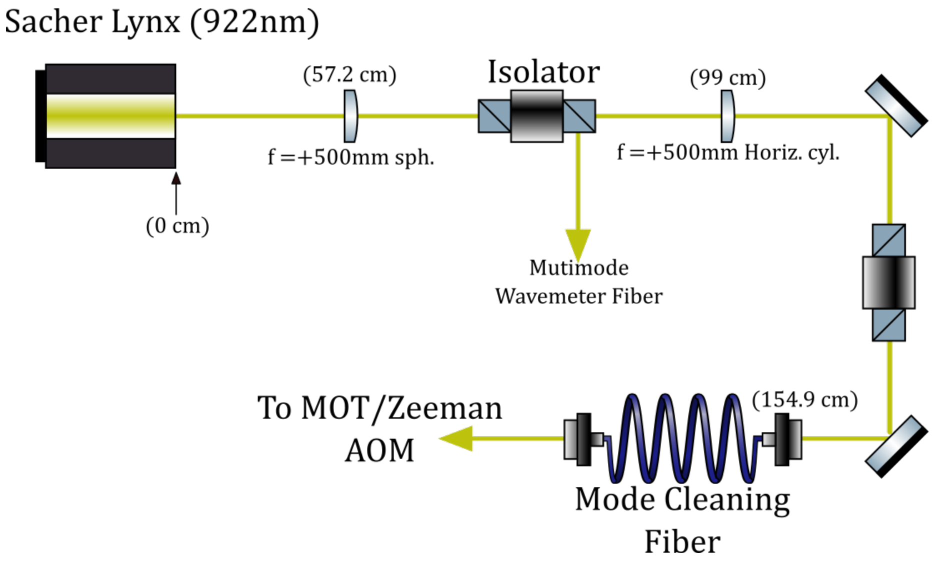

Figure 3.4: Schematic of the 922 nm master beam propagating from the head towards the input collimator of the fiber. Geometric distances from the ECDL on the optical table are indicated in parentheses. Drawn distance are not to scale. Note that there is a $\lambda/2$ waveplate with rotational freedom on the output of each of the two optical isolators.

A profile of the beam from the ECDL going through a spherical +500 mm lens at 57.2 cm was used as an input to further beam-propagation calculations for mode matching. Figure 3.5 models the propagation of that beam through a +500 mm cylindrical lens on the horizontal axis at 99 cm from the laser head. Data from figure 3.3 are included to visualize the extent of the overlap (matching). Based on this profile, optimal mode matching is obtained by placing the collimator at 155.9 cm from the ECDL. Changes in optical path length due to the index of refraction of optical elements along the path would change this by about -1 cm, therefore the collimator is placed a physical distance of 154.9 cm from the head. After making the improvements above, the coupling efficiency of the 922 nm light through the fiber was increased by approximately 10% to 60% throughput.

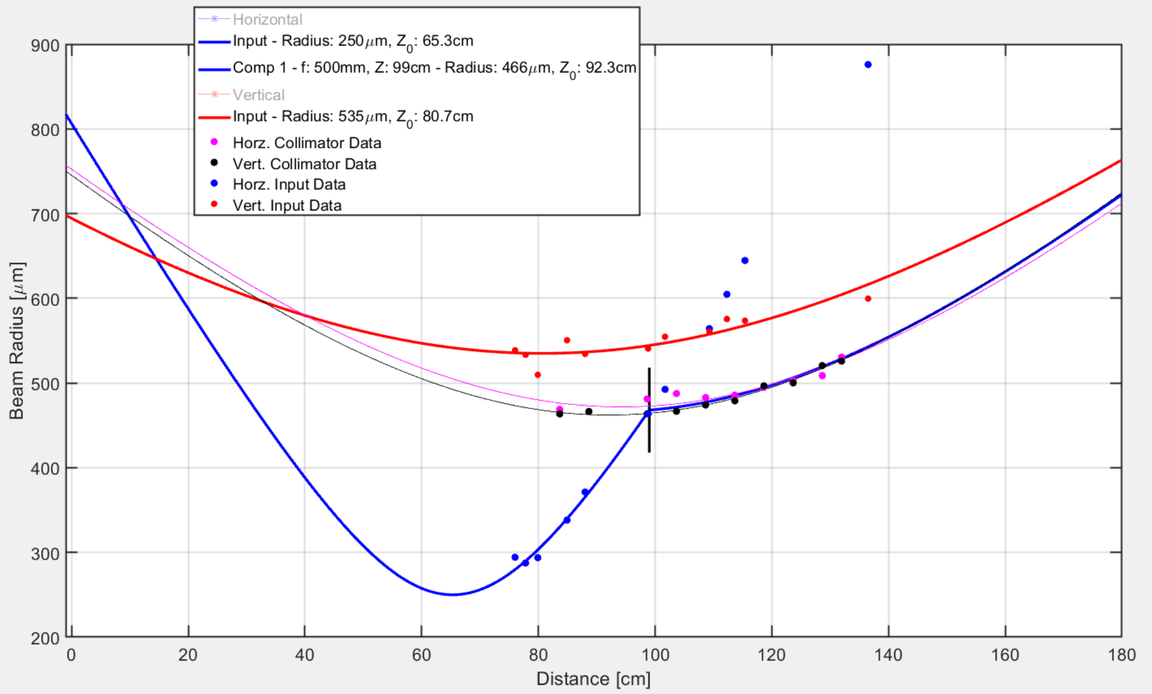

Figure 3.5: Plot of mode matching solution for the 922 nm master beam propagating from the head towards the input collimator of the fiber. Zero distance is the ECDL head. The input of the Gaussian propagation model (red and blue circles) is a measurement of the beam from the ECDL after propagating through a spherical +500mm lens at 57.2cm. The input is propagated programatically through a +500mm cylindrical lens acting on the horizontal axis at 99cm from the laser head, and plotted on top of the measurement we are mode-matching to (magenta and black circles). The face of the collimator is at 154.9cm. We chose to match the horizontal axis most closely. Uncertainties up to ±0.5 cm in measuring distances preclude finer optimization.

To monitor the polarization purity of the light exiting the fiber, we installed a polarizing beam cube after its output. The cube can be slid repeatably in and out of the beampath as needed. We optimized the transmission through this cube by rotating the $\lambda/2$ waveplate on the output of the final isolator before the fiber. The powers are documented in table 3.1.

Through fiber: no cube, no waveplate	61 mW
Rejected from cube: optimized waveplate	0.4 mW
Through fiber: no cube, with waveplate	60.5 mW
Through fiber: with cube and waveplate	58.5 mW

Table 3.1: Powers in various configurations of the monitoring cube after the 922 nm fiber.

Monitoring the rejected power through the cube, we see that any polarization fluctuations are below 10%. An example of the time-drifts in power through the fiber is shown in figure 3.6.

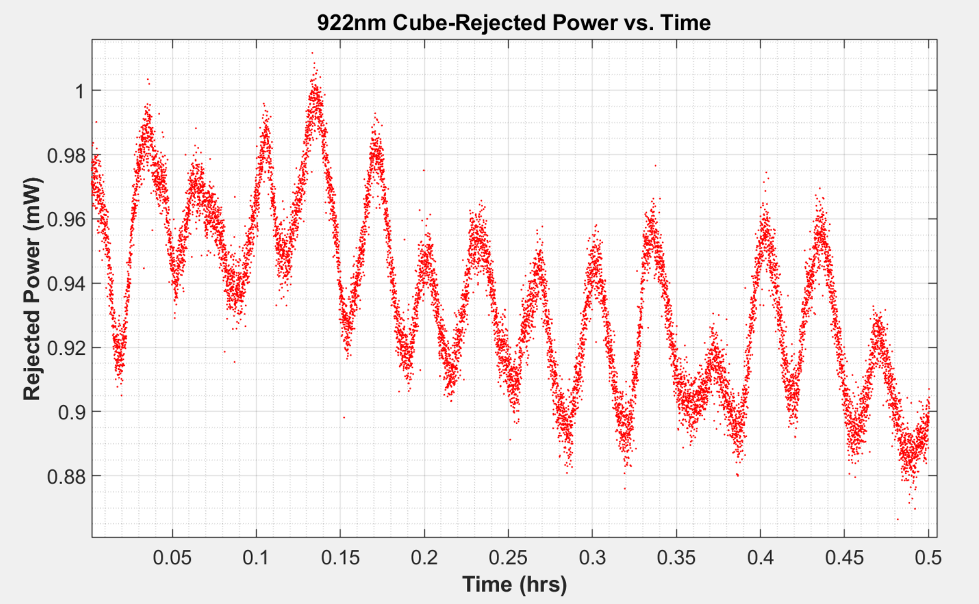

Figure 3.6: Power rejected from the 922 nm polarization-monitoring cube over time.

For reference, the transmitted power during this time was steady at 62 mW. The scale of these fluctuations is small enough to suggest that polarization issues were not a cause of the drifts in power from the MOT cavity. However, improving the polarization stability such as with a different fiber setup, might yield noticeable improvements.

We also realigned the two optical isolators on the path between the head and the fiber input collimator. Propagating away from the head, the 1^{st} isolator was adjusted to have -30 dB of isolation, and the 2^{nd} to have -27 dB. During this alignment we found that a stray reflection from the 1^{st} isolator's input face was a major factor in the noise of the 922 nm master laser. Placing the isolator at a slight angle from colinear with the beam improved the situation. Some noise still remained, and there is evidence that the issue was a sub-optimal mode of the 922 laser. The characteristic period of the noise bursts changes when the laser mode-hops, and a new grating-PZT voltage is required to get back to the appropriate wavelength.

3.1.2 MOT Doubling Cavity Improvements

After exiting the fiber mode-matched in the previous section, the 922 nm light is split by a 252.4 MHz AOM into paths leading (after passing through their respective TAs) to the two frequency doubling cavities. The TA seed light from the AOM is split unequally, with about 20% more power going into the MOT cavity TA. Passing through the AOM, the MOT cavity beam uses the zeroth order, and that beam's optimization will be discussed here. The overall goal was to increase the 461 nm power coming from the MOT doubling cavity up to or above 100 mW. A secondary goal was to improve the stability of the cavity's 461 nm power output because it suffered from slow drifts by as much as 40% on an hour timescale.

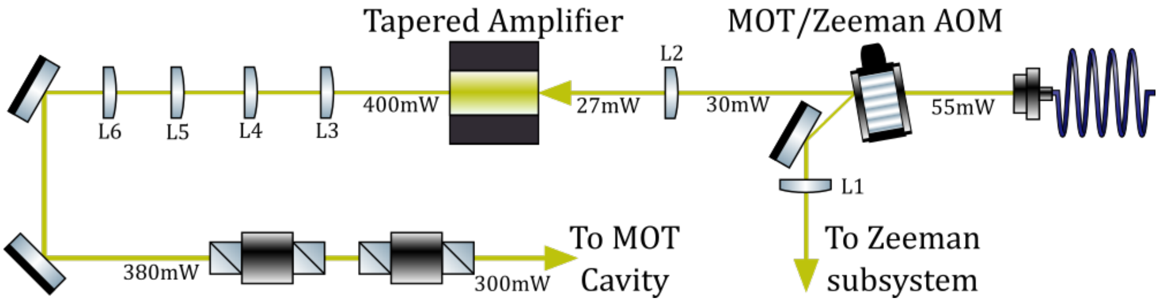

Figure 3.7: Schematic of 922 nm beam for the MOT cavity subsystem. Approximate optical powers at each point are indicated and the drawing is not to scale. Note that the physical distance between the AOM and tapered amplifier is nearly 2 m, and that there is a $\lambda/2$ waveplate on the input of the first isolator. The focal lengths and geometries of included lenses (L1 through L6) in-order are: 250 mm spherical, 500 mm spherical, 80 mm vertical cylindrical, 200 mm horizontal cylindrical, unlabeled telescope, 250 mm horizontal cylindrical.

The long (nearly 2 m) path length between the 922 nm fiber output and the MOT cavity TA was an initial cause for concern. Pointing instability of the beam into the TA could be a source of the power fluctuations we observe from the MOT, especially if it leads to pointing instability though the tightly constrained path through the dual isolators. After measuring beam powers at the TA input, post-isolators, and post-cavity, we found no evidence that this was the case.

3.1.2.1 MOT Cavity Alignment Optimization

Optimization of the 922 nm light entering the MOT cavity follows a similar procedure to that for a fiber or TA. The beam being sent into the device is carefully measured (profiled), and then adjusted to best match the device's natural mode. In the case of the MOT cavity, the natural mode is the fundamental mode of the resonator. The partially transparent cavity mirror affects the input beam in different ways, depending on the cavity geometry. For the MOT cavity, the mirror is plano-concave with a 25 mm radius of curvature and a reflectivity at 922 nm of 0.975 (curved surface) [100]. Therefore the mirror acts as a $f = -50\,\mathrm{mm}$ spherical lens upon the 922 nm beam passing through it. This lensing effect is crucial to account for when mode-matching light into the cavity [103].

Ideal matching is achieved when the waist size and location of the input, after propagating through the curved incoupling mirror, match the natural waist of the cavity. Because we typically consider only the TEM_{00} Gaussian mode when characterizing and modeling beams, specifying the intensity e^{-2} waist size and location is sufficient to completely describe the beam's free-space behavior. If needed, higher-order modes can be modeled, though uncertainties in measurements of distances and indices of refraction are often of greater significance.

Moving the the +200 mm lens (see figure 3.8) immediately prior to the cavity back (away from cavity) by two centimeters significantly improved the cavity coupling and resulted in just over 100 mW of 461 nm light being produced in a stable manner. Further adjustment to the cavity temperature and alignment could produce powers as high as 140mW. However, the resonator appeared to be unstable at the higher output powers, and would quickly drop to a lower-power mode.

The cavity alignment's sensitivity on the +200 mm lens position made it useful to have a single-point measurement of the beam's transverse position prior to adjusting its location. This measurement then provides a good starting place when realigning the system after moving the lens. We used a wedged beam sampler to direct about 5% of the input light onto a beam camera. The camera image's coordinates were recorded, and then used as a metric when realigning the system. This was a reproducible way to quickly return to optimal alignment into the cavity after each lens movement iteration. Afterwards, the cavity coupling can be further tuned via mirror alignment to reduce the relative size of non-fundamental modes to that of the TEM_{00}. This final optimization is done by observing the cavity output on a photodiode while scanning the PZT controlling the resonator's length.

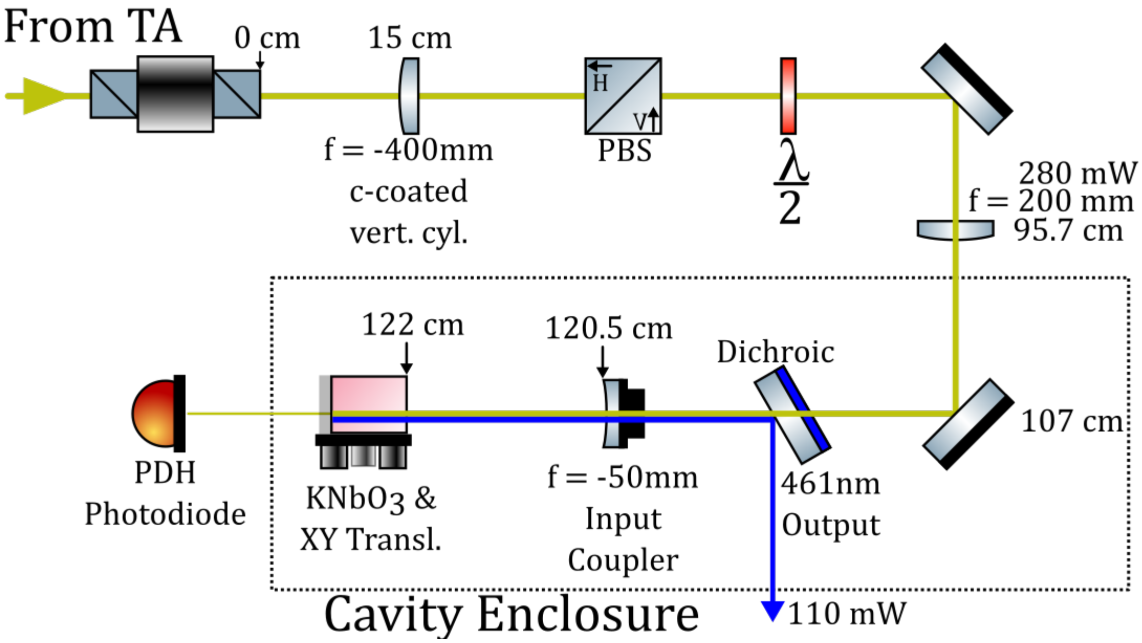

Figure 3.8: Schematic of 922 nm beam from the dual isolators to the MOT cavity doubling crystal. Not to scale, selected approximate optical powers indicated, distances are geometric and referenced to the output of the last isolator (closest to the cavity). The thicknesses of the dichroic mirror, input collimator, and crystal are 1.5 cm (n = 1.5), 0.4 cm (n = 1.5), and 0.5 cm (n = 2.8) respectively. The indicated distance to the crystal corresponds to the axial translation stage at 0.675 in.

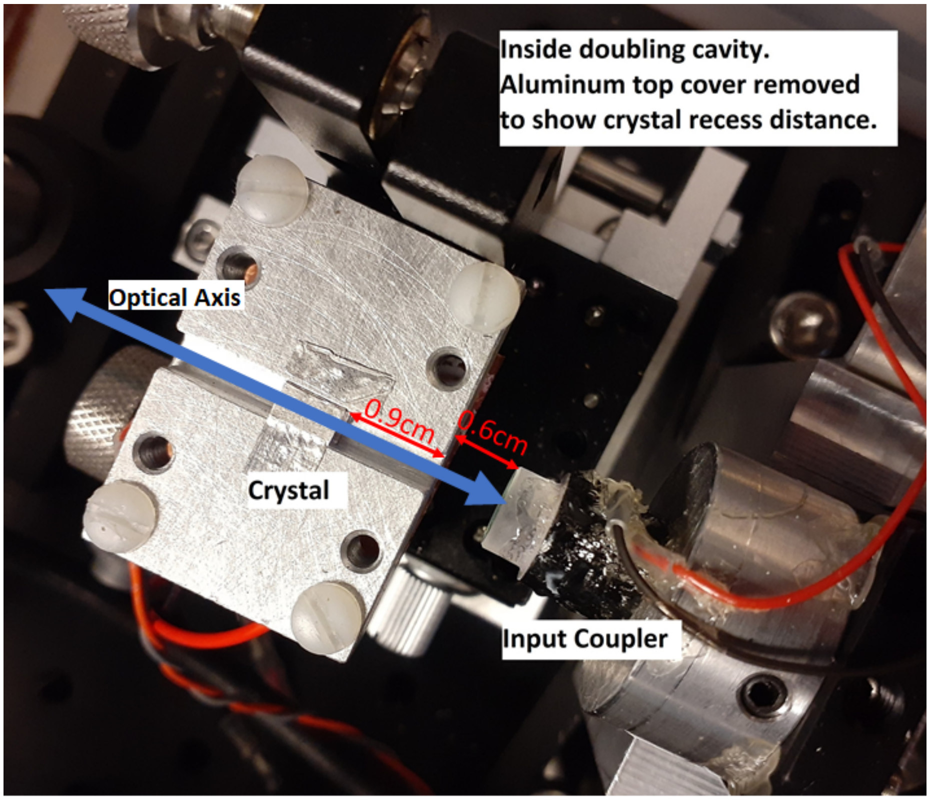

Figure 3.9: View of the doubling crystal housing inside the MOT cavity, with top-cover removed. The crystal is recessed 0.9 cm from the side of the aluminum mount on the side facing the input coupling mirror. The coupling mirror's curved, reflective, side is 0.6 cm away from the mount face closest to it. The flat silver foil on top of the crystal is made of indium, and serves to add additional mechanical and thermal contact between the crystal and the housing.

3.2 Electronics

This section describes two particular electronics projects undertaken during my degree that were first implemented on the Neutral apparatus. Their generality and usefulness led to later implementation of copies in other sections of the Killian lab.

3.2.1 Arduino General-Purpose Slow PID Lock

A ubiquitous tool in both research and industrial control applications is the proportional integral derivative (PID) feedback method. PID is a simple feedback method for calculating an appropriate correction signal to be fed back to a system under control. This correction signal is based on the deviation of a system parameter from a desired set point. The parameter which is monitored and controlled will depend on the type of system. In many cases, the system information is converted to a voltage or current for the purposes of manipulation. When applied to the system, the correction signal closes the feedback loop and stabilizes ("locks") the system at the desired point against perturbations. In the laboratory, they are a common tool for locking parameters such as laser powers, heater temperatures, and laser frequencies. The latter is the case described here.

3.2.1.1 Basic PID Operation

Figure 3.10 shows a block diagram of a general PID control loop. Information about the current state of the system is combined with the desired set point, to form an "error" signal $e(t)$ containing information on how far any deviation is from the ideal conditions. The PID algorithm then acts on this time-dependent signal to generate a correction signal $V(t)$

$$V(t) = K_p e(t) + K_i \int_0^t e(\tau) d\tau + K_d \frac{\mathrm{de(t)}}{\mathrm{d}t} \tag{3.1}$$

where the three K parameters define the response, and are the "knobs" available tuning by the user. The resulting correction signal is then fed back to the device under control to alter its state towards the desired one, reducing the error signal (ideally) to zero.

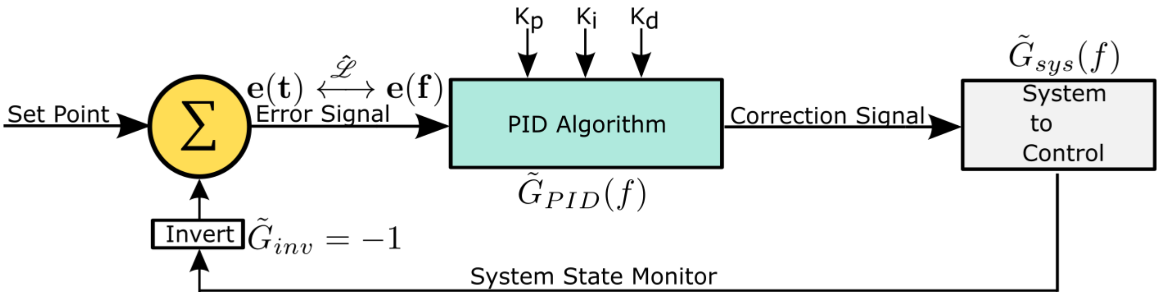

Figure 3.10: Block diagram of the fundamental operating segments of a PID-based feedback loop. $\tilde{G}_{sys}(f)$ is the complex gain of the system under control. $\tilde{G}_{loop}$ is the complex gain of the loop as a whole, including all depicted blocks. While $\tilde{G}_{loop}(f)$ is often a nontrivial function at higher frequencies, we can neglect its frequency dependence by setting the unity gain frequency ten times lower than the -3 dB frequency of the system under control allows us to neglect the frequency dependence of $\tilde{G}_{loop}$. The inversion of the system state monitoring signal adds an additional 180° to the phase of the feedback signal.

Equation 3.1 is an intuitive time-domain description of the PID operation. To quantitatively analyze the performance and stability of the feedback, one typically switches to the frequency domain by way of a Laplace ($\hat{\mathscr{L}}$) transform. The primary frequency-dependent quantities that determine the behavior of a system's response are its complex gain $|\tilde{G}(f)|$ and phase ϕ.

$$\tilde{G}(f) = |\tilde{G}(f)|e^{i\phi} = \frac{\tilde{V}_{out}(f)}{\tilde{V}_{in}(f)} \tag{3.2}$$

$\tilde{V}_{in}(f)$ and $\tilde{V}_{out}(f)$ are the input and output signals respectively. Here, only systems with a linear response to perturbations at a single frequency are considered. For such systems, a single-frequency sinusoidal input signal $\mathrm{Re}[\tilde{V}_{in}(f)]$ of amplitude $|\tilde{V}_{in}(f)|$ will propagate through the system and result in a response $\mathrm{Re}[\tilde{V}_{out}(f)]$ at the same frequency. Only the response's amplitude or phase may differ from the input. The gain of the closed feedback loop as a whole is the product of the gains of each element $\tilde{G}_i(f)$ comprising it (see figure 3.10)

$$|\tilde{G}_{loop}(f)| = \prod_{i=1}^{n} |\tilde{G}_i(f)| \tag{3.3}$$

A rigorous treatment of feedback loops shows that stability is determined by the phase relationship at frequencies near where the magnitude of the total closed loop gain (eq 3.3) is one, or 0 dB [87]. This is the unity gain frequency. In order for correction signals to reduce perturbations from the setpoint, the correction needs to combine destructively with them. This is an example of negative feedback, where the feedback's actions reduce the deviation from a given set point. Positive feedback, where the deviations from the set point are amplified, is undesirable in nearly all cases.

The first step in designing a feedback loop is to find the lowest frequency f_{bad} that should be avoided to ensure stable operation. This informs the design of the PID circuit, the corrective electronics ensuring negative feedback, by putting an upper limit on how quickly it can be allowed to respond to perturbations from the setpoint. The lower limit is typically set by the desire for operation on experimentally relevant timescales. For our purposes, stability means that as the time of operation increases towards infinity, the loop signal's magnitude remains bounded and there is no long-term oscillatory behavior.

Common f_{bad} examples are frequencies where the phase approaches 180°, or at which there is a mechanical resonance in the system to control (e.g. in a laser piezo). A good rule of thumb is to design such that the unity gain frequency (where $\tilde{G}_{loop}(f_{unity}) = 0\,\mathrm{dB}$) is an order of magnitude less than f_{bad}. Doing so ensures that, with a fully characterized loop and within the specified frequency range, the loop is stable. The factor of ten helps account for uncertainties in characterizing the loop's frequency response, essentially trading some level of bandwidth for a higher level of confidence in stability over the decreased range. In the range of frequencies $0 \leq f \lesssim f_{bad}/10$, we can neglect the frequency dependence and any phase shifts of the system being controlled and its complex gain $\tilde{G}_{sys}$. The Arduino slow lock operates at frequencies orders of magnitude lower than most other elements in the loop. We believe that the limiting mechanical resonance of the 922 nm laser system (see figure 3.7) chosen for the first implementation of the Arduino slow lock is that of the laser's diffraction grating peizo with $f_{bad} \approx 100\,\mathrm{Hz}$. At $f \leq f_{bad}/10 = 10\mathrm{Hz}$, we assume the gain of the system begin controlled is constant, and choose a unity gain frequency of 10 Hz.

To characterize the PID control electronics, one would typically make a Bode plot of the system's gain versus signal frequency. This is challenging with the digital Arduino system, as the gain does not decrease in a continuous manner. Rather, the output begins to degrade by digitizing into discrete steps similar to what is shown in figure 3.11. Therefore, we modeled the Arduino lock circuit (with $K_p = 0$) as an integrator with gain:

$$|\tilde{G}_{Ard}(f)| = \frac{1}{2\pi f RC} \tag{3.4}$$

and recorded the time constant ($\tau = RC$) by observing how quickly the signal integrates a constant V_{in} via:

$$V_{out} = \frac{1}{\tau}\int_0^t (V_{in} + c)dt \tag{3.5}$$

for a constant c. Note that although the symbolism RC is still used here to describe the time constant, the integration takes place in code, not using physical resistors and capacitors. This measurement allows us to relate τ to the K_i PID coefficient included in the code, and we found that $\tau = 1\mathrm{s}$ for $K_i = 1$.

3.2.1.2 Ardunio-Lock Details: Hardware

Our lab has traditionally implemented PID locks via analog circuits built around operation amplifiers. These dedicated circuits are still our go-to choice for precise, high-bandwidth applications. However, microcontrolers are also an attractive option for certain projects. Benefits of a microcontroller platform include ease of adjusting parameters (via programming instead of physical components), versatility of design, and the potential for remote control/monitoring.

The *Arduino* platform is a popular open-source family of boards built around 8-bit Amtel® AVR microcontrollers. These boards are designed to be beginner-friendly, have readily available community support, and offer a simplified software development environment. The development environment is based on C++, allowing full use of that language if one chooses. Finally, most of the boards come with native USB support, making it easy to use a conventional computer to interface with them.

Ardunio Type	Uno
Clock Speed (default)	16 MHz
Digital In-Out Pins (0-5V)	14
Analog Input Pins (10-bit)	6
DC Current Per IO Pin	20mA
Flash Memory	32KB
SRAM	1KB
Host Interface	USB

Table 3.2: Arduino Uno specifications of interest for this project. Note that there are no analog output pins native to the device.

There are many potential applications within the laboratory that require continuous monitoring against drifts occurring on the hour to day timescale. An inexpensive, quickly-to-deploy solution would be advantageous. Heaters and voltage controlled oscillators (VCOs) fit this criteria, as do lasers that are already locked to a frequency reference with a high-bandwith lock. In the latter case, there is often a tradeoff between bandwidth and the range of a lock's output. Being able to quickly react to signals often comes at the expense of only being able to work within a narrow range of outputs. For these reasons, we focused our development of an Arduino-based low bandwidth PID lock on controlling a laser's frequency.

After settling on a microcontroller and general application, the next design step is to decide how the controller will interface with the laboratory equipment from which it will be sending and receiving signals. While the Arduino's onboard 10-bit analog to digital converter (ADC) gives a sufficient nominal resolution of $5\,V/1023 \approx 5\,\mathrm{mV}$, the device has no analog *output* channels. Some kind of continuously variable output voltage capability is necessary in order to have fine-control over the lock behavior. We accomplished this by attaching an MCP4745 external 12-bit digital to analog converter (DAC) to the Arduino. The DAC communicates with the Arduino via the I2C serial communication protocol. I2C is a two-wire protocol (serial clock = SCK = pin A5, serial data = SDA, pin A4), that supports multiple devices in a master/slave configuration. This means that the project could be expanded to have one Arduino controlling multiple outputs.

I2C on the Arduino is included in software via the default ”Wire.h” library”. The protocol has a moderate speed ($\sim$10 kBps), and is intended for cable lengths of less than a few meters. These limitations don't present an issue for this project as the lock operates on a few-Hz timescale, and the signal lines between the DAC and Ardunio are on the order of only a few centimeters. If faster communication is needed, there are other communication protocols available (e.g. SPI), as well as the potential for tweaking the timing of various onboard clock rates (e.g. two-wire bit rate, TWBR) to gain additional performance. In this project, the following line of code in the *setup()* function sets the I2C speed. The TWBR number is used to scale the microprocessor's clock rate to derive the I2C frequency [2]:

```
TWBR = 12; // Two wire bit register. Controls the I2C protocol speed
    (SCL).
```

As an example of when the communication and processing rates of the system become a bottleneck, we tested the Arduino+DAC's ability to recreate a waveform at various input frequencies. When the input begins to approach the speed at which the system can process and transmit data, digitization will occur in the output signal, as shown in figure 3.11.

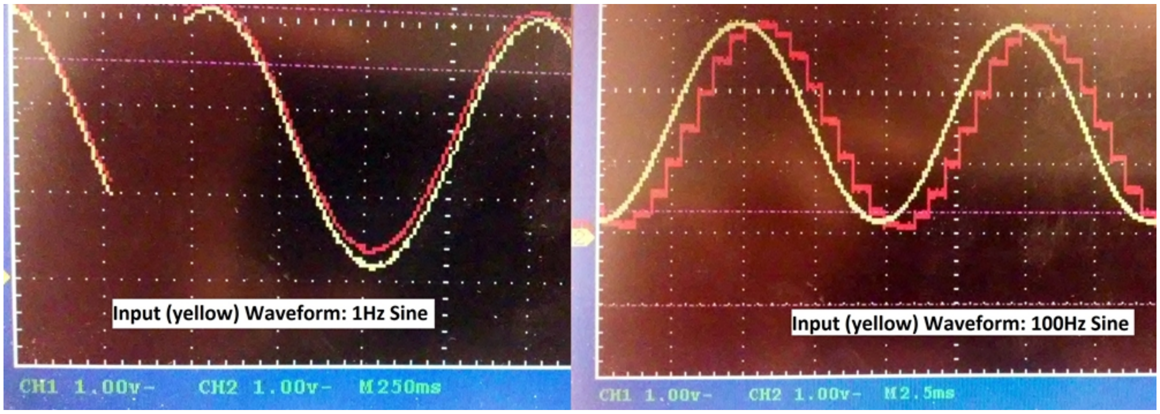

Figure 3.11: Digitization ("stair steps") due to a signal processing and communication bottleneck. Input sine waveform (yellow trace), output waveform (red trace).

We also found that printing to the serial port (USB) can slow down the system's response rate by an order of magnitude, as those clock cycles are diverted from processing the analog input/output.

While the DAC has an absolute maximum output current of 25 mA, the voltage begins to deviate from the calculated ideal after a few mA (see MCP4725 datasheet). Because of this, for applications requiring more than a few mA, another stage (e.g. operational amplifier) is recommended. Many laboratory devices operate outside the

0-5 V range of the system's inputs and outputs. Therefore, some signal conditioning circuitry is necessary if the application's demands exceed 5V. It is also good practice to scale any input signals such that any expected swings in them will span the full range of acceptable inputs. This ensures maximal available resolution.

3.2.1.3 Conditioning Circuitry

Many typical use-cases in the laboratory will require scaling of the input and output voltages to and from the Arduino lock. Moreover, since this lock is intended to operate on signals with frequencies of about 1 Hz, it is desirable to filter out any high frequency components that make their way onto the output. Additional analog scaling and filtering circuitry perform this function.

To scale up any input signal and take advantage of the full ADC range, we used a non-inverting op-amp gain stage. To protect against unexpected overvoltage input conditions, a 5 V Zener diode was included as a voltage clamp. This diode will conduct at voltages over 5 V shunting extra current to ground and clamping the signal at a safe maximum.

On the output, a series of low-pass filters (3 dB frequencies of 30 Hz and 3.3 Hz) strongly reduce the amplitude of high frequency noise, an adjustable voltage divider allows scaling of the signal, and a transimpedance amplifier buffers the final output. This output stage is pictured schematically in figure 3.12. The 3.3 Hz low pass filter was included after the initial construction to further suppress high-frequency voltage noise observed on the circuit output. The observed noise was approximately 30 mV peak-to-peak, and we made the decision to sacrifice additional lock bandwidth to reduce it further. Specifically, the 3.3 Hz filter necessitated a reduction of the the originally-designed unity gain point, with a new value less than one Hz. In practice, this change is acceptable due to the 922 nm laser's drift timescale of approximately twenty minutes.

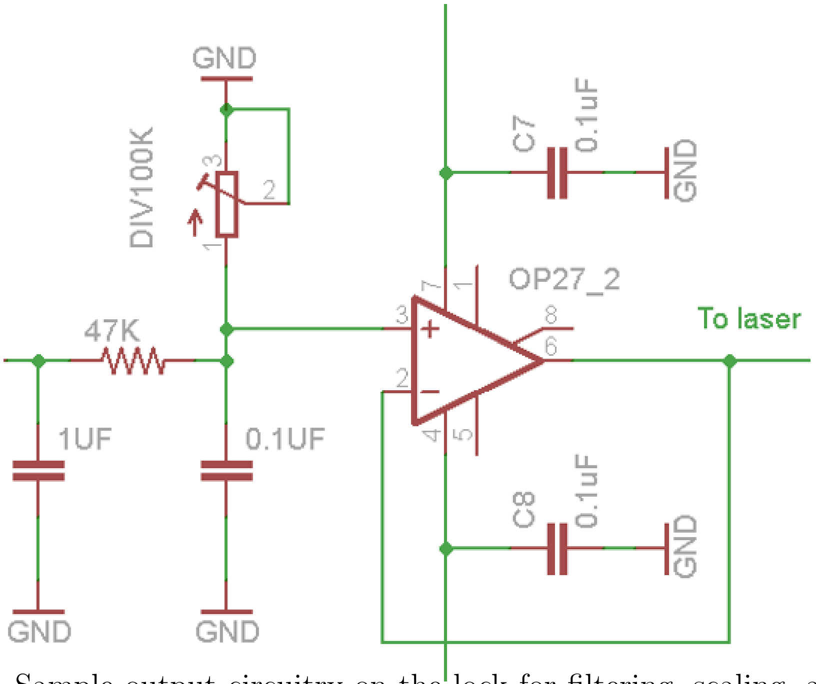

Figure 3.12: Sample output circuitry on the lock for filtering, scaling, and buffering the signal prior to being sent to the device under control by the lock.

Including an LCD screen and enable/disable switch complete the project's hardware at a general level. The screen gives a quick visual indication of the state of the lock; whether it is engaged or not, and the level of its signals with respect to their maximums.

3.2.1.4 Arduino Shield

To aid in the quick deployment of these slow locks as needed within the laboratory, we made an Arduino-Uno compatible "shield" which would contain most of the auxiliary electrical components. A shield is a specialized printed circuit board with appropriately spaced pins to fit on top of, and make contact with, the Arduino's rows of header pins. The advantage of a shield is that it takes up less space, provides a simple template for circuit construction, and can be easily swapped for a new one if something is damaged. The shield includes all of the aforementioned scaling, protection, and buffering hardware, as well as a unity-gain differential amplifier (AMP03) immediately prior to and after the Arduino. The purpose of the AMP03 was an attempt to separate the potentially noisy digital (Arduino) ground from that of the analog components sending their signal to the instrumentation. Images of the shield details are available in the appendix.

When locked and powered via a quality 120 VAC to DC wall-adapter, the circuit's output had acceptable noise characteristics for our applications of about 20 mV peak to peak. Including the shield and LCD, the entire package can be constructed with a size less than 3.5" ×3" ×3".

3.2.1.5 Ardunio-Lock Details: Software

This project takes advantage of open-source code such as the PID library written for the Arduino by Brett Beauregard[16]. At the time of this writing, the library was on version 1.2.1. Digging into the library's code (`PID_v1.cpp`), one can see the explicit implementation of the PID algrithm:

```
/*Compute all the working error variables*/
      double input = *myInput;
      double error = *mySetpoint - input;
      double dInput = (input - lastInput);
      outputSum+= (ki * error);
      .
      .
      .
      double output;
      if(pOnE) output = kp * error;
      .
      .
      .
      /*Compute Rest of PID Output*/
      output += outputSum - kd * dInput
}
```

The project also utilizes libraries to communicate with the LCD screen, and MCP4725 DAC[1]. The code is largely self explanatory, consists of simple commands with online documentation, and has been significantly commented for clarity. There are a few minor modification made to the PID library itself (files `PID_v1.cpp` and `PID_v1.h`). These modifications allow the error signal computed by the PID library, to be manipulated in the Arduino programming environment. It is necessary to force the error value to zero when the Arduino is not locked (e.g. while the lock is under manual control) to keep an error signal from accumulating. A large accumulated error signal is detrimental to lock acquisition if present when the PID is engaged. In addition to the Arduino code, I have included the changes made the the library files in the appendix.

3.2.1.6 Specific Implementations

This system has been implemented a few times the Killian Lab and I describe the first implementation here as an example. The initial use was as a compliment to the existing analog PID lock controlling the frequency of our 922 nm laser that is subsequently frequency doubled. The analog lock feeds back to the laser's current, which can counteract small quick perturbations in frequency. The electronics would drift out of their locking range on a timescale of a few hours, requiring manual intervention. Using the Arduino slow lock to feed back to the PZT controlling the diffraction grating in this Littrow-configuration ECDL constitutes a second feedback path that is much slower to respond, but has a much larger working range. This configuration extended the time that the system would stay locked to approximately 24hrs.

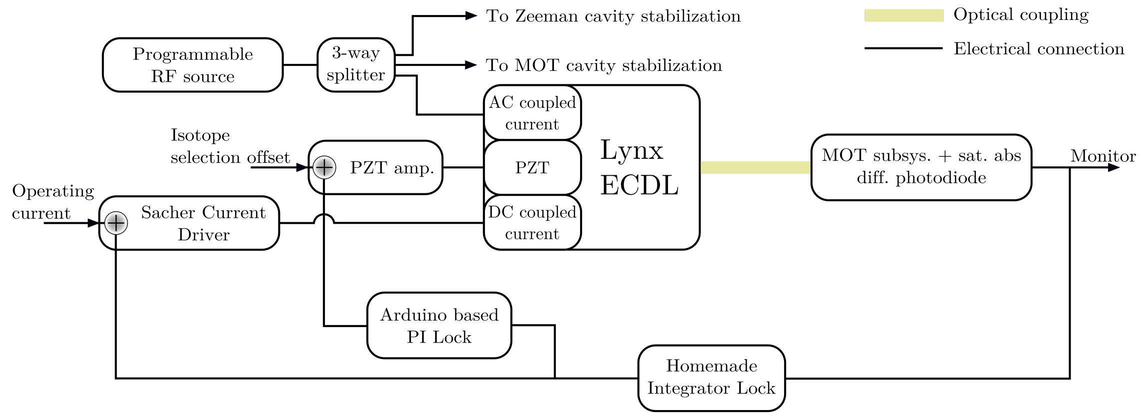

Figure 3.13: 922nm laser frequency stabilization system. Schematic from J. Aman's PhD thesis [4]. The Arduino slow lock is installed as a second feedback path, complimenting the existing analog integrator.

After quantifying the responses of the slow-lock circuit and existing laser system, we then set the unity gain frequency of the entire 922nm-system loop (slow lock included). Using equations 3.3 and 3.4, we found that the unity gain frequency was approximately 3Hz with the integration PID coefficient at $K_i = 1$. To account for the additional noise-reducing 3.3 Hz low-pass filter added to the control electronics' output, the unity gain point was further reduced by about an order of magnitude by lowering K_i to 0.8. Then we tweaked K_p (final value = 0.2) to remove any small constant offsets that would otherwise integrate to the circuit rails because of the integrators infinite DC gain. The derivative term K_d was set to zero. This term helps to avoid overshoot and other lock-acquisition issues, but is generally not critical in most of our applications.

3.2.2 Infinite sample and hold

Injection-locked slave diodes, seeded by a stable master laser, are a common tool in the lab for modestly increasing the optical power available. One particular example is the

Neutral apparatus “spectroscopy” slave, which is a multipurpose system operating on the 689 nm ($^1S_0$ - $^3P_1$) atomic transition. While performing two-photon spectroscopy with it [5], we found that the laser power stabilization electronics were struggling to acquire and lock during PA-beam exposure times shorter than about 70 ms. To overcome this, and enable shorter exposures, I built an infinite sample and hold (ISH) circuit [97]. The ISH name stems from the device's ability to continuously sample a voltage until triggered, then hold its output at the last sampled level for long times without change. Because the voltage level is stored as digital information (vs a traditional capacitor), it is immune to droop over time (hence “infinite”).

The circuit has a short acquisition time (roughly 5 μs), and is based on an ADC+DAC pair comprised of an LTC1417 and LTC1658 respectively. Both are low-power, 14-bit devices that communicate with each other via a serial line, and the ADC (LTC1417) samples at 400 ksps. The completed circuit's inputs are a TTL pulse from our experimental timing hardware, and a spectroscopy beam photodiode signal for monitoring optical power. The circuit provides a means of sampling the laser diode's output before application to the atoms, holding at this value, then pulsing (over an order of magnitude more quickly) an AOM to illuminate the atoms at the appropriate power.

The LTC1417 has an onboard voltage reference of 4.096 V, and this limits the range of inputs to that value, though the chip's datasheet details ways to increase this. For each sample, the circuit requires a square wave input to the CONVST (conversion start) pin. The TTL signal switches the input of this pin from a constant 5 V (hold mode) to a 250 kHz square wave from a MAX1697U (sample mode). I built a printed circuit board to buffer and scale the input/output voltages, in addition to containing all the digital circuitry. A circuit schematic and printed circuit board image are included in the appendix.

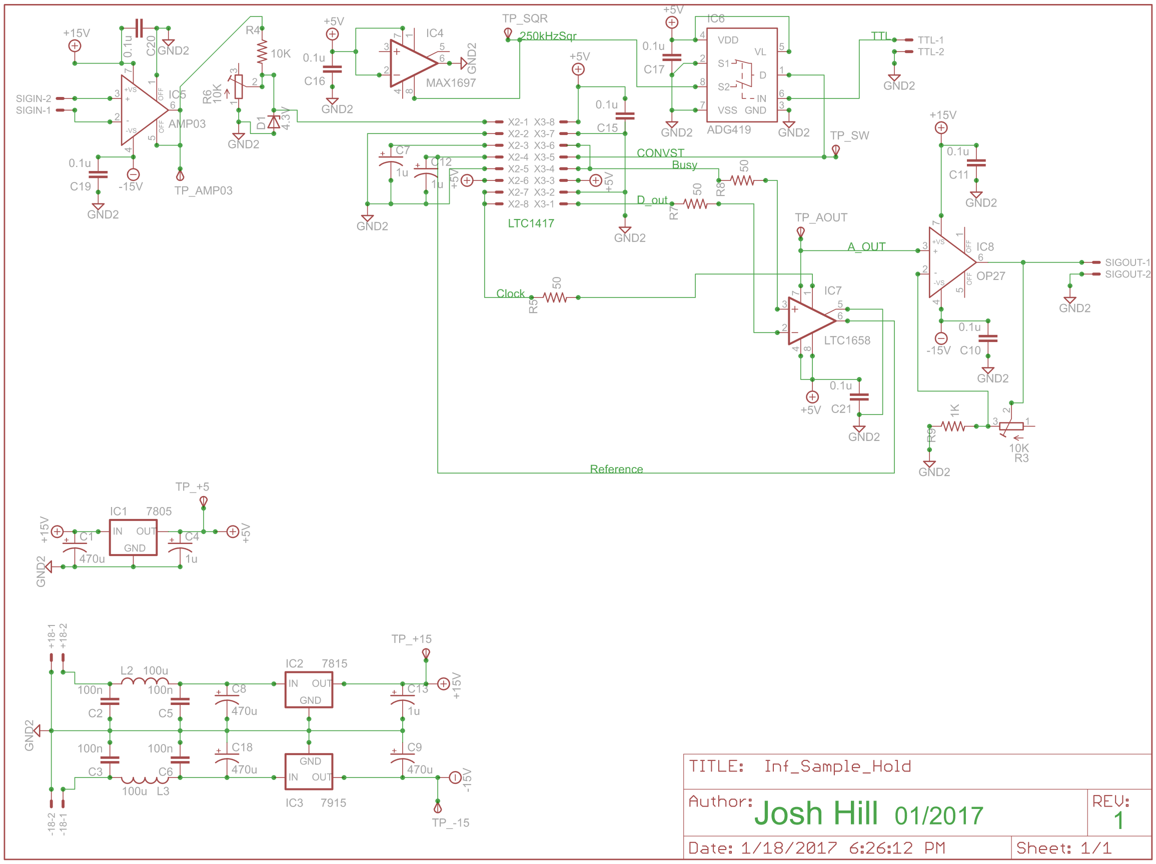

Figure 3.14: Schematic board for the infinite sample and hold device. Note that the LCT1417 did not have a through-hole option at this time, and required a breakout board to convert the surface-mount SSOP16 package to DIP.

The resulting circuit functions well. When combined with a shutter, power lock electronics, and AOM, it was successfully used to apply 698 nm spectroscopy pulses to the atoms with times as low as a few hundred μs. For more details on the specific timing of this experimental sequence, see section 2.3.4.2 of J. Aman's PhD thesis [4].

Chapter 4

Binding Energies

When quantifying a particular PA resonance, two fundamental quantities are of primary interest. The first quantity is the PA resonance frequency, and thus the binding energy of the created molecule. The second interesting quantity is the "strength" of the resonance, e.g. how much signal is observed for fixed excitation laser detuning and intensity, as well as sample density. The former is what I report in this chapter. A subsequent thesis chapter will discuss details for quantifying the resonance strengths, and relating them to fundamental parameters such as the molecular wavefunction.

In a manner analogous to the coupling of angular momenta in an atom, there exist various coupling regimes (Hund's cases *a,b,c...*) determining which momenta couple most strongly, and therefore which set of quantum numbers are "good" for that basis. The additional complexity of molecules also allows for a significant number of possible symmetries. There exist a few different conventions for encoding all this information into a set of term symbols [92][17]. Here, we describe molecular states using the notation for Hund's case (a) [9]

$$^{(2S+1)}\Lambda^{+/-}_{g/u} \tag{4.1}$$

The projection of the molecule's electronic orbital angular momentum onto the internuclear axis is denoted by $\Lambda \in \{\Sigma, \Pi, \Delta ...\}$. In addition, g/u describes the wavefunction being even (g), or odd (u) under an inversion of the electron coordinates through a center of symmetry. For Σ states, $+/-$ describes whether the state wavefunction changes sign ($-$), or not ($+$), under reflection about a plane containing the internuclear axis. S is the total electronic spin of the molecule. In this work, we use PA spectroscopy to excite ground-state atoms from the scattering continuum above the $5s^2\,{}^1\mathrm{S}_0$ - $5s^2\,{}^1\mathrm{S}_0$ ${}^1\Sigma_g^+$ ground potential to various bound molecular vibrational states confined to the $5s^2\,{}^1\mathrm{S}_0$ - $5s5p\,{}^1\mathrm{P}_1$ ${}^1\Sigma_u^+$ excited potential. In most instances hereafter, I will drop the atomic constituent prefix notation of the molecular potentials, and only refer to them as ground or excited.

4.1 Molecular Potentials

This chapter presents our measurements and analysis of molecular binding energies on the excited potential in ^{84}Sr (bosonic), ^{86}Sr (bosonic), and ^{87}Sr (fermionic) via photoassociation spectroscopy. Binding energies ($E_\nu > 0$) are identified by their vibrational quantum number ν and reported in GHz detuned from the $5s^2\,{}^1\mathrm{S}_0$ - $5s5p\,{}^1\mathrm{P}_1$ asymptote of two well-separated atoms (e.g. of dissociation energy D). Detuning $\Delta = (f_{PA} - D/h) < 0$ of the photoassociaton laser with frequency f_{PA} is reported from the same reference. Absolute energies are reported in spectroscopic wavenumbers ($\widetilde{\nu} = 1/\lambda$) which have conventional units of cm^{-1}. Note that $0.001\,\mathrm{cm}^{-1} \times \mathrm{hc} \sim 1.986 \times 10^{-23}\mathrm{J} \sim \mathrm{h} \times 29.98\,\mathrm{MHz}$, where h is Plank's constant and c is the speed of light in vacuum.

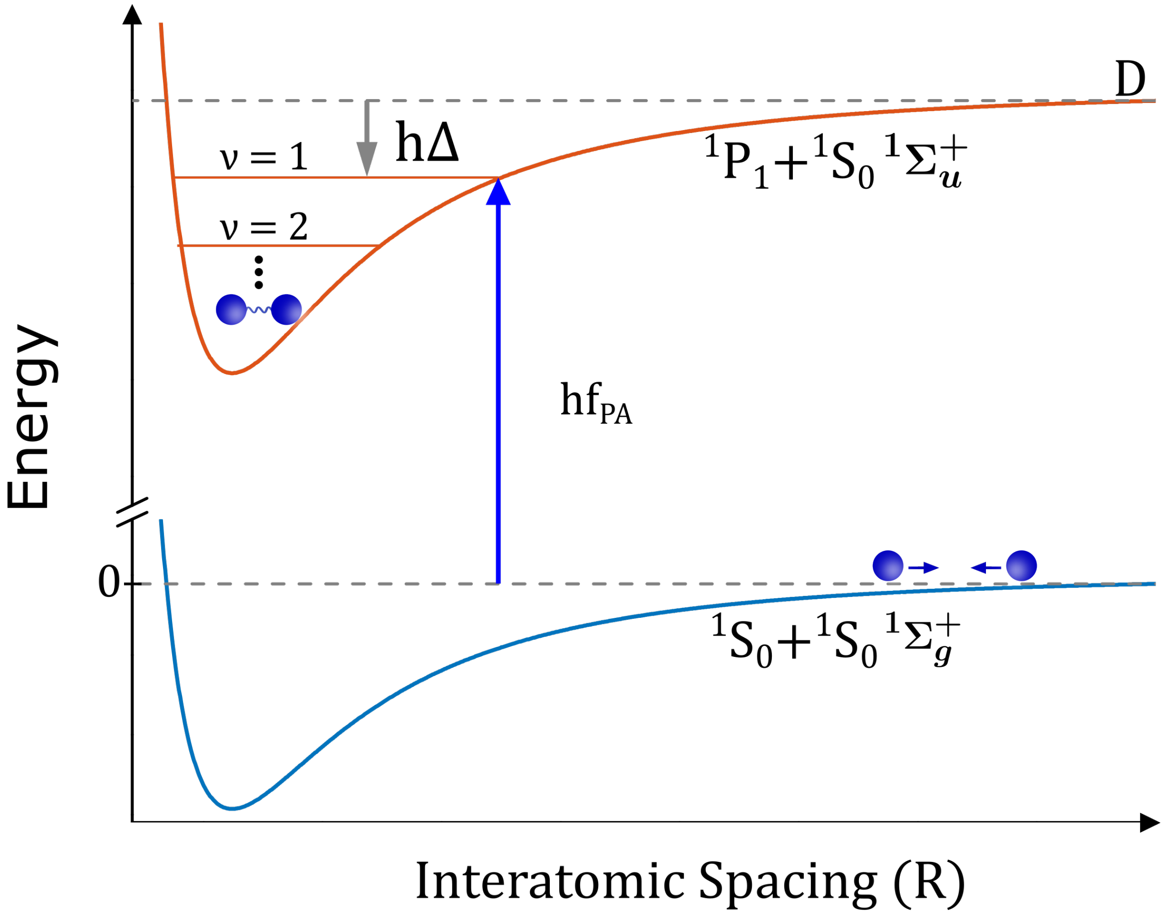

Figure 4.1: Qualitative diagram of the interatomic energy potentials relevant to the photoassociation discussed in this thesis. Note that we neglect the $\sim 2\,\mu$K $\sim 60\,$kHz thermal energy of the colliding ground-state pair.

Consider two neutral strontium (SrI) atoms each in their $^1S_0$ ground-state with a large internuclear separation R. At large R, the atoms interact primarily via an attractive van der Waals potential proportional to the C_6 dispersion coefficient ($C_6 \sim 3170$ atomic units $\sim 1.50 \times 10^{-7}\,\mathrm{cm}^{-1}\text{Å}^6$) [105]

$$V_g(R) = D - \frac{C_6}{R^6} \tag{4.2}$$

Note that we neglect the $\sim 2\,\mu$K $\sim 60\,$kHz thermal energy of the colliding ground-state pair.

Nominally, there is an additional term to eq. 4.2 representing the centrifugal barrier characterized by the molecular angular momentum quantum number l of the incoming scattering states, the reactants.

$$+\frac{\hbar^2}{2\mu}\frac{l(l+1)}{R^2} \tag{4.3}$$

The size of this barrier is important to determining which partial waves ($l \in 0, 1, 2...$) can contribute to the interaction (reaction). For low enough temperatures (and thus kinetic energies), higher order waves cannot enter the interaction region and contribute. At the ultracold temperatures of our samples, only $l = 0$ (s-waves) contribute. To confirm this, one can set the derivative of the sum of eq. 4.2 and eq. 4.3 equal to zero, and solve for the internuclear spacing of the barrier peak. For $l = 1$ this separation is about 7.37 nm, at which point the barrier height is about 275 μK, which is two orders of magnitude larger than our $\sim 2\,\mu$K samples. Therefore we have confidence that only the lowest order partial waves are interacting in our case.

Photoassociation light detuned lower in energy ("red") of the ${}^1S_0$ -${}^1P_1$ atomic transition excites two atoms from the scattering continuum above the ground molecular ${}^1\Sigma_g^+$ potential given by eq 4.2, to bound molecular (homonuclear dimer) states confined to the ${}^1\Sigma_u^+$ molecular potential $V_e(R)$. The latter potential constitutes an attractive resonant dipole-dipole interaction [123]. Stein et al. estimate the total number of bound states on this excited potential to be 350 ± 50 [105]. The same team also studied the long-range portion of the ground-state potential, quantifying the dispersion coefficients that characterize it [106]. As illustrated in figure 4.1, the excited potential connects asymptotically to the $5s5p\,{}^1P_1$ state in the dissociation limit. The resonant excitation condition is satisfied when PA laser photons have an energy equal to the difference in energies between that of a particular bound molecular state and the ground-state scattering atoms.

For large internuclear separations, V_e takes the form

$$V_e(R) = D - \frac{C_3}{R^3} + \frac{\hbar^2}{2\mu}\frac{J(J+1)+2}{R^2} \tag{4.4}$$

where μ is the molecule's reduced mass, and J is the total molecular angular momentum of the excited molecular state [69]. The C_3 dispersion coefficient is related to fundamental constants and *atomic* properties via

$$C_3 = \frac{3\hbar\lambda^3}{16\pi^3\tau} \tag{4.5}$$

where τ is the lifetime of the excited atomic ${}^1\mathrm{P}_1$ state. In the regime of low collision energies and large internuclear separations that we study, molecular properties are often relatable to those of the bare atomic constituents. This is a useful conceptual tool, and can simplify the theoretical analysis of the molecule's behavior.

In general, the final rotational term in eq 4.4 depends on the specific molecular potential under consideration [15] [74] [132]. Three additional ${}^1\mathrm{S}_0$ - ${}^1\mathrm{P}_1$ potentials exist, but have either insufficient coupling to be an appreciable contributor to the signal (e.g. repulsive potentials with no discrete states) or are inaccessible due to a combination of selection rules, symmetry considerations, and the collision energies (temperatures) involved [69] [55]. Moreover, we only consider single-photon processes here, and neglect retardation effects [110][57][76]. This approach is consistent with other studies in Sr [130][75][85], Ca [133][30], and Yb [113][119][44].

It is instructive to estimate the contribution of the rotational term in eq 4.4. The term's largest relative contribution to the overall potential will be at an internuclear separation corresponding to the outer turning point of the excited-state's motion. For the PA resonances we measure, this separation is approximately $80 - 240\, a_0$.

where $a_0 = 5.292 \times 10^{-11}$ m is the Bohr radius. For these separations, and restricting consideration to $J = 1$ rotational quanta for reasons discussed earlier, the rotational term is about four orders of magnitude smaller than the $-C_3/R^3$ interaction term, and can safely be neglected.

4.2 Detecting Molecules

What is the experimental signature of spectroscopic PA molecule creation and how do we assign a binding energy to the resonance? This section will address those questions, and provide details about our measurement protocols. All of the the binding energy data presented in this thesis are from PA loss spectroscopy of ultracold ($T \sim 1\,\mu$K) Sr atoms confined in an optical dipole trap (ODT). We detect a PA resonance by scanning an excitation laser that is red detuned with respect to the atomic ^{1}S$_0$ - ^{1}P$_1$ transition ($\lambda \sim 461$nm) and subsequently measuring the characteristic loss of atoms from the trap as a function of frequency (fig. 4.2). The PA loss's dependence on detuning Δ and the square of atom number density n^2, enable us to distinguish it from other loss mechanisms.

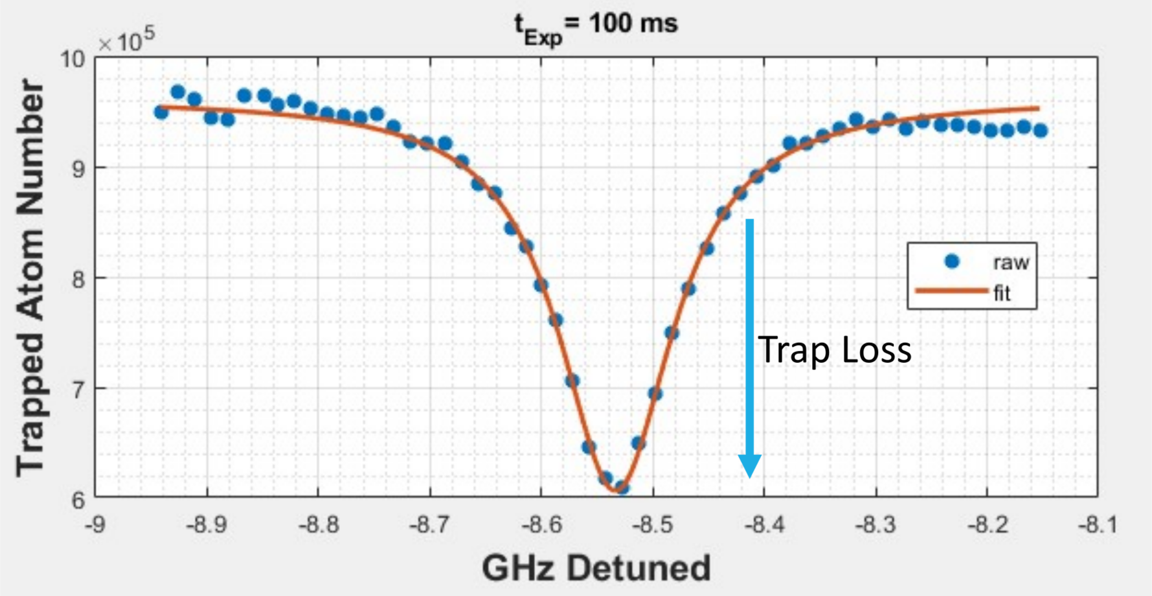

Figure 4.2: Representative example of a spectroscopic PA signal. Data (blue dots) showing loss of atoms from the trap and fit (red line) to a Lorentzian lineshape with center frequency ~ 8.53GHz. This particular data is the average of three scans (runs through the full frequency range) each with the PA laser applied for 100 ms.

There are two primary trap-loss mechanisms which indicate PA is occurring. First, a molecular state confined to the $V_e(R)$ excited potential can decay via spontaneous emission back into two ground-state atoms with greater kinetic energy than the initial colliding pair. Second, the excited molecule can change states to one confined to a different molecular potential that is repulsive (energy decreases with increasing R). In both cases, the products (molecule or atoms) obtain additional kinetic energy. This energy is then greater than that of the confining optical trap (its "depth") and sufficient for the products to be lost from it. For the ~ 1W of $\lambda = 1064$nm light used in these PA experiments, the optical dipole trap's depth is on the order of $8\,\mu$K.

The measurement of a particular resonance frequency requires a balance between the excitation laser's intensity I and exposure time. Higher intensity leads to more heating due to off-resonant scattering at a rate γ, while longer exposure times decrease the trapped atom number as they are lost from the ODT due to both off-resonant scattering, and background gas collisions at a rate of γ_{bg}. Moreover, because both the heating of the sample and the strength PA resonances are dependent on the detuning, this balance must be adjusted across the range of detunings studied to produce a measurable signal while minimizing the sample distortion.

4.2.1 Binding Energy Extraction from Spectra

To determine binding energy E_ν of a particular PA resonance with vibrational quantum number ν, the corresponding spectroscopic loss data for a fixed PA laser intensity and exposure time are fit to a phenomenological Lorentzian lineshape with a linear background.

$$N(f) = \frac{P_1 \frac{P_2}{2\pi}}{(P_3 - f)^2 + (\frac{P_2}{2})^2} + P_4 f + P_5 \tag{4.6}$$

Where P_1 through P_5 are fit parameters corresponding to amplitude, width, center frequency, linear slope, and linear offset respectively. Laser jitter is the dominant broadening mechanism, and no effort was made to account for molecular-state ac Stark shifts from the optical dipole trap or PA laser fields. We intentionally chose exposure times and intensities such that the atom loss was approximately 10 - 50%: i.e. far from loss saturation. This model is sufficient to extract the primary quantity of interest ($P_5 = E_\nu/h$) given the ± 30 MHz overall frequency uncertainty of the PA laser locking scheme.

Studies of the resonance's dependence on exposure time will be discussed in a following chapter, where a model will be introduced that relates the loss-spectra to to-body collisional molecular effects. Additional data and this subsequent model of the two-body collision processes will be used to quantify PA resonance strengths and underlying physical parameters.

4.2.2 Differential Energy Measurements and Frequency Lock

In order to measure various PA resonances, a well-defined energy reference is required. Afterwards, detunings of the PA laser can then be quoted with respect to that level. The natural reference for this work is the energy of the $5s^2\,{}^1\mathrm{S}_0$ - $5s5p\,{}^1\mathrm{P}_1$ atomic transition. The molecular potential described by eq. 4.4 connects to this level in the asymptotic case of large internuclear separations. We quote binding energies as the difference between the observed PA molecular resonance, and the atomic transition appropriate for each isotope. For each isotope, we measure the corresponding asymptotic transition energy on a Moglabs FZW600 wavemeter by periodically tuning the PA laser to atomic resonance. Then, after heavily attenuating the beam, we used loss spectroscopy to verify the atomic resonance wavelength. Such measurements also allowed us to quantify our frequency uncertainty as $\pm\,30\,\mathrm{MHz}$.

The wavemeter also has the useful function of being able to return a PID correction signal based on the difference between its optical input and a software-defined setpoint. We took advantage of this functionality by setting up a feedback loop whereby the device's correction signal was fed back to the laser's diffraction grating, providing wavelength stabilization (fig. 4.3). Including the PA laser wavelength setpoint in the LabView experimental control VI was the method by which we programmatically scanned the laser's wavelength. The wavemeter's reported value is taken as the independent variable in our measurements. In the locked-loop configuration, the meter's least significant digit fluctuates at the $\pm\,0.0005 = 15\,\mathrm{MHz}$ level from shot-to-shot, possibly due to mechanisms internal to the laser or meter itself, or PID control voltage jitter. These fluctuations dominate other possible broadening mechanisms such as 1064 nm and 461 nm AC stark shifts, the sample's thermal energy distribution, etc., and are comparable to the uncertainty in measuring the atomic asymptote energy. A more sophisticated feedback system could reduce these effects, but the current setup is adequate for the studies conducted in this thesis.

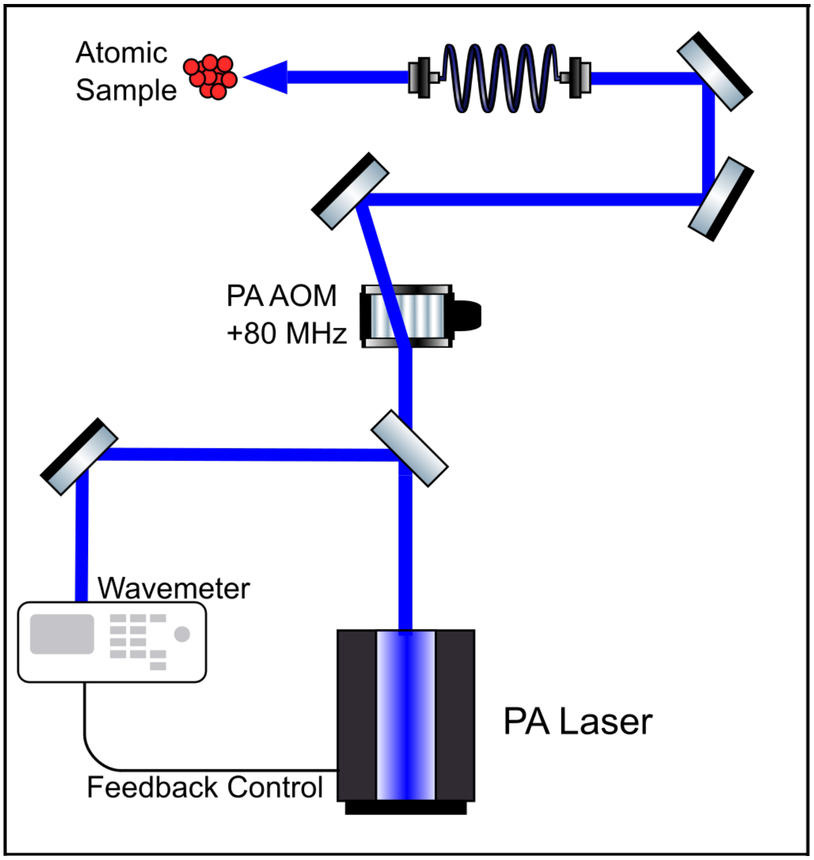

Figure 4.3: Simplified schematic of PA beam path for exciting resonances and monitoring frequency on the wavemeter. Beam shaping optics are omitted, and can be found in figure 2.3.

4.2.3 Wavemeter Absolute Calibration

Though our binding energies are measured as differences between the PA transition and the appropriate atomic resonance, there are times when it is advantageous to measure absolute frequencies, as opposed to frequency differences. These measurements serve as a monitor of any drifts in the wavemeter (and their timescale), as well as a double check of any frequency offsets (e.g. AOMs) in the system. Because the meter does not have an internal absolute frequency reference such as a He-Ne laser, one must be supplied by sending light of a known frequency to it. For example, a beam locked to an atomic transition could serve as a known reference. Then, the meter can be calibrated by entering the known numerical value for the reference frequency into the device's internal calibration software routine.

We have found that the meter's measurements at one frequency do not remain accurate to our desired level when a point significantly far away from the previous calibration value is measured (e.g. changing from $\lambda = 461\,\mathrm{nm}$ to $689\,\mathrm{nm}$). As the meter is a shared instrument, such changes occur often. Therefore, for measuring absolute frequencies, it is important to have reference light available with a frequency close to the region of interest. Conveniently, such a reference is available to us in the form of a laser independent from that used for PA excitation. This second laser source is wavelength-locked to any appropriate Sr isotopic resonance of the $^1\mathrm{S}_0$ - $^1\mathrm{P}_1$ transition using Doppler-free saturated-absorption spectroscopy in a strontium-filled heat pipe. The $\lambda \sim 461\,\mathrm{nm}$ Zeeman slower, MOT, and 2D transverse collimation trapping and cooling stages are also derived from this independent ("461 nm master") laser. Therefore, the sampled calibration light has the same wavelength as the output of the master laser and the 2D collimation beams (fig. 4.4) [20].

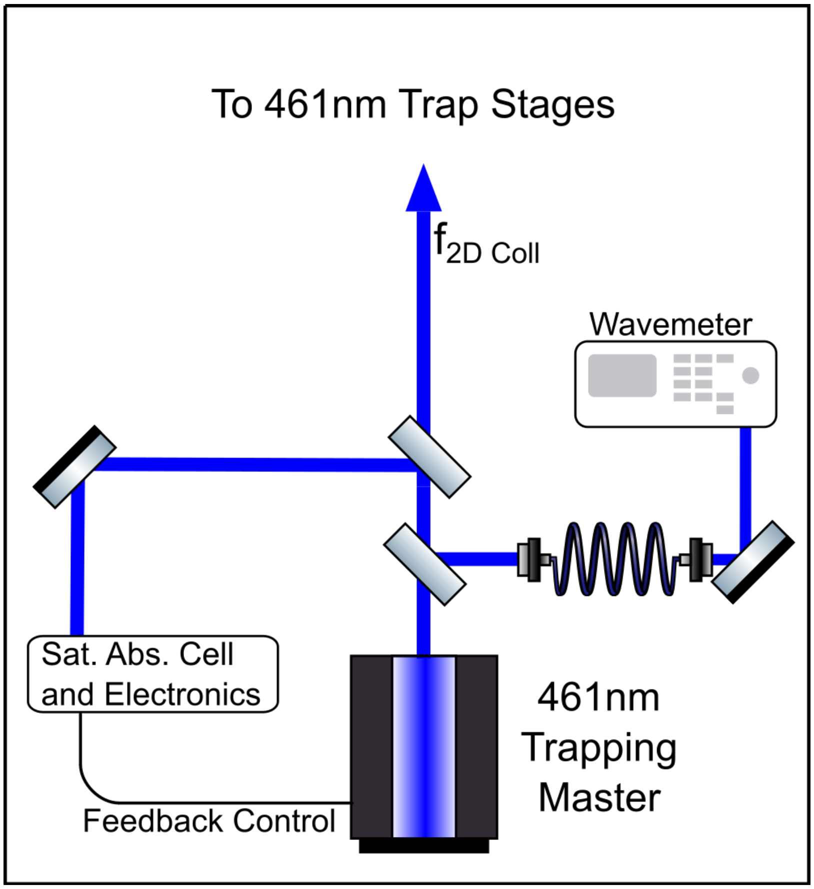

Figure 4.4: Simplified schematic of beams relevant to the frequency calibration of the wavemeter. Beam shaping optics are omitted, and can be found in figure 2.3.

A standard literature reference gives the value of this transition for neutral strontium (SrI) with natural isotopic abundance as $21698.452 \pm 0.004\,\mathrm{cm}^{-1}$ [101]. The isotope and hyperfine structure (for fermionic species) shift the value as shown in table 4.1.

Isotope	**Shift From ^{88}Sr (MHz)**
^{88}Sr	0
^{87}Sr ($F = 7/2$)	-12
^{87}Sr ($F = 11/2$)	-55
^{87}Sr ($F = 9/2$)	-78
^{86}Sr	-125
^{84}Sr	-271

Table 4.1: Isotope shifts of the $^1S_0$ - $^1P_1$ transition with respect to the same transition in the most abundant isotope, ^{88}Sr. Individual hyperfine levels are shown for fermionic ^{87}Sr [35][19]. Note that the hyperfine splitting, labeled by total angular momentum quantum number F, is on the order of the molecular transition's natural linewidth ($\gamma_{mol} \approx 60\,\mathrm{MHz}$) [68]. Our PA laser resolution is comparable to the hyperfine shift, and we do not resolve the individual levels. Therefore, detunings for ^{87}Sr are quoted from the centroid (as defined in [42]) at -52.1 MHz.

We perform the wavemeter calibration by locking the 461 nm master's wavelength to the isotope of interest, connecting the fiber carrying its light to the meter, and then entering the known value for the atomic transition frequency into device's software. This known value is $21698.452\,\mathrm{cm}^{-1}$ offset by any isotope shift (see table 4.1) and a $+95\,\mathrm{MHz} = 3.17 \times 10^{-3}\,\mathrm{cm}^{-1}$ experimental shift due to the hardware configuration. The hardware shift is the combination of an offset due to the +1 order of the 80 MHz AOM controlling PA light going to the atoms, which light to the wavementer from the PA laser does not encounter (see fig. 4.4), and the master laser being $\gamma_{atomic}/2 \sim 15\,\mathrm{MHz}$ below the atomic resonance to which it is locked [20]. From this point, the wavemeter is calibrated such that it will display the wavelength of PA light on the atomic sample.

4.2.4 Example Spectra and Frequency Binning

An example spectrum of a single ^{84}Sr PA resonance being fit to eq. 4.6 is shown in fig. 4.5. The figure presents the data before and after binning into 15 MHz wide frequency-bins. Unless otherwise noted, all data in this thesis are frequency-binned at that level prior to fitting. The binning occurs in post-processing; all raw data points are permanently recorded. Multiple passes though the frequency range, as well as multiple points falling into one bin during a single pass, are averaged. The respective standard deviation in atom number is incorporated into the experimental uncertainties.

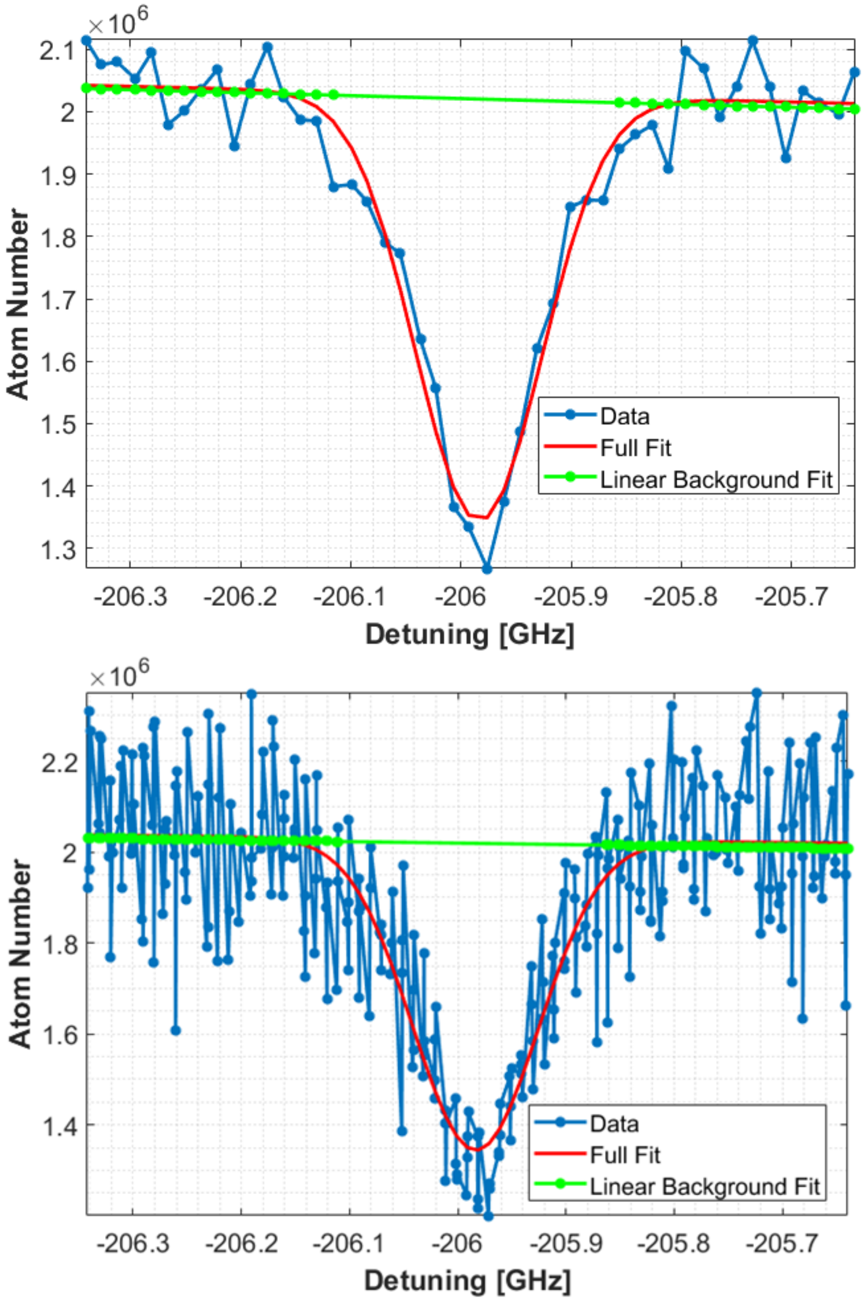

Figure 4.5: Example spectrum of a single ^{84}Sr PA resonance being fit to a Lorentzian lineshape. The same data are shown before (lower plot) and after (upper plot) binning into 15 MHz wide frequency bins. The green fit curve indicates only the linear background, fitting points away from the line center. This linear-only fit is used to generate guesses for the P_4 and P_5 fit parameters in eq. 4.6. The full eq. 4.6 fit (shown in red) is then used to determine the center frequency.

4.2.5 Atomic Sample Before PA

Immediately prior to PA excitation, the atomic sample is confined in a crossed optical dipole trap (ODT). As described in chapter two, the atoms are trapped at the intersection of two elliptical $\lambda = 1064\,\text{nm}$ beams propagating perpendicular to gravity. Each beam has an approximate e^{-2} radius size at the atoms of $30\,\mu\text{m}$ vertically and $130\,\mu\text{m}$ horizontally. The optical power of each beam is reduced to about 1.2 W over the course of 300 ms (forced evaporative cooling), and then held at that power for an additional 200 ms (free evaporative cooling). The evaporation stages were used primarily to allow the sample to reach both equilibrium and a temperature of $\sim 1.8\,\mu\text{K}$. No attempts were made to cool any isotopic species to quantum degeneracy.

Approximating the trapping potential as an infinite harmonic well is valid for deep trapping potentials and cold samples. In this regime, small displacements from the potential minimum allow measurements of the frequency f_T at which atoms oscillate in the trap. This is a useful technique for quantifying the potential energy landscape the atoms experience [4] [41]. Though there are a few possible oscillation modes that could be excited, only sloshing (center-of-mass) oscillations are quoted in this thesis. These frequencies can then be related to various sample and trap properties, including the confining beams' size at the atoms. This independent check of the latter quantity is especially useful since physical access to the trapping location is complicated by the enclosing vacuum chamber.

Table 4.2 summarizes the important ODT and sample parameters immediately prior to application of the PA laser. Any differences between trap powers used for various isotopes are described by the trap frequencies. Note that the trap used for ^{84}Sr was sufficiently separated in time from the others that realignment of the beams took place in the intervening period, changing the measured trap frequencies.

	f_x [Hz]	f_y [Hz]	f_z [Hz]	$N_0 \times 10^6$	T [μK]	$n_0 \times 10^{13}$ [cm^{-3}]
^{84}Sr	81	30	406	4.5	1.9	1.7
^{86}Sr	61	76	388	1.2	1.8	1.1
^{87}Sr	68	85	433	2.3	1.8	2.1

Table 4.2: Summary of important ODT and sample parameters immediately prior to application of the PA laser.

4.3 Modeling the Binding Energies

For rotationless ($J = 0$) potentials described by eq. 4.4, LeRoy and Bernstein derived an analytic semiclassical expression for the binding energies of bound vibrational states close to the dissociation (D) limit in terms of D and C_3 [65]. Originally derived for general $1/R^n$ potentials, we focus on the $n = 3$ case here, neglecting higher-order dispersion terms [66]. Should a regime that warrants incorporation of such corrections be explored, others have performed theoretical work extending equation 4.7 [25]. The LeRoy Bernstein relation has found wide application across PA spectroscopy experiments studying various elements, including heteronuclear dimers [130] [133] [113] [43]. For our potential of interest, the expression is

$$E(\nu) = D - [(\nu_D - \nu)H_3]^6 \tag{4.7}$$

where μ is the reduced mass, ν is an integer vibrational index, ν_D is a non-integer ($0 < \nu_D < 1$) effective vibrational index of the dissociation limit. The integer ν index counts down from the asymptote (smaller binding energies for smaller index numbers), beginning at $\nu = 1$ for the least bound state. The constant H_3 depends on the reduced mass μ, and $\Gamma(x)$ is the gamma function acting on an argument x.

$$H_3 = \frac{1}{\sqrt[3]{C_3}} \cdot \frac{\hbar\Gamma(\frac{4}{3})}{2\Gamma(\frac{5}{6})} \left(\frac{2\pi}{\mu}\right)^{1/2} \tag{4.8}$$

Using eq. 4.7 to fit a sequence of experimentally determined binding energies is straightforward. This is accomplished by performing a combined fit of all data (^{84}Sr, ^{86}Sr, and ^{87}Sr) using a common value of C_3 as a fit parameter and independent values of ν_D for each isotope. Next, the sequence of ν values are chosen to yield $0 < \nu_D < 1$. In this way we are able to unambiguously assign a vibrational quantum number ν to a particular spectral line.

4.4 Data and Discussion

With an atomic sample held in the beams of our characterized ODT, we are now ready to apply the PA excitation laser. This excitation laser's intensity (I = 3.6 - 237 mW/cm^2) and exposure time (t = 10 - 1000 ms) are varied depending upon the sample and strength of the PA resonance. Typical peak atom loss due to PA is 10-50% over the baseline (same exposure time, but with no PA laser). Higher intensities generally produce larger loss signals, with the caveat that they also bring higher sample temperatures due to off-resonant scattering. As long as intensities high enough to produce significant cloud deformation are avoided, measurements of only the resonance center frequency f_ν (and thus binding energy E_ν) can tolerate such heating. However, measurements of resonance strengths themselves, as will be described in the next chapter, require more attention to the PA beam's effects on the sample. In this chapter, we are only concerned with E_ν.

For all three isotopes studied, we covered a range of detunings Δ from about -7

to $-320\,\mathrm{GHz}$, corresponding to vibrational quantum numbers $\nu \sim 75$ - 145. The PA excitation of colliding ground-state atoms to the molecular potential described by eq. 4.4 is strongly suppressed due to a node in the ground-state wave function at detunings of around $-55\,\mathrm{GHz}$ and $-100\,\mathrm{GHz}$ for ^{84}Sr and ^{87}Sr atoms respectively. This is the reason for the lack of data in the immediate vicinity of those detunings.

After exposing the PA beam, the PA and dipole trap lasers are immediately extinguished. This releases the atoms from the trap, and destructive resonant absorption imaging (also using the 461nm transition) is subsequently performed after a predetermined time-of-flight. Fits of the resulting atom cloud absorption image quantify the atom number and their temperature [78].

The PA spectroscopic widths Γ we observed were typically 60 - 150 MHz. The lower limit is consistent with an expected molecular linewidth of $2 \times \gamma_{atomic} = 60\,\mathrm{MHz}$. The Katori group observed broadening in ^{88}Sr for detunings more negative than $\Delta \sim -400\,\mathrm{GHz}$, and tentatively linked it to predissociation [130]. The Takahashi group observed a similar effect in PA studies of ^{174}Yb, again attributing it to predissociation from the $^{1}\Sigma_u^+$ state to triplet molecular states [113]. We do not observe a broadening trend in any of the isotopes studied, over the $\Delta \leq 320\,\mathrm{GHz}$ range we probe. The three furthest-detuned ^{87}Sr data points (see table 4.5) had widths $\sim 220\,\mathrm{MHz}$, but the data are sparse and insufficient to draw meaningful conclusions. Future studies incorporating data in the $\Delta \leq -400\,\mathrm{GHz}$ range would be valuable for making more conclusive statements about this effect, as would a tighter frequency-locking scheme that could allow resolving of the ^{87}Sr hyperfine states.

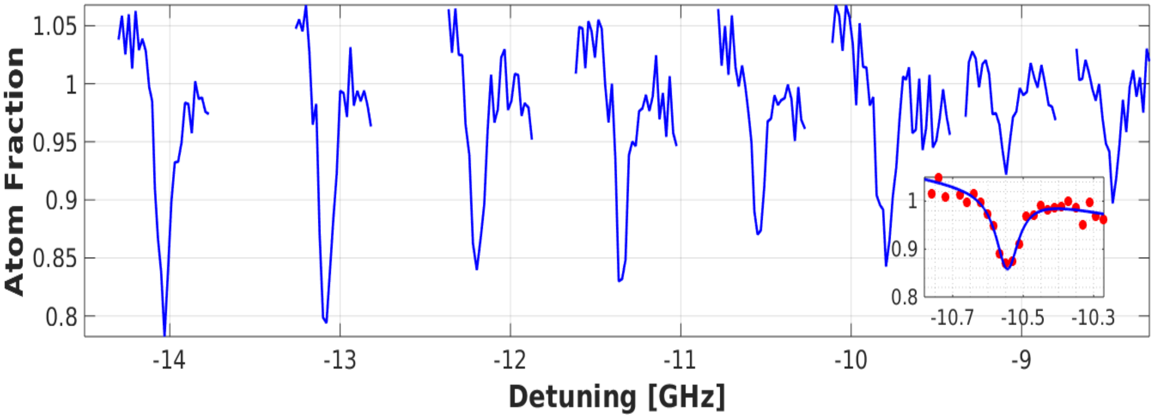

Figure 4.6: Representative atom loss spectra for excitation to molecular states on the $^1\Sigma_u^+$ $5s^2\,{}^1\mathrm{S}_0$ - $5s5p\,{}^1\mathrm{P}_1$ potential in ^{87}Sr. Background atom number is normalized to one. PA laser exposure times and intensities are adjusted to give comparable atom loss for all spectra, so line intensity does not reflect the PA-collision-event rate constant β_ν (eg. 5.7). Exposure times and intensities for these data vary from 75 - 200ms and 3.6 - 11.5 mW/cm^2 respectively. Inset is a representative fit to a Lorentzian.

4.4.1 Binding Energies

Here, I present our measurements of binding energies E_ν, as well as the results of fitting the data to eq. 4.7. At the time of writing, these present the first reported measurements of PA resonances using the 461 nm $^1\mathrm{S}_0$ - $^1\mathrm{P}_1$ transition in ^{87}Sr and ^{84}Sr. The Killian lab (among others) has performed such measurements on ^{88}Sr and ^{86}Sr with this transition in the past, and we measured the latter isotope again as a double-check and for uncertainty estimation [81] [85].

Fitting the data to eq. 4.7 provided a mentorship opportunity, and a Rice undergraduate student (P. Lunia) performed the fitting in Python. Note that for fermionic ^{87}Sr, the sample population was approximately equally distributed among the 10 available m_F nuclear spin states as a natural outcome of trapping in the red ($^1\mathrm{S}_0$ - $^3\mathrm{P}_1$) MOT [31]. Moreover, the ~ 60 MHz hyperfine splitting between the $F \in \{\frac{7}{2}, \frac{9}{2}, \frac{11}{2}\}$

states is sufficiently small that we do not resolve it [124]. Reducing the optical power to mitigate that broadening mechanism was not enough to resolve the hyperfine structure as frequency jitter in the laser-servo loop is on the order of the splitting.

ν	E_ν [GHz]	σ [GHz]	$obs. - fit.$ [GHz]
76	7.31	0.03	0.03
77	7.91	0.03	0.03
78	8.52	0.03	0.00
79	9.21	0.03	0.00
80	9.91	0.03	-0.04
81	10.67	0.03	-0.05
82	11.52	0.03	-0.03
83	12.42	0.03	-0.01
86	15.40	0.03	-0.02
87	16.53	0.03	-0.01
89	18.88	0.03	-0.10
91	21.68	0.03	-0.03
93	24.73	0.03	-0.04
94	26.39	0.03	-0.04
95	28.10	0.03	-0.08
99	36.13	0.03	-0.04
100	38.38	0.02	-0.06
130	187.83	0.03	0.03
131	196.71	0.03	0.02
132	205.98	0.03	0.03
133	215.73	0.07	0.18

Table 4.3: ^{84}Sr measured binding energies (E_ν), experimental uncertainties (σ), and residuals ($obs. - fit.$).

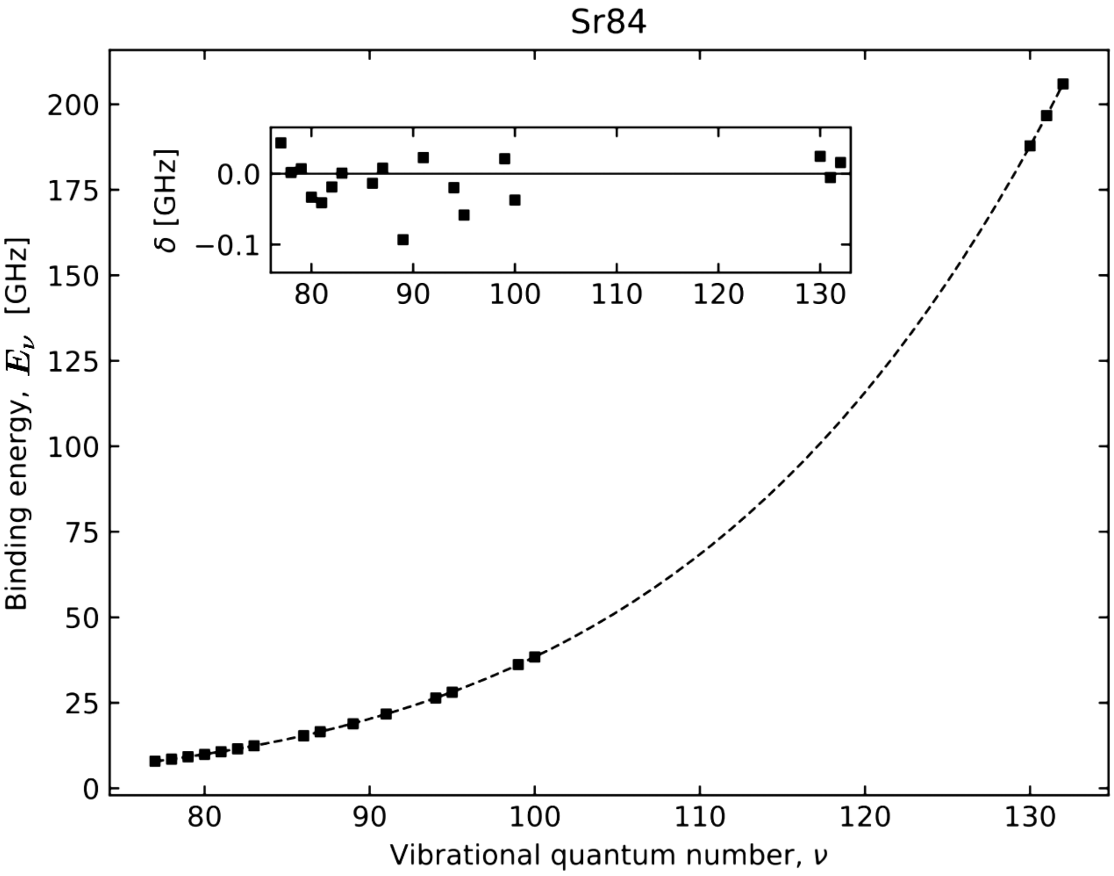

Figure 4.7: Fit (dashed line) to eq. 4.7 of the binding energies of states on the $^1\Sigma_u^+$ $5s^2\,^1S_0$ - $5s5p\,^1P_1$ molecular potential for ^{84}Sr as a function of vibrational quantum number ν. The inset plots the difference (δ) between observed and fit values using parameters from table 4.6.

ν	E_ν [GHz]	σ [GHz]	$obs. - fit.$ [GHz]
77	7.83	0.02	0.08
78	8.46	0.02	0.09
82	11.31	0.03	-0.01
83	12.21	0.02	0.05
88	17.35	0.02	0.06
89	18.55	0.02	0.04
94	25.73	0.02	0.02
95	27.42	0.02	0.02
100	37.32	0.03	0.02
105	50.04	0.03	0.03
109	62.58	0.03	-0.03
113	77.74	0.02	-0.02
118	100.83	0.03	-0.04
122	123.26	0.03	0.01
127	156.96	0.03	0.06
128	164.46	0.02	-0.02
131	189.01	0.03	-0.03
134	216.54	0.03	-0.05
136	236.80	0.03	0.04

Table 4.4: ^{86}Sr measured binding energies (E_ν), experimental uncertainties (σ), and residuals ($obs. - fit.$).

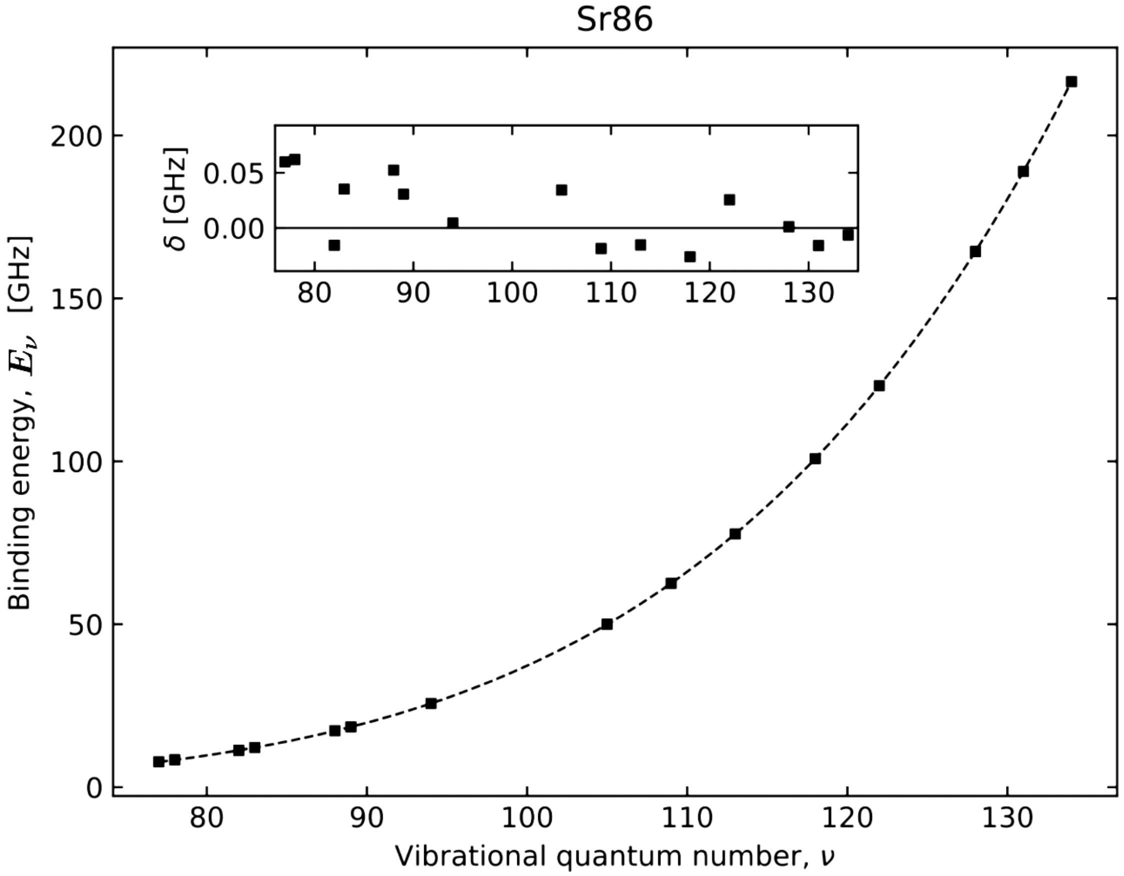

Figure 4.8: Fit (dashed line) to eq. 4.7 of the binding energies of states on the ${}^1\Sigma_u^+$ $5s^2\,{}^1\mathrm{S}_0$ - $5s5p\,{}^1\mathrm{P}_1$ molecular potential for ^{86}Sr as a function of vibrational quantum number ν. The inset plots the difference (δ) between observed and fit values using parameters from table 4.6.

ν	E_ν [GHz]	σ [GHz]	$obs. - fit.$ [GHz]
76	6.67	0.11	0.11
77	7.23	0.03	0.13
78	7.79	0.03	0.11
79	8.37	0.03	0.08
80	9.05	0.03	0.11
81	9.69	0.03	0.04
82	10.42	0.11	0.04
83	11.26	0.03	0.06
84	12.09	0.03	0.06
85	12.99	0.03	0.06
86	13.95	0.05	0.06
87	14.95	0.03	0.06
88	16.02	0.03	0.07
93	22.32	0.03	0.02
95	25.36	0.03	-0.02
99	32.57	0.05	-0.01
100	34.55	0.04	-0.06
105	46.43	0.04	-0.07
108	55.05	0.04	-0.08
109	58.20	0.03	-0.09
110	61.49	0.06	-0.12
142	288.18	0.03	-0.01
143	300.67	0.03	0.01
144	313.57	0.03	-0.01

Table 4.5: ^{87}Sr measured binding energies (E_ν), experimental uncertainties (σ), and residuals ($obs. - fit.$).

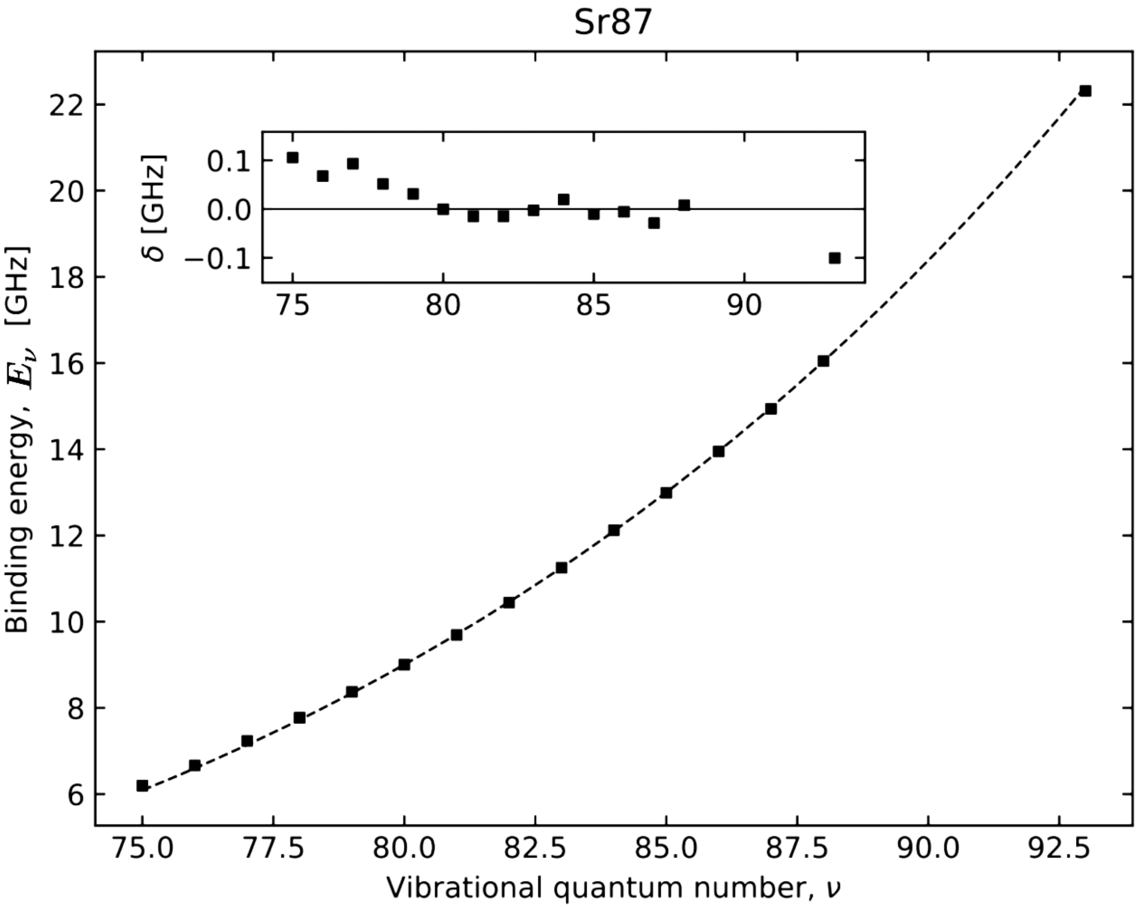

Figure 4.9: Fit (dashed line) to eq. 4.7 of the binding energies of states on the ${}^1\Sigma_u^+$ $5s^2\,{}^1\mathrm{S}_0$ - $5s5p\,{}^1\mathrm{P}_1$ molecular potential for ^{87}Sr as a function of vibrational quantum number ν. The inset plots the difference (δ) between observed and fit values using parameters from table 4.6.

4.5 Uncertainties and Excited-State Lifetime

The largest source of uncertainty in our measurement of binding energies stems from the calibration and locking scheme controlling the frequency of the PA laser (see fig. 4.4). As described earlier in this chapter, the laser's output is sampled and sent to a wavemeter with a programmable PID setpoint. The meter then outputs a correction signal that is fed back to laser's diffraction grating, providing frequency stabilization.

The absolute calibration of the device introduces a frequency uncertainty of about ± 30 MHz. There is also shot-to-shot variation in the laser's frequency from mechanisms internal to the laser's operation and or PID control voltage jitter that the loop is unable to mediate. This jitter dominates other possible broadening mechanisms such as 1064 nm and 461 nm ac Stark shifts, as well as the thermal energy distribution of the atomic sample. The jitter is approximately similar in scale to the calibration uncertainty. Quantifying the spectral width (e.g. with an optical cavity), and a more sophisticated feedback system, could reduce these effects. However, the current setup is adequate for the studies conducted in this thesis. Experimental uncertainties (σ) in tables 4.3, 4.4, and 4.5 are the sum of the statistical uncertainty from the fit to each resonance's center frequency (f_ν), and the absolute uncertainty from calibration of the wavemeter.

We perform a combined fit of all data to eq. 4.7 using a common value of C_3 as a fit parameter, and independent values of ν_D for each isotope. The quantum numbers ν assigned to each level are shifted to obtain $0 < \nu_D < 1$. Table 4.6 shows the resulting fit parameters, including the value of C_3. The statistical uncertainties in the energies from this procedure are very small, but the fit residuals for all three isotopes show a systematic trend corresponding to ~ 100 MHz variation over a change of ~ 100 GHz in binding energy. This trend may indicate systematic wavemeter error, variation in molecular-state ac Stark shifts from the optical dipole trap laser fields, or the influence of additional terms in the molecular potential not accounted for by the Leroy-Bernstein formula [25].

These measurements can also be used to calculate the $^1\mathrm{P}_1$ excited-state lifetime $\tau = 1/\gamma_{atomic}$ via eq. 4.5. Our data indicate a value of $\tau = 5.20$ ns. Adding an additional fit parameter to eq. 4.7 in the form of a binding energy offset removes the systematic trends in the residuals and increases τ by 0.02 ns or 0.4%, which we take as our uncertainty.

Isotope	^{87}Sr	^{86}Sr	^{84}Sr
ν_D	0.87 ± 0.02	0.20 ± 0.02	0.87 ± 0.02
C_3 (cm^{-1}Å^6)	605 ± 3		

Table 4.6: Parameters from fitting PA binding energy data in ^{84}Sr, ^{86}Sr, and ^{87}Sr to eq. 4.7.

There are fewer published works studying the ^{1}P$_1$ state lifetime compared to those of the narrow intercombination ^{3}P$_j$ triplet series, and table 4.7 compares the three most recent prior results at the time of writing to that determined in this work. The value of τ determined here differs by 1% from the most accurate reported measurement of $\tau = 5.263 \pm 0.004\,\text{ns}$, performed with photoassociation in an optical lattice [130], and is in closer agreement with a more recent value of $\tau = 5.234 \pm 0.008\,\text{ns}$ determined via ac Stark shifts of Sr levels [45] . Note that the former reference used a significantly higher "typical" PA beam intensity (10,000 mW/cm^2) than our work (3.6 - 237 mW/cm^2).

Measurement Method	**Isotope**	**τ (ns)**	**Reference**
PA Spectroscopy ($\lambda = 689\,\text{nm}$ MOT)	^{88}Sr	5.22 ± 0.03	[85]
PA Spectroscopy ($\lambda = 810\,\text{nm}$ 1D Lattice)	^{88}Sr	5.263 ± 0.004	[130]
ac Stark Shifts ($\lambda = 689\,\text{nm}$ 1D Lattice)	^{87}Sr	5.234 ± 0.008	[45]
PA Spectroscopy ($\lambda = 1064\,\text{nm}$ ODT)	^{84}Sr, ^{86}Sr, and ^{87}Sr	5.20 ± 0.02	This work

Table 4.7: Comparison of atomic lifetimes (τ) for the ^{1}P$_1$ state from various groups. From the top row down, the trapping method for each result is a 689 nm magneto-optical trap, a “magic” wavelength lattice that induces commensurate light shifts in the ground and excited-states, a “tune-out” lattice that zeros the light shift in the ground-state, and the crossed optical dipole trap described in another chapter of this thesis.

Chapter 5

PA Lineshape and Rate Constant

In a previous chapter, we used a simple Lorentzian (eq. 4.6) to fit photoassociative atom loss spectra. We could then determine molecular binding energies E_ν for each resonance, identified by their vibrational quantum numbers ν. This chapter will develop a more detailed theoretical description of the PA loss lineshape, and present results extracted from the model. By measuring the loss spectra of selected PA resonances, each at various exposure times, this more detailed description allows us to extract values of the two-body collision rate constant β_ν. The rate constant is particularly interesting because it encapsulates much of the physics of the PA process beyond the sequence of binding energies. For example, it determines resonance amplitudes (for fixed atom density and laser intensity), and can be related to the ground-state wave function as a sensitive measure of collision length and energy scales.

5.1 Photoassociative Loss

A description of atoms being lost from the trap due to photoassociation begins with the time-evolution of the local atomic density $n(t)$ via

$$\dot{n} = -\beta_\nu n^2 - \gamma n \tag{5.1}$$

where γ is the one-body loss rate due to off-resonant scatter plus background gas collisions (eq. 6.1). Our goal is to construct an expression for the number of atoms in the trap as a function of PA laser exposure time t and frequency f. The rates β_ν and γ both depend on the laser's frequency and intensity I. We make the simplifying assumption that the sample temperature is independent of the laser's frequency, and therefore does not change throughout the spectra for fixed ν, I, and t. This assumption is true to within 20%, with heating and atomic cloud deformation being more difficult to avoid for resonances closer to the atomic asymptotic ($\Delta \lesssim 20\,\mathrm{GHz}$). Such effects influence the uncertainty in our measurements, as will be described in a latter section of this chapter. There are theoretical models of the loss that do account for temperature changes, as well as the initial thermal distribution of the colliding atoms [57]. However, these are not warranted given the scale of other uncertainties in our measurements.

Assuming a constant sample temperature, the number of atoms in the trap as a function of the PA exposure time can be found by integrating eq. 5.1 over volume to obtain

$$\dot{N} = -\beta(I, f) N^2 \frac{V_2}{V_1^2} - \Gamma_1 N \tag{5.2}$$

Collisions between successively higher numbers of partners occur more frequently in higher density regions. This effect can be conveniently expressed in terms of effective ith body volumes V_i depending on the number of collision partners (eq. 5.5). V_1

and V_2 in eq. 5.2 are the one and two-body effective volumes respectively. Note that $V_2/V_1^2 = 1/(2\sqrt{2}V_1)$, and $n_0 = N_0/V_1$. Solving eq. 5.2, the resulting number evolution is

$$N(t) = \frac{N_0 \mathrm{e}^{-\gamma t}}{1 + \frac{n_0 \beta_\nu}{2\sqrt{2}\gamma}(1 - \mathrm{e}^{-\gamma t})} \tag{5.3}$$

where $N_0 = N(0)$ and $n_0 = n(0)$ are the atom number and density at the beginning of the PA interaction time respectively.

5.1.1 Three Body Rate Estimation

Loss processes involving higher numbers of constituents, e.g. three-body collisions, require higher densities than those for two-body loss [120]. To estimate the contribution of such processes to the atom loss signal under typical conditions in these experiments, we consider a possible three-body term for eq. 5.1. The rate G has been introduced to provide a more convenient form for comparison to other processes depending on density to the first power.

$$\dot{n} = -\left(\frac{1}{6}\right) \mathrm{k}_3 n^3 = -\mathrm{G}n \tag{5.4}$$

where k_3 is the three-body collision rate. Because this k_3 rate is conventionally defined for non-condensed bosonic collision partners in a single internal sate, it subsumes a factor of $= 3!$ from the three-body correlation function $g^{(3)}$ reflecting bosonic bunching. The 1/6 factor in eq. 5.4 reflects our treatment of collisions in ^{87}Sr fermionic samples, equally populated among the ten spin states, as if occurring in a classical non-interacing gas with $g^{(3)} = 1$. The ten available spin components form a large enough set of distinct internal states to neglect Pauli blocking.

At the time of writing, data are available for k_3 in ^{86}Sr ($\sim 10^{-24}\,\mathrm{m}^6/\mathrm{s}$) [109] and ^{84}Sr ($\sim 3\times10^{-27}\,\mathrm{m}^6/\mathrm{s}$) [127]. To our knowledge, there has yet to be any measurement of k_3 in ^{87}Sr, however, its rate is expected to be comparable to that in ^{84}Sr due to the similarity of their scattering lengths (approximately 96 and 123 Bohr radii respectively).

As alluded to in deriving eq. 5.3, more frequent collisions between successively higher numbers of partners in higher density regions can be expressed via effective volumes V_{i} depending on the number of collision partners (i). For atoms of temperature T

$$V_{\mathrm{i}} = \frac{1}{n^i(0)} \int n^i(r) d^3r = \frac{1}{f_x f_y f_z} \left(\frac{k_B T}{\mathrm{i} \cdot 2\pi m} \right)^{3/2} \tag{5.5}$$

Where f_j is the oscillation frequency of atoms displaced in the optical trap's jth axis, k_B is the Boltzman constant, and m is the atomic mass. This definition assumes that the optical dipole trap potential ($V = \frac{1}{2} m \sum_j \omega_j^2 x_j^2$) is an infinite harmonic well in three dimensions (x_j) with angular oscillation frequencies ω_j, and that the atomic density distribution is Gaussian ($n = n(0) \exp(\frac{-V}{k_B T})$).

Simplifying eq. 5.4 and grouping factors together, we find:

$$\mathrm{G} = \mathrm{k}_3 \frac{n_0^2 V_3}{6 V_1} \tag{5.6}$$

For the $n_0 \sim 1.5 \times 10^{13}\,\mathrm{cm}^{-3}$ densities used in the experiments described in this thesis, and assuming k_3 for ^{87}Sr is $3 \times 10^{-27}\,\mathrm{m}^6/\mathrm{s}$, $G \approx 0.40\,\mathrm{s}^{-1}$. Therefore G can safely be neglected in comparison to the two-body process we wish to study, as well as the one-body rate from off-resonant scattering (fig. 6.2).

5.2 Rate Constant and Resonance Amplitudes

Close to resonance with a transition to the excited molecular state of vibration quantum number ν and center frequency f_ν, the two-body loss parameter β_ν is described with a model that convolves the natural transition lineshape with a phenomenological

Lorentzian [85].

$$\beta_\nu = \frac{2K_\nu \gamma_{mol}}{\Gamma} \frac{1}{1 + 4(f - f_\nu)^2/\Gamma^2}, \tag{5.7}$$

Where $\gamma_{mol} = 2\gamma_{atomic}$ is the natural linewidth of the PA transition due to radiative decay of the molecular state, and Γ is the observed linewidth of the transition. The model maintains the integrated transition amplitude. K_ν is the resonant (peak) collision-event rate constant that would be observed in the absence of any broadening beyond the natural linewidth (i.e. if $\Gamma = \gamma_{mol}$). Thermal broadening due to the spread in initial atom energies is much smaller than γ_{mol}, and the laser intensity is low enough that saturation effects are negligible. Figure 5.1 shows a fit of typical atom loss spectra to eqs. 5.3 and 5.7 for different PA laser exposure times for ^{86}Sr.

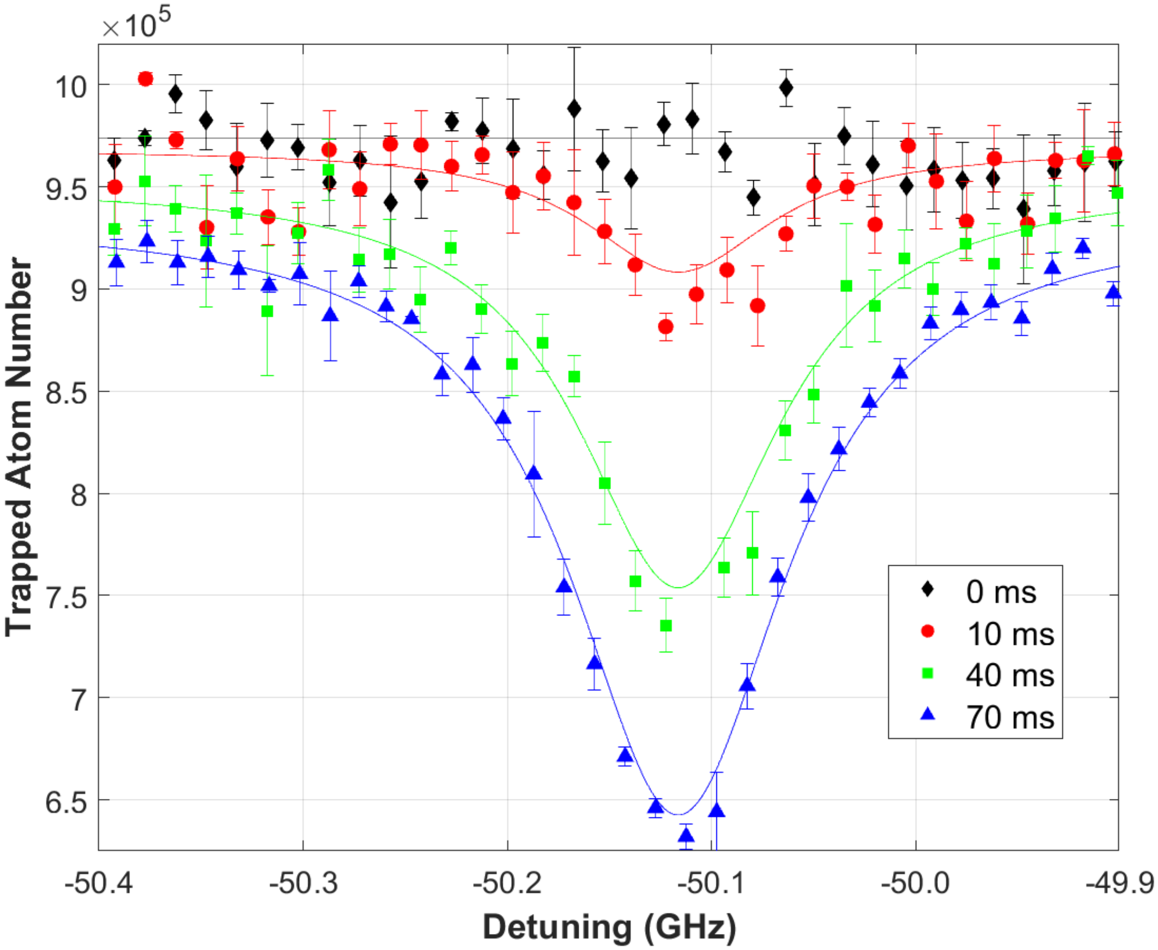

Figure 5.1: Atom loss spectra for PA to the $\nu = 105$ vibrational state on the excited molecular potential in ^{86}Sr. The PA laser exposure time for each trace is indicated in the legend. A combined fit of all data to eqs. 5.3 and 5.7 determines the intensity-normalized peak collision-event rate constant $K_{\nu=105}/I = 2.8 \times 10^{13}\,\mathrm{cm}^5/(\mathrm{s{\cdot}mW})$ for $I = 3.6\,\mathrm{mW/cm}^2$. The initial density was $n_0 = 1.3 \times 10^{13}\,\mathrm{cm}^{-3}$.

Measuring spectroscopic data for frequencies approximately one linewidth Γ on either side of a PA resonance not only helps determine the resonant center frequency, but also allows differentiation between two-body and one-body (primarily determined by off-resonant scattering) loss processes. Possessing this background data in the "wings" of the PA lineshape therefore enables each exposure time spectra to generate another measurement of β_ν. Each sweep of frequencies through the PA resonance at a fixed exposure time is accompanied by interleaved measurements of the trapped atom number immediately prior to exposing the PA beam (i.e. zero exposure time). These zero-time scans determine the initial sample density n_0, and the order in which they happen allows us to account for drifts in the number of trapped atoms between sweeps through resonance.

5.2.1 Computational Side-note: Fitting

The initial approach to fitting the combined eqs. 5.3 and 5.7 to PA spectroscopic data used *Matlab's* `lsqcurvefit` function. Although it was possible to manually fine-tune initial guesses for the fit parameters $(K_\nu, \Gamma, \gamma, f_\nu)$, the function struggled with this task, often settling on parameter values wildly far from approximate manual guesses, and the data. Bounding the parameters to physically sensible values (e.g. $f_\nu \geq 0$) marginally improved the fit success rate, loosely defined as the fit returning parameter values comparable to the best values when tuned by eye. However, the largest gain in success rate came from switching to minimizing the root-mean-square difference between the fit iterations and data with the `fminsearch` minimization routine. We did not conduct an exhaustive analysis of why this method succeeded where the previous was sub-optimal. However, the working hypothesis is that the fit objective functions are not smooth, and the many local minima were causing the gradient-based `lsqcurvefit` routine to converge at these places rather than a more appropriate parameter set. The `fminsearch` by contrast, is a direct method that computes function values at various points around the current one rather than derivatives.

5.3 Relationships to Fundamental Quantities

The PA loss description developed in the preceding section provides an understanding of how the observed resonance amplitudes, and their associated rate constants, change with laser intensity and detuning from the atomic asymptote ($\Delta_\nu < 0$). It is also useful to relate these measurements to other fundamental quantities governing the collision and excitation process. One such quantity is the wave function of the colliding ground-state atoms $\psi_g(R)$, dependent on the internuclear separation R. Such a relationship, and the approximations necessary for its calculation, will be outlined here. Afterwards, the observed spectroscopic data will be compared to rate constant predictions based on numerically solving for $\psi_g(R)$.

When studying the spectroscopy of molecular vibrational transitions, the Franck-Condon factor (FCF) is a common tool for quantifying the probability of a transition's occurrence. The tool can also be applied to transitions between bound states. However, the factors $F^\nu_{eg}(E, \Delta_\nu)$ in this thesis correspond to the data in that they are restricted to transitions from a free (continuum) ground-state with wave function $\psi_g(R, E)$ and initial collision energy E, to a bound molecular excited-state with wave function $\psi^\nu_e(R)$, vibrational quantum number ν, and detuning Δ_ν. For both the FCF and excited wave function, the superscript ν is a label, and does not indicate exponentiation. In using the FCF, nuclear motion is approximated as negligibly slow over the transition timescale. This amounts to a decoupling of the vibrational and electronic degrees of freedom. The free-to-bound FCF per unit energy is related to the overlap of the wave functions via

$$F^\nu_{eg}(E, \Delta_\nu) = \left| \int_0^\infty \psi^\nu_e(R) \psi_g(R, E) dR \right|^2 \tag{5.8}$$

where $\psi_g(R, E)$ is energy-normalized, and $\psi^\nu_e(R)$ is normalized to unity.

Recall from the previous description of the spectroscopic lineshape (eq. 5.7), that K_ν/I is an intensity-normalized, resonant, collision-event rate constant for excitation by a laser with negligible linewidth. The rate has conventional units of $\mathrm{cm}^5/(\mathrm{mW\,s})$, and is proportional to the FCF. For unsaturated (loss $\ll 100\%$) transitions at large detunings, Ciuryło develops the theoretical scaling for this proportionality [23].

Up to this point, calculations of the FCF still require knowledge of the ground and excited-state wave functions. It would be advantageous to relate the FCF to only one wave function. In particular, because the ground-state strontium potential is well-studied, numerically calculating the ground-state wave function is more straightforward than for the excited-state. At long range and ultracold temperatures, the ground potential can be approximated by a form of eq. 4.2 that keeps additional higher-order multipole expansion terms

$$V_g(R) = -\frac{C_6}{R^6} - \frac{C_8}{R^8} - \frac{C_{10}}{R^{10}} \tag{5.9}$$

Fourier-transform spectroscopy experiments in a Sr heat-pipe have accurately determined recommended dispersion coefficient values of $C_6 = 1.525 \times 10^7\,\mathrm{cm}^{-1}\mathrm{\AA}^6$, $C_8 = 5.159 \times 10^8 \mathrm{cm}^{-1}\mathrm{\AA}^8$, and $C_{10} = 1.91 \times 10^{10}\,\mathrm{cm}^{-1}\mathrm{\AA}^{10}$ [106].

To relate the FCF to $\psi_g(R, E)$, we take advantage of the reflection approximation [14]. For cold, binary collisions between two ground-state atoms at long range, excitation to a single excited-state (single-channel) bound to an attractive potential, the FCF is dominated by the amplitude of the ground-state wave function near the position of the last lobe in the excited-state wave function (see fig. 6b of [57]). Thus, the approximation stems from the collision energies involved, and the shape of the wave functions over a particular set of internuclear separations, when confined to $\sim 1/R^3$ and $\sim 1/R^6$ potentials.

For a particular isotope, the measured PA resonance detunings define a set of

Condon radii via

$$h\Delta_\nu = V_e(R_{C,\nu}) - D - V_g(R_{C,\nu}) \tag{5.10}$$

I.e. the Condon radii are the internuclear separations at which the photon energy (via the Plank constant h) is resonant with the difference in molecular potentials. R_C is a classical separation at which the transition can be described as occurring. The van der Waals length R_{vdW} is a convenient delineation between short and long range regimes.

$$R_{vdW} = \frac{1}{2}\left(\frac{2\mu C_6}{\hbar^2}\right)^{1/4} \tag{5.11}$$

For ^{87}Sr, $R_{vdW} \sim 75\,a_0$, which is smaller than the Condon radii of the resonances we measure (approximately $80 - 240$ Bohr radii). This fact, and the approximately 2μK initial collision energies of the ground-state atoms, put our samples within the region of validity for the reflection approximation. Boisseau describes quantitative examples of separations too small, or too large, where the approximation breaks down [14].

Under these conditions, the FCF reflects, in the colloquial sense of “is a proxy for”, the ground-state wave function, and vice versa. Using the reflection approximation, the FCF can be related to the energy-normalized ground-state wave function at the Condon point $\Psi_g(R_{C,\nu}, E)$, by

$$F^\nu_{eg}(E, \Delta_\nu) = \frac{\partial E_\nu}{\partial \nu}\frac{1}{d_c}|\Psi_g(R_{C,\nu}, E)|^2 \tag{5.12}$$

where $\partial E_\nu/\partial\nu$ is the spacing between adjacent vibrational levels in the excited-state at level ν, which can be found from the LeRoy Bernstein expression (eq. 4.7). The difference in slopes between the excited and ground potentials is given by

$$d_c = \left|\frac{d}{dr}\left[V_e(R) - V_g(R)\right]\right|_{R=R_{C,\nu}} \tag{5.13}$$

The technique is powerful because, when used in a parameter regime that allows the appropriate approximations to be made, the amplitudes of vibrational spectra can be explained without detailed knowledge of the excited-state wave function or electronic properties such as dipole matrix elements.

To compare measured rate constant data against the model in eq. 5.12, we calculated ground-state wavefunctions using $V_g(R)$ from eq. 5.9 for a collision energy of $2\,\mu$K by numerically integrating the Schrödinger equation via the Numerov method [53]. This was performed by the Rice student W. Huie, and more information can be found in his Bachelors thesis on the Killian group website [50]. $V_e(R)$ was calculated as in eq. 4.4.

The FCF, and thus the measured resonance amplitude, is also dependent on the quantum statistics of the colliding atoms. In particular, the signal is proportional to the probability of finding two particles at a distance equal to $R_{C,\nu}$. This probability is determined by the two-particle pair correlation function $g^{(2)}(R)$ [124]. We calculate an approximate $g^{(2)}(R)$, by finding the value for two particles at the same location ($R = 0$). This approximation is valid so long as $R_{C,\nu}$ is small compared to the thermal deBroglie length

$$\lambda_{dB} = \frac{h}{\sqrt{2\pi m k_B T}} \tag{5.14}$$

For the temperatures probed in this work, the de Broglie length is about a factor of twenty larger than the Condon radii, and we are justified in calculating $g_f^{(2)}(0) = 0.9$ for ^{87}Sr samples with ten equally populated m_F states. Therefore, predicted K_ν/I values for ^{87}Sr are further reduced with respect to those that would be expected for bosonic samples by the ratio of the pair correlation functions $g_f^{(2)}/g_b^{(2)}$, where $g_b^{(2)} = 2$ reflects bunching in thermal bosonic samples.

We are now in a position to compare spectroscopic rate constant data with predictions based on eq. 5.12 and its constituent factors as described in the preceding paragraphs. Figure 5.2 shows the measured values of K_ν/I, extracted from fits to eqs. refeq:number and 5.7, and theoretically expected values. A common scaling factor is applied to the theoretical predictions for all isotopes to account for the proportionality between K_ν/I and the Franck-Condon factors. The PA laser intensity is taken as the peak value at the center of the Gaussian beam's transverse profile.

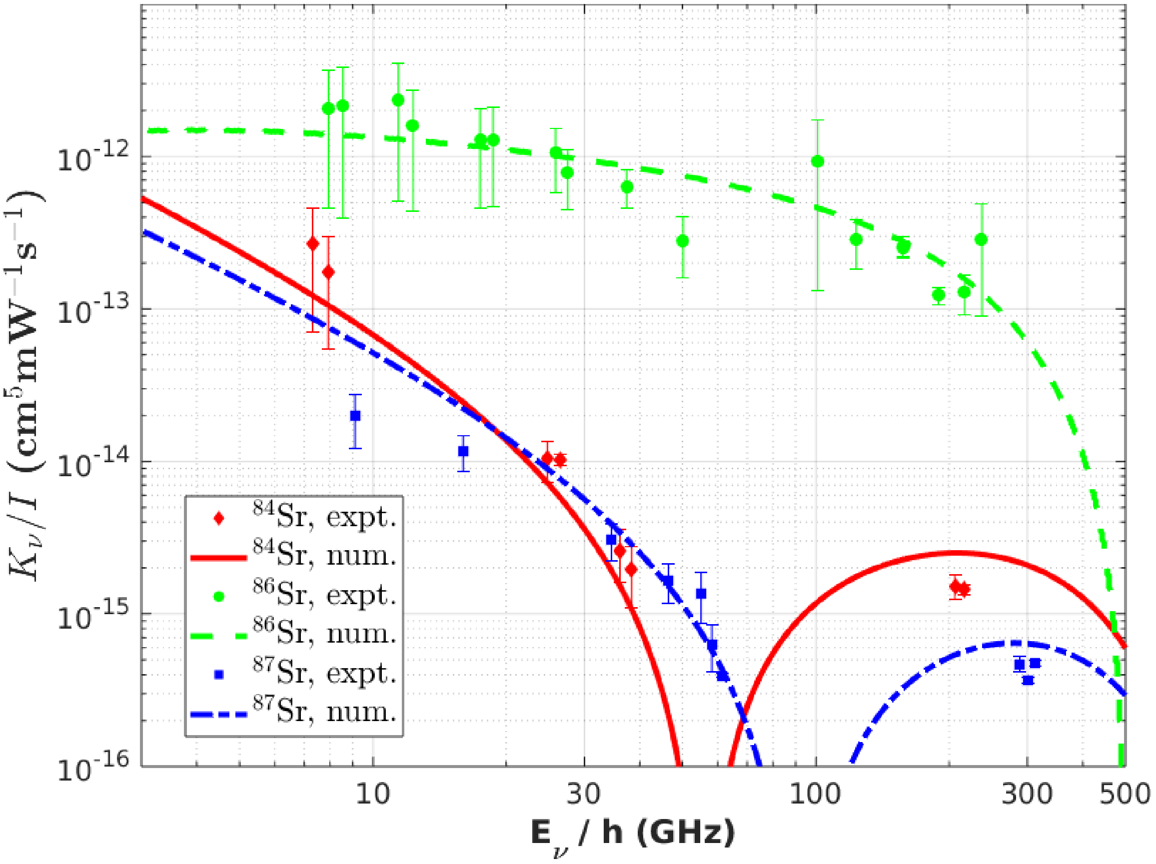

Figure 5.2: Comparison of experimental data and theoretical predictions for the intensity-normalized resonant collision-event rate constant K_ν/I. Solid lines are predictions based on Franck-Condon factors derived from numerically calculated ground-state wave functions (eq. 5.12). Solid points are measured values of K_ν/I, extracted from fits to eqs. 5.3 and 5.7

To our knowledge, publication of these data constitute the first reported PA resonance frequencies and K_ν/I values for excitation to bound states on any potential in ^{87}Sr, and to this particular potential in ^{84}Sr [49]. Our most recent measurements for ^{86}Sr agree within a factor of two with previously reported values, which is reasonable given systematic uncertainties [81]. Note that the rate coefficients go to zero when the Condon radius for the transition is near a node of the ground-state wave function. For ^{87}Sr and ^{84}Sr, the node interrogated by measurements reported here corresponds to internuclear spacing equal to the s-wave scattering lengths, $a_{84} = 123\,a_0$ or $a_{87} = 96\,a_0$ [72], where a_0 is the Bohr radius. For ^{86}Sr, $a_{86} = 823\,a_0$ is a larger lengthscale than probed here, and the node corresponding to $\Delta = -500\,\mathrm{GHz}$ is the second pre-asymptotic node [81].

5.3.1 Uncertainties

All fit parameters are well determined, but systematic uncertainty in laser intensity, atom density, and sample temperature lead to an uncertainty of about a factor of 3 in the measured values of K_ν/I. Pernicious experimental contributors to the uncertainty in these quantities are, for example, uncertainty in how well aligned the PA and ODT lasers are to the atomic sample. Physical access to the atom-laser overlap region is precluded by the vacuum apparatus. While is it possible to measure the beam on a test setup with appropriate distances, imperfections in optical elements and some ambiguity in the beam alignment remain. Using an atom loss resonance as a metric for peaking up the beam's alignment is a valuable, but not foolproof, method of ensuring that the exact center of the Gaussian beam is overlapped with the sample. Misalignment of the PA laser from the atoms would reduce the intensity compared to the peak value we quote. Misalignment of the ODT beams can cause the atoms to experience an anharmonic trapping potential, leading to uncertainties in the trapping volume and thus the atomic density.

Another potential source of uncertainty is the distorting effect of the PA beam on the atomic sample. This tends to asymmetrically elongate the cloud, pushing atoms along the beam's propagation axis as in fig. 5.3. Away from resonance with a PA transition, this effect is most pronounced at the smallest detunings measured (see eq. 6.2). This does not appear to have a substantial impact on the quality of the fits determining the atom number and temperature in that axis, but unless otherwise indicated, atomic sample temperatures quoted in this thesis are those obtained from fits to the vertical cloud axis, as this is affected less by the distortions. Our PA atom-loss rate model assumes a constant temperature of the sample over the range of excitation laser frequencies. While we made every effort to minimize sample heating throughout the spectra, temperature fluctuations of up to 20% were a necessary consequence of the PA laser intensities necessary to to achieve a measurable signal.

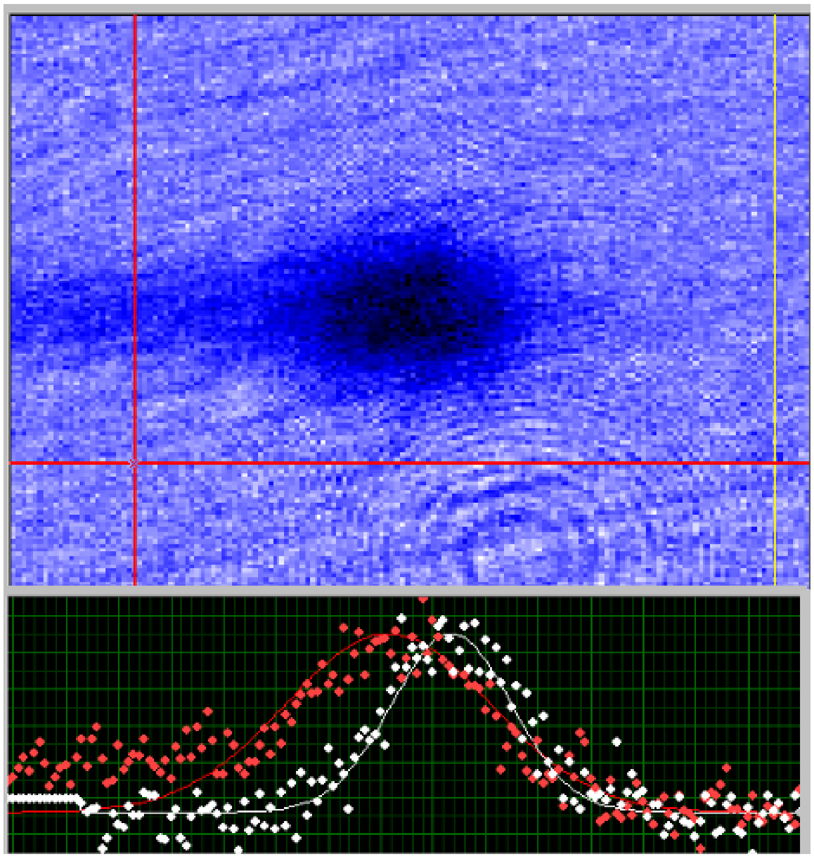

Figure 5.3: Asymmetric distortion in a sample of ^{87}Sr atoms with an approximate detuning of 20 GHz, about10 ms after being released from the ODT. The plotted data are Gaussian fits to one-dimensional cuts through each of the vertical and horizontal cloud axes containing the peak optical depth signal.

Lastly, the approximately 10 -1000 ms PA laser exposure times used were comparable to, or much longer than, than the motional timescale of the atoms in the trap given by

$$\frac{1}{\bar{f}} = \frac{1}{(f_x f_y f_z)^{1/3}} \approx 8\,\mathrm{ms} \tag{5.15}$$

If the size of the sample is not much less than the extent of the PA laser, this could introduce time dependent intensity fluctuations as the moving sample experiences non-peak beam intensities. We measure *in situ* sample sizes of approximately 150 μm (the smaller axis of the PA beam is 440 μm). While this effect could be most pronounced between shot-to-shot measurements at short exposure times, our 200 ms free evaporation equilibration time and averaging together of multiple frequency sweeps when collecting data make this uncertainty negligible in relation to those previously discussed.

Chapter 6

PA As a Tool

6.1 Introduction

In this chapter I discuss employing PA as a tool, particularly for experiments involving ^{87}Sr atoms confined to an optical lattice. A second goal of this work, after identifying PA resonances characterizing the physics behind their spectra, was to understand if the resonances could be used as a detection mechanism in experiments the lab plans to conduct in the future. The basic premise of the intended technique is to apply light resonant with a particular PA transition to atoms confined in an optical lattice. In doing this, the PA process introduces an atom loss channel for pairs occupying the same lattice site. Given the typical parameters of cold-atom experiments (densities, lattice depths, etc), the majority of sites will be occupied by zero, one, or two atoms. The latter "doublons" are our primary interest, and quantifying their dynamics can provide valuable information about the sample temperature and be used to probe quantum phase transitions [112].

The goal of this chapter is to compare simple calculations of the photoassociation rate, and other loss processes, to the data. From this comparison, a parameter set advantageous for implementing PA-based doublon detection in Sr will be determined, with a particular emphasis on ^{87}Sr. A metric for making this determination is the ratio of rates, for example, by checking whether the rate of PA-induced doublon loss is greater than other loss processes for typical conditions in an optical lattice. The PA rate must be the dominant loss mechanism for it to be a useful tool, otherwise quantifying the doublon number could not occur before other processes eroded the overall number of trapped atoms. Therefore, after studying the strengths and frequencies of the resonances, the next step to employing them as a detection mechanism is to quantify which resonances and experimental parameter regimes are necessary to achieve a favorable balance of PA to non-PA loss rates.

6.2 One-Body Rates

There are a few nontrivial reasons why trapped atoms in an ODT can be lost during spectroscopy experiments. The two-body (two Sr atom) PA process characterized by eqs. 5.2 and 5.7 is the one example. One-body processes also contribute to the overall loss signal. Quantifying these additional loss channels allows us to differentiate the PA signal of interest, and focus on the physics it contains. Higher-order n-body loss mechanisms exist, but become increasingly less likely for a given density, and will not be considered here.

Two one-body loss processes will be examined here. The first process is the off-resonant rate R of PA laser photons scattering from single atoms. The same occurs for ODT photons as well, but the detuning is sufficient large from the strongest (^{1}S$_0$ - ^{1}P$_1$) transition to make the rate negligible. In the case of exceedingly weakly trapped atoms, every scattering event leads to loss of the atom from the trap. For progressively stronger traps (deeper potential wells), the loss rate will be subsequently lower as only atoms with sufficient thermal plus photon recoil energy will be able to escape. For a sense of scale, a trap depth of $5\,\mu$K is about $100\,$kHz deep, and the photon recoil energy for a $\lambda \sim 461\,\mathrm{nm}$ photon is about $11\,\mathrm{kHz}$.

The second one-body loss rate γ_{bg} arises from collisions between Sr and background gas atoms in the vacuum chamber. Despite the ultra-high vacuum environment, there are residual non-Sr atoms inside the chamber due to outgassing or diffusion. When confining atoms in a trap with a depth that is constant over time (free evaporation) for a variable holding period, the sample stabilizes to a point where any heating is balanced by residual evaporation after a period of rapid initial atom loss and temperature decrease. This regime is typically indicated by a change in the slope of atom-loss (and temperature decrease) as the ODT hold time is increased. By measuring the slope after this point we are able to put an upper bound on γ_{bg}. For example, ^{84}Sr data (figure 6.1) in an ODT with about $1.9\,\mathrm{W}$ of power in each of the two beams indicates $\gamma_{bg} = 1/\tau_{bg} = 0.15\,\mathrm{s}^{-1}$, or $\tau_{bg} = 6.67\mathrm{s}$. In general, this estimated bound on γ_{bg} will depend on the trap depth and geometry, as well as the sample species and density.

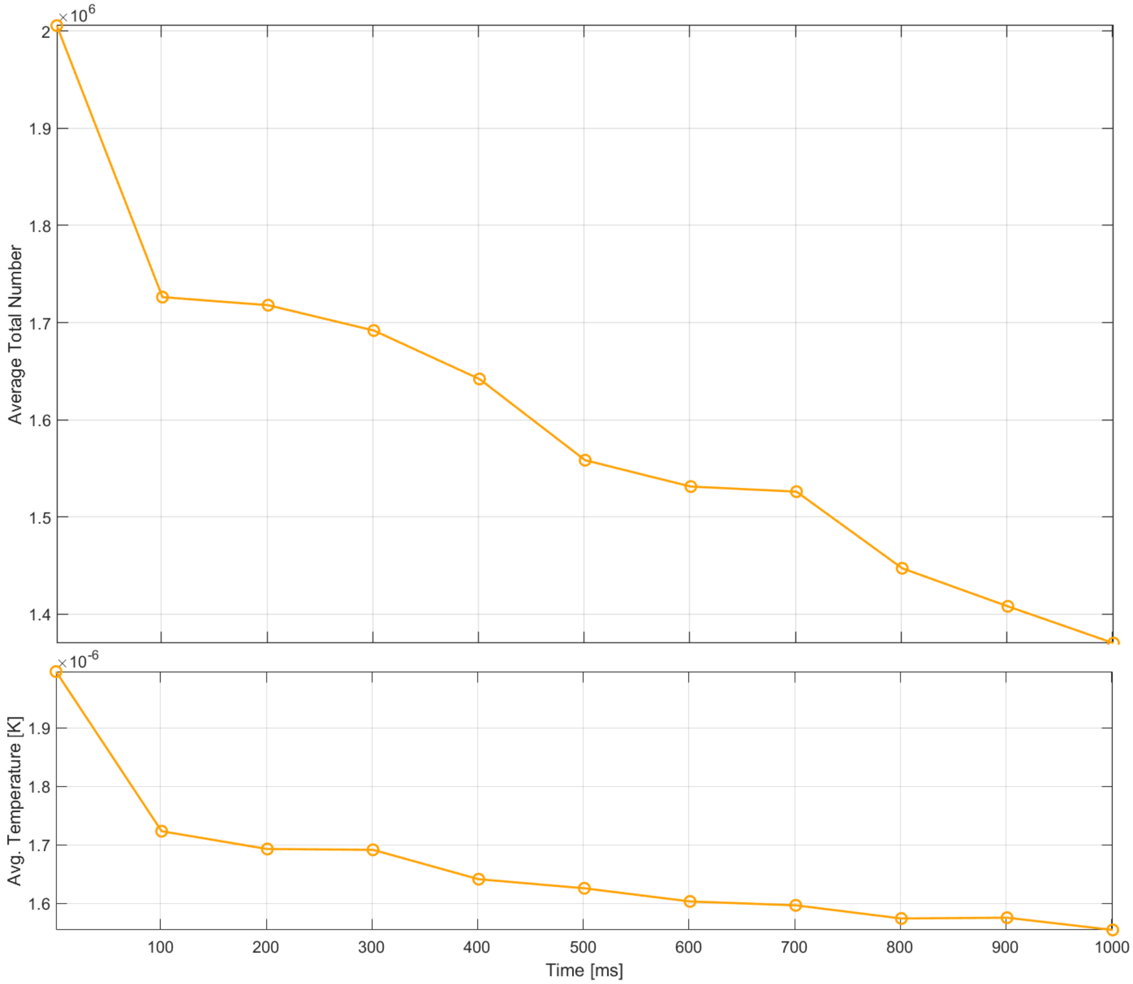

Figure 6.1: Example data of ^{84}Sr confined in the ODT with approximately 1.9 W of power in each of the two beams. Measuring the atom-loss slope after the rapid initial loss at about 150 ms indicates an upper bound of $\gamma_{bg} \sim 0.15\,\mathrm{s}^{-1}$.

Finally, γ_{bg} and R are combined to form an overall one-body rate γ. The saturation intensity for this $\lambda \sim 461\,\mathrm{nm}$ transition is $I_s = \hbar\omega^3\gamma_{atomic}/(12\pi c^2) = 40\ \mathrm{mw/cm}^2$, while the saturation parameter is $s_0 = I/I_s$ [?]. The natural linewidth of the transition is $\gamma_{atomic} = 30.5\,\mathrm{MHz}$. The loss rate is then modeled by:

$$\gamma = R + \gamma_{bg} = \frac{\gamma_{atomic}}{2} \cdot \frac{s_0}{1 + s_0 + \frac{4\Delta^2}{\gamma_{atomic}^2}} + \gamma_{bg} \tag{6.1}$$

For detunings $|\Delta| \gg \gamma_{atomic}$, and neglecting the effect of γ_{bg} based on measured estimates, eq. 6.1 simplifies to:

$$\frac{\gamma}{s_0} \approx 2\pi \left(\frac{\gamma_{atomic}^3}{8\Delta^2} \right) \tag{6.2}$$

where the result has units of s^{-1} for γ_{atomic} and Δ in Hz.

In figure 6.2, scaled one-body rate measurements extracted from multiple exposure time fits to eq. 5.7 are presented. Data for ^{86}Sr are not shown because the strength of the two-body resonances in that isotope required use of the minimum intensity PA light that could be power-controlled (3.6 mw/cm^2) without modifying the PID circuitry. This lead to inconclusive data for γ/s_0 in ^{86}Sr in the form of insignificant variation of the quantity with respect to experimental uncertainties.

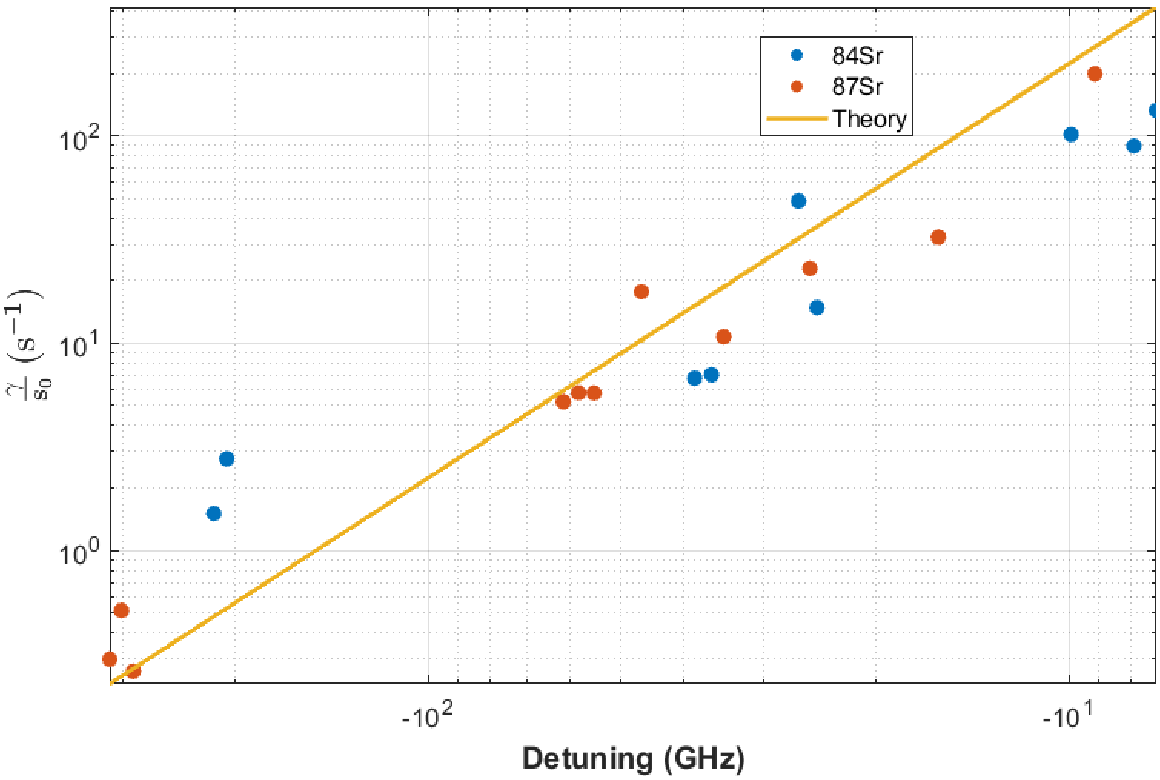

Figure 6.2: Comparison of scaled one-body loss rate (γ/s_0) data and theory for for ^{87}Sr and ^{84}Sr at an intensity of 3.6 mW/cm^2. The data are via fits to eq. 5.7, and eq. 6.2 was used to calculate the prediction curve. Including the effect of γ_{bg} would cause the predicted rate to trend to a constant value of γ_{bg}/s_0 for increasingly negative detunings. The final two ^{84}Sr data points are suggestive of this, though more points would be needed for a definitive measurement.

Table 6.1 summarizes the various gamma symbols in this thesis.

γ_{atomic}	30.5 MHz, ^{1}P$_1$ atomic state natural linewidth
γ	Combined one-body photon scattering loss rate
Γ	Empirical Lorentzian lineshape width
γ_{mol}	$2\,\gamma_{atomic}$, ^{1}S$_0$+^{1}P$_1$ molecular state natural linewidth
$\Gamma(x)$	Gamma function acting on the argument x

Table 6.1: Summary of definitions for the use of the symbol gamma in this thesis.

6.3 Parameter Estimation of PA in a Lattice

Now we turn our attention from one-body to two-body rates; calculating the rate at which atoms in an optical lattice undergo photoassociation. The goal is to demonstrate the value of PA as a doublon-detection mechanism for ^{87}Sr atoms confined in an optical lattice. To make quantitative predictions, we will assume a parameter regime that is readily accessible with common experimental tools. Recall that the recoil energy of an atom (mass m) interacting with a photon (wavelength λ) is $E_R = (\hbar 2\pi)^2/(2m\lambda)$. The assumptions underlying the following calculations are:

- Lattice wavelength $\lambda = 1064\,\mathrm{nm}$
- Lattice depth $V_0 = 16 \times E_R$
- Each lattice site potential is a 3D simple harmonic oscillator
- Atoms in ground electronic and vibrational state, but different spin (m_F)
- Negligible repulsive interactions between atoms on same site

In the tight binding model appropriate for a deep lattice, the bandgap between the ground and first excited band can be approximately related via $\hbar\omega_T \approx \sqrt{4V_0 E_R}$ to the oscillation frequency ω_T of a trapped particle that makes only small excursions from the (approximately harmonic) potential's minima [51]. This frequency can in turn be parameterized by a characteristic harmonic oscillator length scale $a_{HO} = \sqrt{\hbar/(m\omega_T)}$. For such oscillations, $a_{HO} \ll \lambda/2$ and the motional ground-state wave function of an atom leads to a density distribution $n(r)$ for that atom of:

$$n(r) = \left(\frac{1}{\sqrt{\pi a_{HO}^2}}\right)^3 e^{-r^2/a_{HO}^2} \tag{6.3}$$

We can therefore calculate the rate of photoassociation $\dot{N}_{PA}$ under these conditions. The rate is related to the peak (on-PA-resonance) two-body collision rate K_ν via integration over volume:

$$\dot{N}_{PA} = -2K_\nu \int_V n^2(r)dV = \frac{2K_\nu}{(2\pi a_{HO}^2)^{3/2}} \tag{6.4}$$

To determine if $\dot{N}_{PA}$ occurs on an experimentally relevant timescale, we compare it to the rate of off-resonant one-body loss induced by the 461nm PA beam as defined in eq. 6.2. If atoms are photoassociating substantially faster than they are heating up or leaving the trap due to photon scattering, then PA can produce a useful atom-loss signal from which to extract information about doublon dynamics. Here, calculating a_{HO} with the geometric mean of the three ω_T, $(2\pi\, a_{HO}^2)^{3/2} = 1 \times 10^{-14}\,\mathrm{cm}^3$. This characteristic volume can then be used to scale the one-body rate γ, and make comparisons between it and $\dot{N}_{PA}$. For PA of ^{87}Sr at small detunings ($\Delta = -10\,\mathrm{GHz}$), $\dot{N}_{PA} \approx 4 \times \gamma$. For detunings beyond the wave-function node at approximately $\Delta = -300\,\mathrm{GHz}$, the rate comparison is more favorable at $\dot{N}_{PA} \approx 17 \times \gamma$. This is illustrated in figure 6.3.

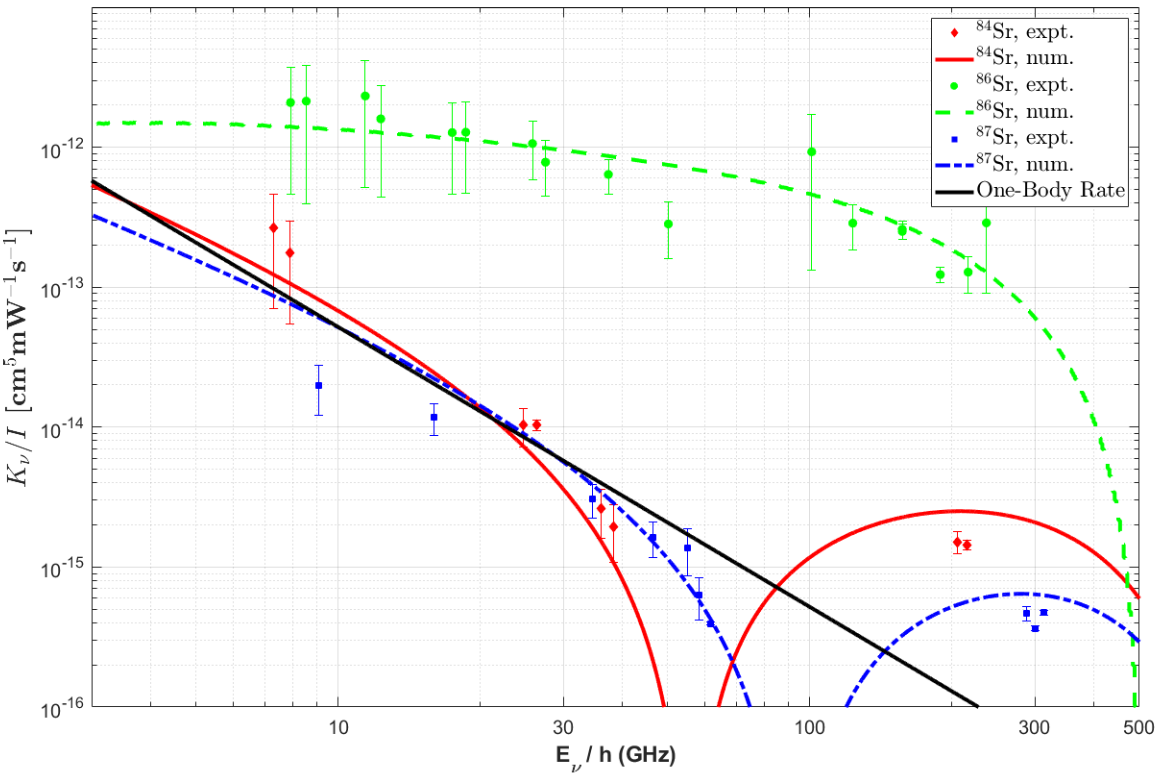

Figure 6.3: Comparison of two-body collision rates (numerical and experiment) for various isotopes with the one-body off-resonant rate γ rate. The latter is calculated using eqn. 6.2 multiplied by the characteristic volume $(2\pi a_{HO}^2)^{3/2}$ and is normalized to intensity. Neglecting the small initial thermal collision energy, $E_\nu/\hbar = |\Delta|$. Note that K values at $E_\nu/\hbar \sim$300 GHz are approximately an order of magnitude larger than the one-body rate, indicating a favorable regime for using PA as a doublon detection tool.

In a deep lattice, the sites are isolated from each other, and there will not be an unlimited reservoir of atoms to collide and photoassociate. Therefore, the two-body collision contribution to the overall atom loss rate will decrease with increasing PA exposure times t. When $t \gg \dot{N}_{PA}^{-1}$, the total loss rate will be dominated by the one-body rate. Other research groups have presented evidence for this, and have explored the lattice-geometry dependence of the effect (see figure 2 of [99]).

6.4 Future Directions

As outlined in the preceding section, using PA as a doublon detection method is a natural extension to the work presented in this thesis. In particular, using the $E_\nu/\hbar \sim 300\,\mathrm{GHz}$ resonances in ^{87}Sr for this application is a compelling first goal. The lab has had limited success with a $\lambda = 532\,\mathrm{nm}$ lattice in the past, however, its eventual use was precluded due to instabilities and heating effects when loading atoms. A new fiber-coupled $\lambda = 1064\,\mathrm{nm}$ lattice is currently under development. A useful experimental milestone for testing this PA-induced doublon removal could be observing the number of remaining atoms as the exposure time of on-resonance PA light is increased. For a deep three-dimensional lattice loaded with atoms such that they are in the Mott insulator regime, the atom number remaining as a function of exposure time can be used to quantify the fraction of doubly occupied sites [99].

Another avenue of possible research could be the investigation of $\Delta \leq -400\,\mathrm{GHz}$ PA resonances and line broadening in that regime that was tentatively attributed to predissociacion. [130].

Lastly, searching for PA resonances using the narrow ($\sim$ 7.5 kHz linewidth) Sr $5s^2\ ^1\mathrm{S}_0$ - $5s5p\,^3\mathrm{P}_1$ transition could be a fruitful research direction. In ^{87}Sr, this linewidth facilitates resolving transitions between individual hyperfine states, as has been observed in fermionic ^{173}Yb [44]. Such resolution is particularly advantageous when combined with spin manipulation among the ten available ^{87}Sr ground-states. Construction of the hardware necessary for such spin manipulation, as well as for spatially separating the states prior to imaging, was the subject of my masters thesis [56]. Spin manipulation in such systems is interesting as as a means of exploring quantum many-body physics and PA has been used to control the interactions between ultracold molecules [21] [46] [10] [104].

The search for PA resonances in ^{87}Sr will be aided by my construction and implementation of an optical phase-locked-loop system for injection locking a lab-built diode laser pair (ECDL + slave for additional power) at a programmable offset from our stable $\sim 689\,\mathrm{nm}$ master laser. The hardware schematic and beat note power spectrum for the system are shown in figures 6.4 and 6.5 respectively.

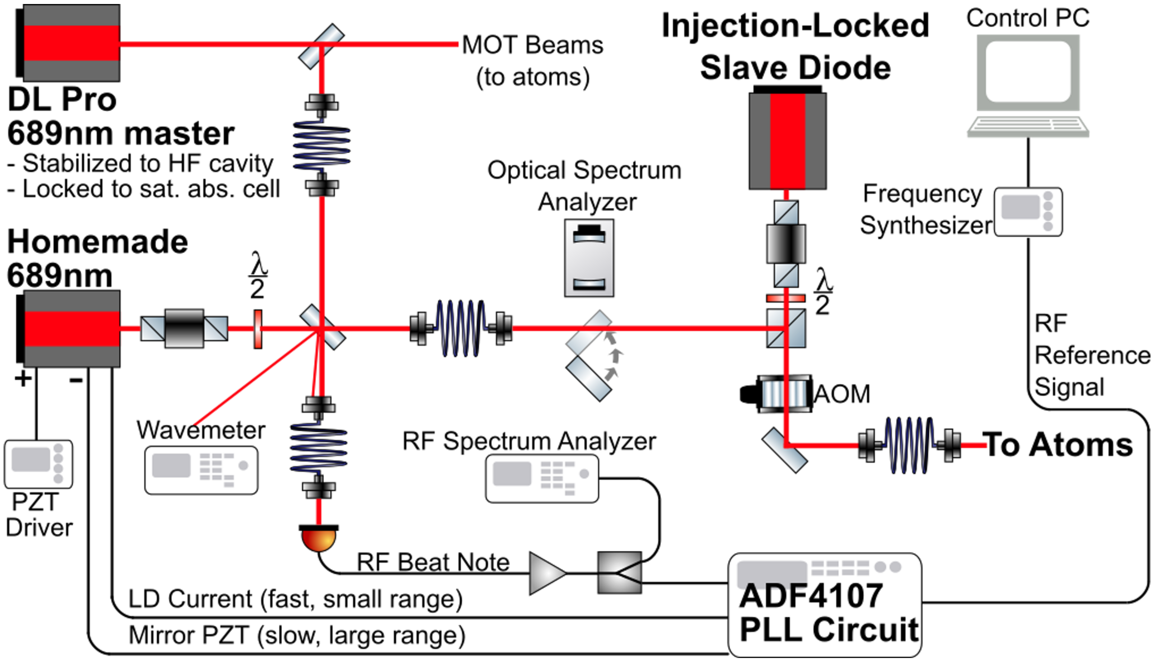

Figure 6.4: Schematic of the $\lambda = 689\,\mathrm{nm}$ optical phase locked loop (OPLL) system constructed as a widely (many GHz) tunable laser source for use in searching for PA resonances in ^{87}Sr on the $^2\,{}^1S_0$- $5s5p\,{}^3P_1$ transition.

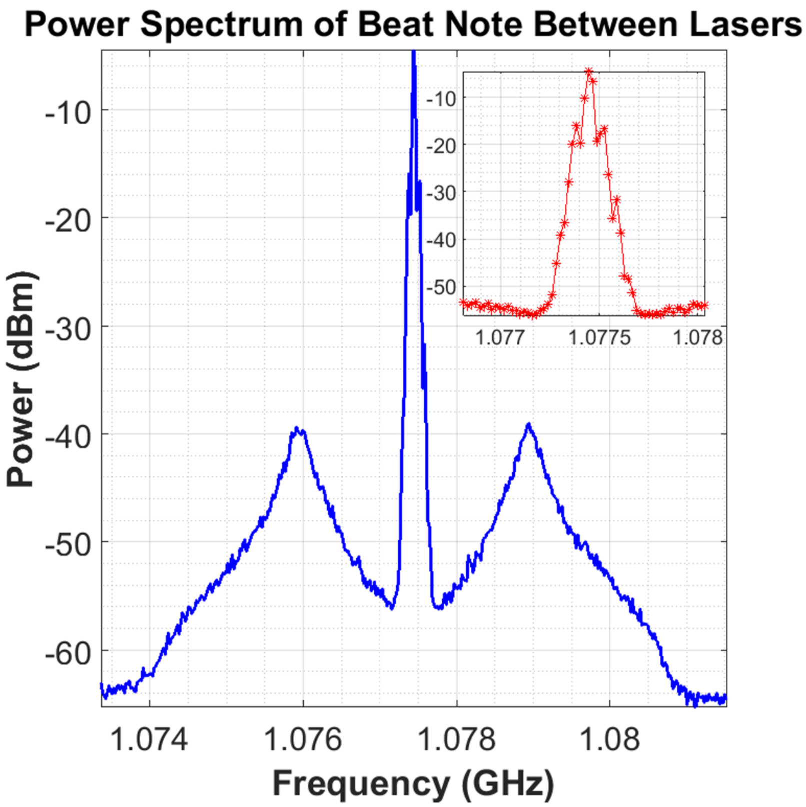

Figure 6.5: Power spectrum of the beat note between the master and locked offset lasers for the system shown schematically in figure 6.4. The inset shows the spectrum around the central carrier frequency.

6.5 Conclusion

In this thesis I have introduced the photoassociation (PA) process, its history as a technique for measuring quantities such as scattering lengths, and provided motivation for our interest in using the technique to detect doubly occupied optical lattice sites ("doublons") in future experiments. I have described our measurements and characterization of PA resonances up to $\sim$ 314 GHz red detuned from the atomic asymptote of the ${}^1\Sigma_u^+$ $5s^2\,{}^1\mathrm{S}_0$ - $5s5p\,{}^1\mathrm{P}_1$ molecular potential in fermionic ^{87}Sr. We performed similar measurements in bosonic ^{86}Sr and ^{84}Sr, and a combined fit to the semiclassical LeRoy-Bernstein model allowed determination of the $^1P_1$ atomic state lifetime and other spectroscopic parameters. Resonance intensities were compared with predictions from Frank-Condon factors using a reflection approximation and numerically-calculated ground-state wavefunction via the best available information about the ground-state potential. To within experimental uncertainties, the resonance frequencies and intensities are reasonably well-described by theoretical predictions. This work will enable accurate prediction of photoassociative transition frequencies and rates for experiments with the strontium isotopes most commonly used in quantum gas experiments. The work also can be used to guide future experiments wishing to implement PA-based doublon detection protocols in Sr, particularly those studying the rich physics introduced by the large nuclear spin of fermionic ^{87}Sr.

References

---

[1] adafruit/Adafruit_mcp4725: MCP4725 12-bit I2C DAC.

[2] Gammon Forum : Electronics : Microprocessors : I2C - Two-Wire Peripheral Interface - for Arduino.

[3] The NIST Reference on Constants, Units, and Uncertainty: Fundamental Physical Constants, Atomic Unit of Electric Polarizability.

[4] J. A. Aman. *Two-photon photoassociative spectroscopy of strontium-86.* PhD Thesis, Rice University, Aug. 2020.

[5] J. A. Aman, J. C. Hill, R. Ding, K. R. A. Hazzard, T. C. Killian, and W. Y. Kon. Photoassociative spectroscopy of a halo molecule in 86Sr. *Physical Review A*, 98(5):053441, Nov. 2018.

[6] S. Amaran, R. Kosloff, M. Tomza, W. Skomorowski, F. Pawłowski, R. Moszynski, L. Rybak, L. Levin, Z. Amitay, J. M. Berglund, D. M. Reich, and C. P. Koch. Femtosecond two-photon photoassociation of hot magnesium atoms: A quantum dynamical study using thermal random phase wavefunctions. *The Journal of Chemical Physics*, 139(16):164124, Oct. 2013.

[7] L. Anderegg, B. L. Augenbraun, Y. Bao, S. Burchesky, L. W. Cheuk, W. Ketterle, and J. M. Doyle. Laser cooling of optically trapped molecules. *Nature Physics*, 14(9):890–893, Sept. 2018.

[8] M. Aymar and O. Dulieu. Calculation of accurate permanent dipole moments of the lowest Sigma+1,3 states of heteronuclear alkali dimers using extended basis sets. *The Journal of Chemical Physics*, 122(20):204302, May 2005.

[9] B. H. Bransden and C. J. Joachain. *Physics of Atoms and Molecules.* Wiley, 1983.

[10] V. Barbé, A. Ciamei, B. Pasquiou, L. Reichsöllner, F. Schreck, P. S. Żuchowski, and J. M. Hutson. Observation of Feshbach resonances between alkali and closed-shell atoms. *Nature Physics*, 14(9):881–884, Sept. 2018.

[11] J. F. Barry, D. J. McCarron, E. B. Norrgard, M. H. Steinecker, and D. DeMille. Magneto-optical trapping of a diatomic molecule. *Nature*, 512(7514):286–289, Aug. 2014.

[12] K. Beloy, A. W. Hauser, A. Borschevsky, V. V. Flambaum, and P. Schwerdtfeger. Effect of alpha variation on the vibrational spectrum of Sr2. *Physical Review A*, 84(6):062114, Dec. 2011.

[13] S. Blatt, T. L. Nicholson, B. J. Bloom, J. R. Williams, J. W. Thomsen, P. S. Julienne, and J. Ye. Measurement of Optical Feshbach Resonances in an Ideal Gas. *Physical Review Letters*, 107(7):073202, Aug. 2011.

[14] C. Boisseau, E. Audouard, J. Vigué, and P. S. Julienne. Reflection approximation in photoassociation spectroscopy. *Physical Review A*, 62(5):052705, Oct. 2000.

[15] M. Borkowski, P. Morzyński, R. Ciuryło, P. S. Julienne, M. Yan, B. J. DeSalvo, and T. C. Killian. Mass scaling and nonadiabatic effects in photoassociation spectroscopy of ultracold strontium atoms. *Physical Review A*, 90(3):032713, Sept. 2014.

[16] br3ttb. br3ttb/Arduino-PID-Library, Apr. 2020.

[17] J. Brown and Alan Carringtion. *Rotational Spectroscopy of Diatomic Molecules.* Cambridge University Press, 2003.

[18] K. Burnett, P. S. Julienne, P. D. Lett, E. Tiesinga, and C. J. Williams. Quantum encounters of the cold kind. *Nature*, 416(6877):225–232, Mar. 2002.

[19] B. A. Bushaw and W. Nörtershäuser. Resonance ionization spectroscopy of stable strontium isotopes and 90Sr via 5s2 1S0→5s5p 1P1→5s5d 1D2→5s11f 1F3→Sr+. *Spectrochimica Acta Part B: Atomic Spectroscopy*, 55(11):1679–1692, Nov. 2000.

[20] F. Camargo. *Rydberg Molecules and Polarons in Ultracold Strontium Gases.* PhD Thesis, Rice University, 2017.

[21] G. Cappellini, L. Livi, L. Franchi, D. Tusi, D. Benedicto Orenes, M. Inguscio, J. Catani, and L. Fallani. Coherent Manipulation of Orbital Feshbach Molecules of Two-Electron Atoms. *Physical Review X*, 9(1):011028, Feb. 2019.

[22] M. A. Cazalilla and A. M. Rey. Ultracold Fermi gases with emergent SU(N) symmetry. *Reports on Progress in Physics*, 77(12):124401, 2014.

[23] R. Ciuryło, E. Tiesinga, and P. S. Julienne. Optical tuning of the scattering length of cold alkaline-earth-metal atoms. *Physical Review A*, 71(3):030701, Mar. 2005.

[24] R. Ciuryło, E. Tiesinga, and P. S. Julienne. Stationary phase approximation for the strength of optical Feshbach resonances. *Physical Review A*, 74(2):022710, Aug. 2006.

[25] D. Comparat. Improved LeRoy–Bernstein near-dissociation expansion formula, and prospect for photoassociation spectroscopy. *The Journal of Chemical Physics*, 120(3):1318–1329, Jan. 2004.

[26] A. Cooper and et al. Alkaline-Earth Atoms in Optical Tweezers. *Physical Review X*, 8(4):041055, Dec. 2018.

[27] R. Côté, A. Dalgarno, Y. Sun, and R. G. Hulet. Photoabsorption by Ultracold Atoms and the Scattering Length. *Physical Review Letters*, 74(18):3581–3584, May 1995.

[28] A. J. Daley. Quantum computing and quantum simulation with group-II atoms. *Quantum Information Processing*, 10(6):865, Sept. 2011.

[29] S. De, U. Dammalapati, K. Jungmann, and L. Willmann. Magneto-optical trapping of barium. *Physical Review A*, 79(4):041402, Apr. 2009.

[30] C. Degenhardt, T. Binnewies, G. Wilpers, U. Sterr, F. Riehle, C. Lisdat, and E. Tiemann. Photoassociation spectroscopy of cold calcium atoms. *Physical Review A*, 67(4):043408, Apr. 2003.

[31] B. J. DeSalvo, M. Yan, P. G. Mickelson, Y. N. Martinez de Escobar, and T. C. Killian. Degenerate Fermi Gas of 87Sr. *Physical Review Letters*, 105(3):030402, July 2010.

[32] A. Devolder, E. Luc-Koenig, O. Atabek, M. Desouter-Lecomte, and O. Dulieu. Proposal for the formation of ultracold deeply bound RbSr dipolar molecules by all-optical methods. *Physical Review A*, 98(5):053411, Nov. 2018.

[33] R. Ding. *Narrow Line Cooling of 84sr.* Master of Science, Rice University, May 2016.

[34] R. Ding. *Spectroscopy of 87Sr Rydberg Atoms and Molecules.* PhD. Thesis, Rice University, Aug. 2019.

[35] E. R. Eliel, W. Hogervorst, T. Olsson, and L. R. Pendrill. High resolution laser spectroscopy of low-lyingp-states in Sr I and Ba I. *Zeitschrift für Physik A Atoms and Nuclei*, 311(1):1–6, Mar. 1983.

[36] C. D. Engle. A Photophonic Instrument Concept to Measure Atmospheric Aerosol Absorption. Master's thesis, Virginia Polytechnic Intitute and State University, Blacksburg, VA, 1982.

[37] S. Engle. *Mitakuye oyasin: We are all related (Lakota Sioux)*. Master of Arts in Teaching, Thesis Project, Christopher Newport University, Newport News, Virginia.

[38] K. Enomoto, M. Kitagawa, S. Tojo, and Y. Takahashi. Hyperfine-Structure-Induced Purely Long-Range Molecules. *Physical Review Letters*, 100(12):123001, Mar. 2008.

[39] M. Fan, C. Holliman, A. Wang, and A. Jayich. Laser Cooling of Radium Ions. *Physical Review Letters*, 122(22):223001, June 2019.

[40] C. Foot. *Atomic Physics*. Oxford University Press, 2008.

[41] R. Grimm, M. Weidemüller, and Y. B. Ovchinnikov. Optical Dipole Traps for Neutral Atoms. *Advances In Atomic, Molecular, and Optical Physics*, 42:95–170, Jan. 2000.

[42] S. Guerandel, T. Badr, M. D. Plimmer, P. Juncar, and M. E. Himbert. Frequency measurement, isotope shift and hyperfine structure of the 4d9 5s2 2D5/2 to 4d106p 2P3/2 transition in atomic silver. *The European Physical Journal D*, 10(1):33–38, Apr. 2000.

[43] A. Guttridge, S. A. Hopkins, M. D. Frye, J. J. McFerran, J. M. Hutson, and S. L. Cornish. Production of ultracold Cs*Yb molecules by photoassociation. *Physical Review A*, 97(6):063414, June 2018.

[44] J. H. Han, J. H. Kang, M. Lee, and Y. Shin. Photoassociation spectroscopy of ultracold 173Yb atoms near the intercombination line. *Physical Review A*, 97(1):013401, Jan. 2018.

[45] A. Heinz, A. Park, N. Šantić, J. Trautmann, S. Porsev, M. Safronova, I. Bloch, and S. Blatt. State-Dependent Optical Lattices for the Strontium Optical Qubit. *Physical Review Letters*, 124(20):203201, May 2020.

[46] M. Hermele, V. Gurarie, and A. M. Rey. Mott Insulators of Ultracold Fermionic Alkaline Earth Atoms: Underconstrained Magnetism and Chiral Spin Liquid. *Physical Review Letters*, 103(13):135301, Sept. 2009.

[47] G. Herzberg. *Molecular Spectra and Molecular Structure: Spectra of Diatomic Molecules*. Robert E. Krieger Publishing Company, 2 edition, 1989.

[48] G. Herzberg and E. Teller. Schwingungsstruktur der Electronenübergange bei mehratomigen Molekülen. *Z. Phys. Chemie*, B21:410–446, 1933.

[49] J. C. Hill, W. Huie, P. Lunia, J. D. Whalen, S. K. Kanungo, Y. Lu, and T. C. Killian. Photoassociative spectroscopy of 87Sr. *Physical Review A*, 103(2):023111, Feb. 2021.

[50] W. Huie. *Refinement of the strontium molecular potential by numerical computation of bound states.* Bachelors Thesis, Rice University, Apr. 2020.

[51] D. Jaksch and P. Zoller. The cold atom Hubbard toolbox. *Annals of Physics*, 315(1):52–79, Jan. 2005.

[52] B. B. Jensen, H. Ming, P. G. Westergaard, K. Gunnarsson, M. H. Madsen, A. Brusch, J. Hald, and J. W. Thomsen. Experimental Determination of the 24Mg (3s3p) 3P_2 Lifetime. *Physical Review Letters*, 107(11):113001, Sept. 2011.

[53] B. R. Johnson. New numerical methods applied to solving the one-dimensional eigenvalue problem. *The Journal of Chemical Physics*, 67(9):4086–4093, Nov. 1977.

[54] K. M. Jones, E. Tiesinga, P. D. Lett, and P. S. Julienne. Ultracold photoassociation spectroscopy: Long-range molecules and atomic scattering. *Reviews of Modern Physics*, 78(2):483–535, May 2006.

[55] K. M. Jones, E. Tiesinga, P. D. Lett, and P. S. Julienne. Ultracold photoassociation spectroscopy: Long-range molecules and atomic scattering. *Reviews of Modern Physics*, 78(2):483–535, May 2006.

[56] Joshua C Hill. *Design and Construction of an Apparatus for Optically Pumping 87Sr.* Master of Science, Rice University, Aug. 2017.

[57] P. Julienne. Cold binary atomic collisions in a light field. *Journal of Research of the National Institute of Standards and Technology*, 101(4):487, July 1996.

[58] T. C. Killian, S. Stellmer, and F. Schreck. Degenerate Quantum Gases of Strontium. In K. Madison, K. Bongs, L. Carr, A. M. Rey, and H. Zhai, editors, *Annual Review of Cold Atoms and Molecules*, volume 2. World Scientific Publishing Company, May 2014.

[59] M. Kitagawa, K. Enomoto, K. Kasa, Y. Takahashi, R. Ciuryło, P. Naidon, and P. S. Julienne. Two-color photoassociation spectroscopy of ytterbium atoms and the precise determinations of s-wave scattering lengths. *Physical Review A*, 77(1):012719, Jan. 2008.

[60] W. Y. Kon, J. A. Aman, J. C. Hill, T. C. Killian, and K. R. A. Hazzard. High-intensity two-frequency photoassociation spectroscopy of a weakly bound molecular state: Theory and experiment. *Physical Review A*, 100(1):013408, July 2019.

[61] S. Kotochigova, T. Zelevinsky, and J. Ye. Prospects for application of ultracold Sr2 molecules in precision measurements. *Physical Review A*, 79(1):012504, Jan. 2009.

[62] A. Kulosa, D. Fim, K. Zipfel, S. Rühmann, S. Sauer, N. Jha, K. Gibble, W. Ertmer, E. Rasel, M. Safronova, U. Safronova, and S. Porsev. Towards a Mg Lattice Clock: Observation of the 1S0 - 3P0 Transition and Determination of the Magic Wavelength. *Physical Review Letters*, 115(24):240801, Dec. 2015.

[63] A. D. Lange, K. Pilch, A. Prantner, F. Ferlaino, B. Engeser, H.-C. Nägerl, R. Grimm, and C. Chin. Determination of atomic scattering lengths from measurements of molecular binding energies near Feshbach resonances. *Physical Review A*, 79(1):013622, Jan. 2009.

[64] K. P. Lawley. *Advances in Chemical Physics, Molecular Scattering: Physical and Chemical Applications*, volume 30. 1975.

[65] R. J. Le Roy and R. B. Bernstein. Dissociation energies and long-range potentials of diatomic molecules from vibrational spacings: The halogens. *Journal of Molecular Spectroscopy*, 37(1):109–130, Jan. 1971.

[66] R. J. LeRoy and R. B. Bernstein. Dissociation Energy and Long-Range Potential of Diatomic Molecules from Vibrational Spacings of Higher Levels. *The Journal of Chemical Physics*, 52(8):3869–3879, Apr. 1970.

[67] L. R. Liu, J. D. Hood, Y. Yu, J. T. Zhang, N. R. Hutzler, T. Rosenband, and K.-K. Ni. Building one molecule from a reservoir of two atoms. *Science*, 360(6391):900–903, May 2018.

[68] A. D. Ludlow. *The Strontium Optical Lattice Clock: Optical Spectroscopy with Sub-Hertz Accuracy.* PhD. Thesis, University of Colorado, Boulder, 2008.

[69] M. Machholm, P. S. Julienne, and K.-A. Suominen. Calculations of collisions between cold alkaline-earth-metal atoms in a weak laser field. *Physical Review A*, 64(3):033425, Aug. 2001.

[70] L. P. Maguire, S. Szilagyi, and R. E. Scholten. High performance laser shutter using a hard disk drive voice-coil actuator. *Review of Scientific Instruments*, 75(9):3077–3079, Sept. 2004.

[71] M. Mamaev, R. Blatt, J. Ye, and A. Rey. Cluster State Generation with Spin-Orbit Coupled Fermionic Atoms in Optical Lattices. *Physical Review Letters*, 122(16):160402, Apr. 2019.

[72] Y. N. Martinez de Escobar, P. G. Mickelson, P. Pellegrini, S. B. Nagel, A. Traverso, M. Yan, R. Côté, and T. C. Killian. Two-photon photoassociative spectroscopy of ultracold 88Sr. *Physical Review A*, 78(6):062708, Dec. 2008.

[73] D. McCarron. Laser cooling and trapping molecules. *Journal of Physics B: Atomic, Molecular and Optical Physics*, 51(21):212001, Oct. 2018.

[74] B. H. McGuyer, M. McDonald, G. Z. Iwata, M. G. Tarallo, A. T. Grier, F. Apfelbeck, and T. Zelevinsky. High-precision spectroscopy of ultracold molecules in an optical lattice. *New Journal of Physics*, 17(5):055004, May 2015.

[75] B. H. McGuyer, M. McDonald, G. Z. Iwata, M. G. Tarallo, W. Skomorowski, R. Moszynski, and T. Zelevinsky. Precise study of asymptotic physics with subradiant ultracold molecules. *Nature Physics*, 11(1):32–36, Jan. 2015.

[76] W. J. Meath. Retarded Interaction Energies between Like Atoms in Different Energy States. *The Journal of Chemical Physics*, 48(1):227–235, Jan. 1968.

[77] H. J. Metcalf and P. v. d. Straten. Laser Cooling and Trapping of Neutral Atoms. In *The Optics Encyclopedia*. 2007.

[78] P. Mickelson. *Trapping and Evaporation of 87Sr and 88Sr Mixtures*. PhD thesis, Rice University, Houston, Texas, USA, Apr. 2010.

[79] P. G. Mickelson. *Trapping and Evaporation of 87Sr and 88Sr Mixtures*. PhD Thesis, Rice University, Houston, Texas, USA, 2010.

[80] P. G. Mickelson, Y. N. M. d. Escobar, P. Anzel, B. J. DeSalvo, S. B. Nagel, A. J. Traverso, M. Yan, and T. C. Killian. Repumping and spectroscopy of laser-cooled Sr atoms using the (5s5p)3P2–(5s4d)3D2transition. *Journal of Physics B: Atomic, Molecular and Optical Physics*, 42(23):235001, Nov. 2009.

[81] P. G. Mickelson, Y. N. Martinez, A. D. Saenz, S. B. Nagel, Y. C. Chen, T. C. Killian, P. Pellegrini, and R. Côté. Spectroscopic Determination of the S-Wave Scattering Lengths of 86Sr and 88Sr. *Physical Review Letters*, 95(22):223002, Nov. 2005.

[82] J. Mitroy, M. S. Safronova, and C. W. Clark. Theory and applications of atomic and ionic polarizabilities. *Journal of Physics B: Atomic, Molecular and Optical Physics*, 43(20):202001, Oct. 2010.

[83] H. Miyake, N. C. Pisenti, P. K. Elgee, A. Sitaram, and G. K. Campbell. Isotope-shift spectroscopy of the 1S0-3P1 and 1S0-3P0 transitions in strontium. *Physical Review Research*, 1(3):033113, Nov. 2019.

[84] T. Mukaiyama, H. Katori, T. Ido, Y. Li, and M. Kuwata-Gonokami. Recoil-Limited Laser Cooling of 87Sr Atoms near the Fermi Temperature. *Physical Review Letters*, 90(11):113002, Mar. 2003.

[85] S. B. Nagel, P. G. Mickelson, A. D. Saenz, Y. N. Martinez, Y. C. Chen, T. C. Killian, P. Pellegrini, and R. Côté. Photoassociative Spectroscopy at Long Range in Ultracold Strontium. *Physical Review Letters*, 94(8):083004, Mar. 2005.

[86] S. B. Nagel, C. E. Simien, S. Laha, P. Gupta, V. S. Ashoka, and T. C. Killian. Magnetic trapping of metastable 3P2 atomic strontium. *Physical Review A*, 67(1):011401, Jan. 2003.

[87] W. Nagourney. *Quantum Electronics for Atomic Physics*. Oxford University Press, Oxford ; New York, June 2010.

[88] K.-K. Ni, S. Ospelkaus, M. H. G. de Miranda, A. Pe'er, B. Neyenhuis, J. J. Zirbel, S. Kotochigova, P. S. Julienne, D. S. Jin, and J. Ye. A High Phase-Space-Density Gas of Polar Molecules. *Science*, 322(5899):231–235, Oct. 2008.

[89] M. A. Norcia, A. W. Young, W. J. Eckner, E. Oelker, J. Ye, and A. M. Kaufman. Seconds-scale coherence on an optical clock transition in a tweezer array. *Science*, Sept. 2019.

[90] O. Onishchenko, S. Pyatchenkov, A. Urech, C.-C. Chen, S. Bennetts, G. A. Siviloglou, and F. Schreck. Frequency of the ultranarrow 1S0-3P2 transition in 87Sr. *Physical Review A*, 99(5):052503, May 2019.

[91] H. Ozawa, S. Taie, Y. Takasu, and Y. Takahashi. Antiferromagnetic Spin Correlation of SU(N Fermi Gas in an Optical Superlattice. *Physical Review Letters*, 121(22):225303, Nov. 2018.

[92] Peter Atkins and Ronald Friedman. *Molecular Quantum Mechanics*. Oxford University Press, 4th edition, 2005.

[93] W. D. Phillips. Nobel Lecture: Laser cooling and trapping of neutral atoms. *Reviews of Modern Physics*, 70(3):721, 1998.

[94] G. Pichler, S. Milosevic, D. Viza, and R. Beuc. Diffuse bands in the visible absorption spectra of dense alkali vapours. *Journal of Physics B: Atomic and Molecular Physics*, 16(24):4619–4631, Dec. 1983.

[95] S. G. Porsev, M. S. Safronova, and C. W. Clark. Relativistic calculations of C6 and C8 coefficients for strontium dimers. *Physical Review A*, 90(5):052715, Nov. 2014.

[96] O. N. Prudnikov, D. V. Brazhnikov, A. V. Taichenachev, V. I. Yudin, A. E. Bonert, R. Y. Il'enkov, and A. N. Goncharov. Quantum treatment of two-stage sub-Doppler laser cooling of magnesium atoms. *Physical Review A*, 92(6):063413, Dec. 2015.

[97] D. Redmayne. Infinite Sample-and-Hold Outperforms Many Legacy Sample-and-Hold Amplifiers | Analog Devices.

[98] B. J. Reschovsky, B. P. Ruzic, H. Miyake, N. C. Pisenti, P. S. Julienne, and G. K. Campbell. Narrow-line photoassociation spectroscopy and mass-scaling of

bosonic strontium. *arXiv:1808.06507 [cond-mat, physics:physics, physics:quant-ph]*, Oct. 2018.

[99] T. Rom, T. Best, O. Mandel, A. Widera, M. Greiner, T. W. Hänsch, and I. Bloch. State Selective Production of Molecules in Optical Lattices. *Physical Review Letters*, 93(7):073002, Aug. 2004.

[100] A. D. Saenz. *461nm Laser For Studies In Ultracold Neutral Strontium.* PhD Thesis, Rice University, July 2005.

[101] J. E. Sansonetti and G. Nave. Wavelengths, Transition Probabilities, and Energy Levels for the Spectrum of Neutral Strontium (SrI). *Journal of Physical and Chemical Reference Data*, 39(3):033103, Sept. 2010.

[102] F. Schäfer, T. Fukuhara, S. Sugawa, Y. Takasu, and Y. Takahashi. Tools for quantum simulation with ultracold atoms in optical lattices. *Nature Reviews Physics*, 2(8):411–425, Aug. 2020.

[103] C. E. Simien. *422 nm Laser.* PhD Thesis, Rice University, Sept. 2004.

[104] L. Sonderhouse, C. Sanner, R. B. Hutson, A. Goban, T. Bilitewski, L. Yan, W. R. Milner, A. M. Rey, and J. Ye. Thermodynamics of a deeply degenerate SU(N)-symmetric Fermi gas. *Nature Physics*, 16(12):1216–1221, Dec. 2020.

[105] A. Stein, H. Knöckel, and E. Tiemann. Fourier-transform spectroscopy of Sr 2 and revised ground-state potential. *Physical Review A*, 78(4):042508, Oct. 2008.

[106] A. Stein, H. Knöckel, and E. Tiemann. The 1S+1S asymptote of Sr2 studied by Fourier-transform spectroscopy. *The European Physical Journal D*, 57(2):171–177, Apr. 2010.

[107] S. Stellmer. *Degenerate quantum gases of strontium.* PhD. Thesis, University of Innsbruck, Innsbruck, Austria, 2013.

[108] S. Stellmer, B. Pasquiou, R. Grimm, and F. Schreck. Creation of Ultracold Sr2 Molecules in the Electronic Ground State. *Physical Review Letters*, 109(11):115302, Sept. 2012.

[109] S. Stellmer, M. K. Tey, R. Grimm, and F. Schreck. Bose-Einstein condensation of Sr 86. *Physical Review A*, 82(4):041602, Oct. 2010.

[110] W. C. Stwalley, Y.-H. Uang, and G. Pichler. Pure Long-Range Molecules. *Physical Review Letters*, 41(17):1164–1167, Oct. 1978.

[111] S. Sugawa, K. Inaba, S. Taie, R. Yamazaki, M. Yamashita, and Y. Takahashi. Interaction and filling-induced quantum phases of dual Mott insulators of bosons and fermions. *Nature Physics*, 7(8):642–648, Aug. 2011.

[112] S. Taie, R. Yamazaki, S. Sugawa, and Y. Takahashi. An SU(6) Mott insulator of an atomic Fermi gas realized by large-spin Pomeranchuk cooling. *Nature Physics*, 8(11):825–830, Nov. 2012.

[113] Y. Takasu, K. Komori, K. Honda, M. Kumakura, T. Yabuzaki, and Y. Takahashi. Photoassociation Spectroscopy of Laser-Cooled Ytterbium Atoms. *Physical Review Letters*, 93(12):123202, Sept. 2004.

[114] O. Thomas, C. Lippe, T. Eichert, and H. Ott. Experimental realization of a Rydberg optical Feshbach resonance in a quantum many-body system. *Nature Communications*, 9(1):2238, June 2018.

[115] J. D. Thompson, T. G. Tiecke, N. P. d. Leon, J. Feist, A. V. Akimov, M. Gullans, A. S. Zibrov, V. Vuletić, and M. D. Lukin. Coupling a Single Trapped Atom to a Nanoscale Optical Cavity. *Science*, 340(6137):1202–1205, June 2013.

[116] H. R. Thorsheim, J. Weiner, and P. S. Julienne. Laser-induced photoassociation of ultracold sodium atoms. *Physical Review Letters*, 58(23):2420–2423, June 1987.

[117] E. Tiemann, M. Kahmann, E. Pachomow, F. Riehle, and U. Sterr. Nonlinear Zeeman effect in photoassociation spectra of 40Ca near the 3P1+1S0 asymptote. *Physical Review A*, 92(2):023419, Aug. 2015.

[118] E. Tiesinga, C. J. Williams, P. S. Julienne, K. Jones, P. D. Lett, and W. D. Phillips. A Spectroscopic Determination of Scattering Lengths for Sodium Atom Collisions. 101:505, Jan. 1996.

[119] S. Tojo, M. Kitagawa, K. Enomoto, Y. Kato, Y. Takasu, M. Kumakura, and Y. Takahashi. High-Resolution Photoassociation Spectroscopy of Ultracold Ytterbium Atoms by Using the Intercombination Transition. *Physical Review Letters*, 96(15):153201, Apr. 2006.

[120] J. Ulmanis, J. Deiglmayr, M. Repp, R. Wester, and M. Weidemüller. Ultracold Molecules Formed by Photoassociation: Heteronuclear Dimers, Inelastic Collisions, and Interactions with Ultrashort Laser Pulses. *Chemical Reviews*, 112(9):4890–4927, Sept. 2012.

[121] F. Vogt, C. Grain, T. Nazarova, U. Sterr, F. Riehle, C. Lisdat, and E. Tiemann. Determination of the calcium ground state scattering length by photoassociation spectroscopy at large detunings. *The European Physical Journal D*, 44(1):73–79, July 2007.

[122] D. Wang, J. Qi, M. F. Stone, O. Nikolayeva, H. Wang, B. Hattaway, S. D. Gensemer, P. L. Gould, E. E. Eyler, and W. C. Stwalley. Photoassociative Production and Trapping of Ultracold KRb Molecules. *Physical Review Letters*, 93(24):243005, Dec. 2004.

[123] J. Weiner, V. S. Bagnato, S. Zilio, and P. S. Julienne. Experiments and theory in cold and ultracold collisions. *Reviews of Modern Physics*, 71(1):1–85, Jan. 1999.

[124] J. D. Whalen, S. K. Kanungo, R. Ding, M. Wagner, R. Schmidt, H. R. Sadeghpour, S. Yoshida, J. Burgdörfer, F. B. Dunning, and T. Killian. Probing nonlocal spatial correlations in quantum gases with ultra-long-range Rydberg molecules. *Physical Review A*, 100(1):011402, July 2019.

[125] F.-F. Wu, Y.-B. Tang, T.-Y. Shi, and L.-Y. Tang. Magic-intensity trapping of the Mg lattice clock with light shift suppressed below 10e-19. *Physical Review A*, 101(5):053414, May 2020.

[126] L. Xia, L. A. Zundel, J. Carrasquilla, A. Reinhard, J. M. Wilson, M. Rigol, and D. S. Weiss. Quantum distillation and confinement of vacancies in a doublon sea. *Nature Physics*, 11(4):316–320, Apr. 2015.

[127] M. Yan, R. Chakraborty, A. Mazurenko, P. G. Mickelson, Y. N. M. de Escobar, B. J. DeSalvo, and T. C. Killian. Numerical modeling of collisional dynamics of Sr in an optical dipole trap. *Physical Review A*, 83(3):032705, Mar. 2011.

[128] M. Yan, B. J. DeSalvo, Y. Huang, P. Naidon, and T. C. Killian. Rabi Oscillations between Atomic and Molecular Condensates Driven with Coherent One-Color Photoassociation. *Physical Review Letters*, 111(15):150402, Oct. 2013.

[129] M. Yan, B. J. DeSalvo, B. Ramachandhran, H. Pu, and T. C. Killian. Controlling Condensate Collapse and Expansion with an Optical Feshbach Resonance. *Physical Review Letters*, 110(12):123201, Mar. 2013.

[130] M. Yasuda, T. Kishimoto, M. Takamoto, and H. Katori. Photoassociation spectroscopy of 88Sr, Reconstruction of the wave function near the last node. *Physical Review A*, 73(1):011403, Jan. 2006.

[131] A. L. M. Zanelatto, E. M. S. Ribeiro, and R. d. J. Napolitano. Scattering lengths for Li–Cs, Na–Cs, K–Cs, and Rb–Cs ultracold collisions. *The Journal of Chemical Physics*, 123(1):014311, July 2005.

[132] T. Zelevinsky, M. M. Boyd, A. D. Ludlow, T. Ido, J. Ye, R. Ciuryło, P. Naidon, and P. S. Julienne. Narrow Line Photoassociation in an Optical Lattice. *Physical Review Letters*, 96(20):203201, May 2006.

[133] G. Zinner, T. Binnewies, F. Riehle, and E. Tiemann. Photoassociation of Cold Ca Atoms. *Physical Review Letters*, 85(11):2292–2295, Sept. 2000.

Appendix A

Appendix

A.1 Arduino General-Purpose Slow PID Lock

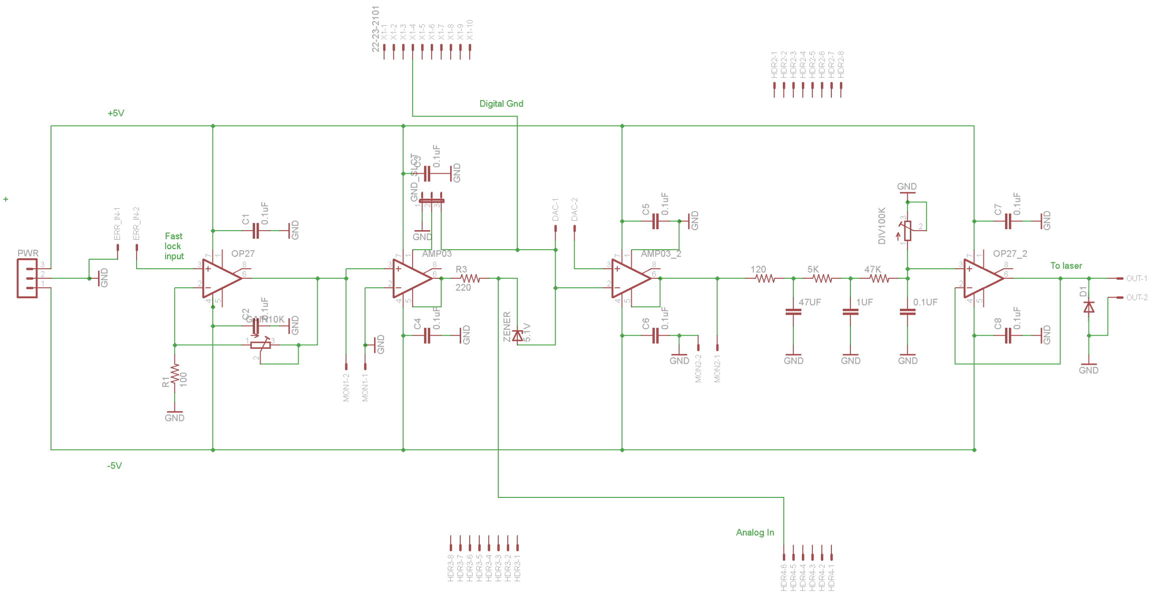

Figure A.1: Circuit schematic of the Arduino slow lock. Input to the board begins on the left, the rows of pins along the top and bottom are the header pins to mate with those of the Arduino, the MPC4725 DAC ground and output connects via wires in the center of the diagram, and the signal exits the board towards the instrumentation on the far right of the diagram.

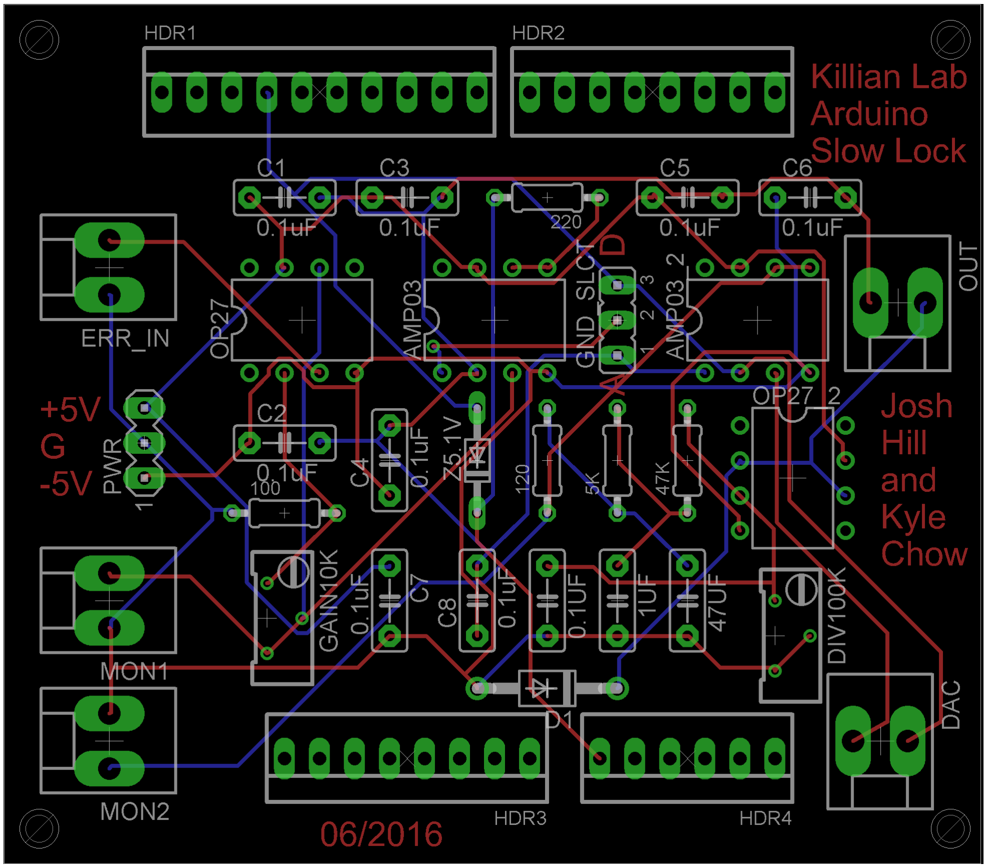

Figure A.2: Physical layout of traces and components on the printed circuit board (PCB). Extra solder pads and through-holes are included for bringing wires into and out of the board from BNC cables.

Listing A.1: Slow_Lock.ino

```
/*****************************************************************
  MCP4725 Slow Lock
  Josh Hill
  Feb. 2018

This sketch reads in 0-5V on the Arduino's A0 analog input pin, calculates an error signal, and puts out a voltage to correct for it.
Lock/unlock is controlled by a switch attached between 3 digital pins. Pin D12 reads the state, from either Low (D10) or High (D11).
Debug = 1 tells it to output to the serial (usb) port, information about the lock.

```

```
This particular code is for the 689nm slow lock. I removed the enable/disable portion of the code and the related physical switch, since we will have a
switch going between the Arduino and an external pot (to control the set point) anyway.

The input to this circuit is 0-4V. The Arduio can accept 0-5V but something is happening at the A0 input pin that makes it only want to go to 4V. Perhaps
an imput impedence issue on the Arduino analog input pin. Scale the input voltage as necessary for any new implementation.

*/

// Libraries
//-------
#include <Wire.h>                    //Include the Wire library to talk I2C
#include <LiquidCrystal.h>           // Talk to the LCD
#include <PID_v1.h>                  // Main PID Library
#define MCP4725_ADDR 0x60            //This is the I2C Address of the MCP4725 (Sparkfun MCP4725A0), by default (A0 pulled to GND).

// DEFINITIONS (GLOBAL)
//-------
double setpoint = 1550;              // Manual setpoint for lock. Max is 2^12 = 4095 =5V. Note that small offsets in the electronics ...
                                     // ... make this value not exactly equal to the 2V ADC integer (1639) corresponding to zero input volts.
float Kp        = 0.2;               // Tuning Parameters (Recall, floats can be < 1).
float Ki        = 1;
float Kd        = 0;
boolean debug   = 0;                 // Print to serial console if true. Leave this off during when not debugging.
double output, input, error, pot;
int int_output;
const int sampleRate = 1;            // How often, in milliseconds, the PID will be evaluated.
boolean  initLCDclearBool = 1;
boolean  lockLCDBool = 1;
LiquidCrystal lcd(7, 8, 5, 4, 3, 2); //Define which Arduino pins do what for the LCD.
PID myPID(&input, &output, &setpoint, Kp, Ki, Kd, 1, DIRECT, &error); // PID function instance called myPID.
```

```
//////////////////////////////////////////////////////////////// <-- Denotes serial debugging code not part of lock.
const long serialPing = 5000; //This determines how often we ping our loop. Serial pingback interval in milliseconds
unsigned long now = 0; //This variable is used to keep track of time.
unsigned long lastMessage = 0; //This keeps track of when our loop last spoke to serial.// last message timestamp.
//////////////////////////////////////////////////////////////



void setup()
{
  lcd.begin(16, 2); //LCD's number of (columns,rows)

  ////////////////////////////////////////////////////////////////
  if ( debug ) {
    Serial.begin(9600);
    Serial.println("Begin");
    lastMessage = millis(); // Timestamp of when we last sent a message over the serial line.
  }
  ////////////////////////////////////////////////////////////////

  input = map(analogRead(A0), 0, 1023, 0, 4095); // Maps the 10-bit input onto a 12-bit number.

  Wire.begin();
  TWBR = 12; // Two wire bit register. Controls the I2C protocol speed (SCL).

    myPID.SetSampleTime(sampleRate);
  myPID.SetOutputLimits(0, 4095);  // Default output is {0,255} for PWM.

  //POWER PIN SETUP
  //-------
  pinMode(A2, OUTPUT);
  pinMode(A3, OUTPUT);
  digitalWrite(A2, LOW);             //Set A2 as GND
  digitalWrite(A3, HIGH);            //Set A3 as Vcc, will power the MCP4725
}



void loop()
  {

  pinMode(13, INPUT);
```

```
  boolean lockBool = digitalRead(13);            // Manual or Arduino control Boolean signal from physical switch.
  input = map(analogRead(A0), 0, 1023, 0, 4095); // Reads in a value (0-1023) depending on the voltage on A0 (0-5V), and maps that number to {0,4095}.
  pot = map(analogRead(A1), 0, 1023, 0, 4095);   // Reads in value from manual tuning pot



  if ( lockBool ==  0) // Switched to manual control
  {
    myPID.SetMode(MANUAL);        // Turns off the PID Controller
    output = pot;                 // Important to set the PID output equal to that of the manual pot even while the Arduino is not being used...
                                  // ... because oterwise when the Arduino is engaged, it jumps to some other value it had been calculating and kicks the system.
    error = 0;                    // Important to force the error to zero while the Arduino is not being used, otherwise it will be accumulating an error based on the input...
                                  // ... and that error will cause the output to change dramatically (kick) when the Arduino is engaged.

     if (millis() % 500 == 0) // Only print to the screen if the time is modulo whatever number is after the "%" symbol.
    {
      // Clear LCD if this is the first run or if the lock was engaged previously
      if (initLCDclearBool == 1 || lockLCDBool == 1)
      {
        lcd.clear();
        initLCDclearBool = 0;
        lockLCDBool = 0;
      }
      lcd.print ("Lock Disabled");
      lcd.setCursor(0, 1);
      lcd.print("Out(V)="); lcd.print(round(output)/4095.0 * 385.0 , 0); lcd.print("/385");
      lcd.setCursor(0, 0);
    }
    }
  else                  // Switched to Ardunio control
  {

    myPID.SetMode(AUTOMATIC); //Turns on PID controller, important to get rid of jump in output
```

```

    //CALCULATE PID OUTPUT
    //-------
    myPID.Compute();                 // The PID algorithm itself, calculates output.
    int_output = round(output);


    //DAC OUTPUT
    //-------
    Wire.beginTransmission(MCP4725_ADDR);
    Wire.write(64);                 // command to update the DAC (64 in decimal = The start byte for the DAC).

    // I2C uses 8-bit (one byte) packets, so we have to break up the 16-bit integer into two bytes, then
    // mask off the first 4 bits (15 in binary is 00001111) because the MPC4725 only can take 12 bits.
    // Most significant bit is furthest to the left. The bits are shuffled around so that when
    // the Wire.write I2C command writes its 8-bit chunk it will chop off nothing important.

    Wire.write(int_output >> 4);        // Grab the 8 most significant bits first.  (D11.D10.D9.D8.D7.D6.D5.D4)
    // The >> and << are bit shift operators.
    // They shift the in the left operand to be shifted left or right by the number of positions in the right operand.
    // The bits at the end (left or right) that are shifted, go away.
    Wire.write((int_output & 15) << 4); // the 4 least significant bits. (D3.D2.D1.D0.x.x.x.x).
    Wire.endTransmission();

    if (millis() % 500 == 0) // Only print to the screen if the time is modulo whatever number is after the "%" symbol.
    {
      if (lockLCDBool == 0)
      {
        lcd.clear();
        lockLCDBool = 1;
      }

      lcd.print ("In(V) = "); lcd.print(5/819.0 * input - 10 , 2);
      lcd.setCursor(0, 1);
      lcd.print("Out(V)="); lcd.print(int_output/4095.0 * 385.0 , 0); lcd.print("/385");
      lcd.setCursor(0, 0);
    }

}

```

```
    ////////////////////////////////////////////////////////////////
    if ( debug ) {
      now = millis();
      if (now - lastMessage > serialPing) { //Put what you want to print out, in this loop.
        Serial.println("---------------------------------------------------");
        Serial.print("\n");
        Serial.print(" Lock State = ");
        Serial.println("Locked");
        Serial.print("\n");
        Serial.print(" Setpoint (12 bit) = ");
        Serial.println(setpoint);
        Serial.print("\n");
        Serial.print(" Input Value = ");
        Serial.println(input);
        Serial.print("\n");
        Serial.print(" PID Function Output = ");
        Serial.println(output);
        Serial.print("\n");
        Serial.print(" Integer Output = ");
        Serial.println(int_output);
        Serial.print("\n");
        Serial.print(" Digital Pin ");
        Serial.println(digitalRead(13));
        Serial.print("\n");
        Serial.print(" Error ");
        Serial.println(error);
        Serial.print("\n");
        Serial.print(" Pot ");
        Serial.println(pot);
        Serial.print("\n");
        lastMessage = now;
      }
    }
    ////////////////////////////////////////////////////////////////
  }
```

The code in listings A.2 and A.3 are the changes made to the C++ PID library files. The line number at which a change occurred is listed to the left of the change, prior to the “)”.

Listing A.2: PID_v1.h Changes

```
20)PID(double*, double*, double*,        // * constructor.  links the PID to the Input, Output, and error
21) double, double, double, int, int, double*);//   Setpoint.  Initial tuning parameters are also set here. (overload for specifying proportional mode)
```

```
22)    PID(double*, double*, double*,        // * constructor. links the PID to the Input, Output, and
23)         double, double, double, int, double*);     //   Setpoint. Initial tuning parameters are also set here
24)
25)    void SetMode(int Mode);               // * sets PID to either Manual (0) or Auto (non-0)
26)
27)    bool Compute();                       // * performs the PID calculation.  it should be called every time loop() cycles. ON/OFF and calculation frequency can be set using SetMode SetSampleTime respectively
28)    void SetOutputLimits(double, double); // * clamps the output to a specific range. 0-255 by default, but it's likely the user will want to change this depending on the application


30)  void SetTunings(double, double,       // * While most users will set the tunings once in the
31)                     double);                       //   constructor, this function gives the user the option of changing tunings during runtime for Adaptive control
32)    void SetTunings(double, double,       // * overload for specifying proportional mode
33)                     double, int);
34)
35)     void SetControllerDirection(int);         // * Sets the Direction, or "Action" of the controller. DIRECT means the output will increase when error is positive. REVERSE means the opposite.  it's very unlikely that this will be needed once it is set in the constructor.
36)void SetSampleTime(int);              // * sets the frequency, in Milliseconds, with which the PID calculation is performed. default is 100

58)
```

Listing A.3: PID_v1.cpp Changes

```
20)PID::PID(double* Input, double* Output, double* Setpoint,
21)       double Kp, double Ki, double Kd, int POn, int ControllerDirection, double* Error)
22){
23)     myError  = Error;

29) PID::SetOutputLimits(0, 255);//default output limit corresponds to the arduino pwm limits

43)PID::PID(double* Input, double* Output, double* Setpoint,
44)        double Kp, double Ki, double Kd, int ControllerDirection, double* Error)
45)    :PID::PID(Input, Output, Setpoint, Kp, Ki, Kd, P_ON_E,
```

```
   ControllerDirection , Error)

87) *myError  = error;
```

A.2 MOT Cavity Additional Information

A.2.1 461nm MOT Cavity Temperature Controller

We used one implementation of the Arduino slow lock to stabilize the temperature of our blue ($^1S_0$ - $^1P_1$) MOT doubling cavity. The cavity suffers from instability in the amount of output 461 nm power, drifting by tens of mW on an hour timescale. In an attempt to debug this drift, we bypassed the existing Wavelength-brand temperature controller with a slow lock feeding back to the cavity thermoelectric device (TEC). The lock functioned as expected, and was able to control the temperature of the cavity well. Unfortunately, there was no improvement in the power output stability of the cavity with either the Arduino lock or a commercial Newport Lightwave LDT5525 temperature controller. The ultimate cause of the drifts was later determined to be pointing stability of the 922 nm input light, and poor cavity mode-matching. During this work, we uncovered some details about the Wavelength temperature controller, and thermistor calibrations. These details are as follows.

The MOT cavity temperature controller is a Wavelength-brand HTC-3000 device. Looking at the DIP switches, one can see that it is configured for bipolar operation, and that the thermistor bias current is 100 μA. We often monitor the output voltage of these devices. To quantify and convert the voltages we see to meaningful temperatures, I wrote code to plot these quantities for a 100μA bias current through a Thorlabs 10 kΩ thermistor. The thermistor coefficients are from the Thorlabs TH10K datasheet.

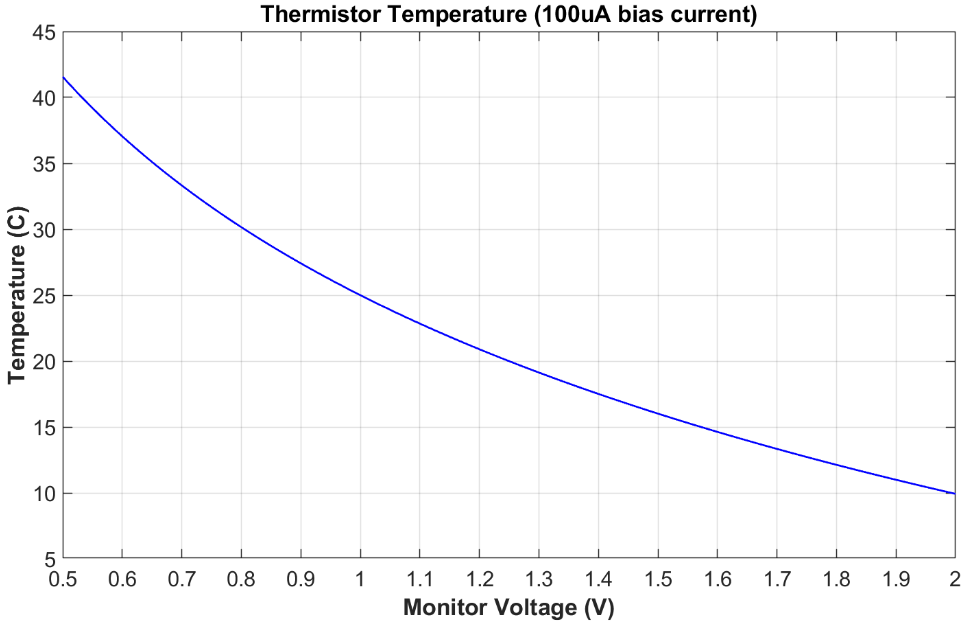

Figure A.3: Plot for converting the voltage across a Thorlabs 10 kΩ thermistor with 100 μA of bias current through it, to a temperature. Thermistor coefficients from the TH10K datasheet.

Listing A.4: Thermistor Voltage to Temperature Matlab Code

```
Vin = linspace(0.5,2,1000);

%Calculation of temperature from resistance measurement through thermistor (assumed to be a Thorlabs 10k).
%Formula from datasheet for temperature as function of resistance
I_bias      = 0.0001;% Bias current in A through thermistor from Wavelength Controller
Rt          = Vin./I_bias; %Calculated thermistor resistance
R25         = 10000; % 25 C resistance of the thermistor
log_ratio   = log(Rt./R25);

a     = 3.3540170E-3;% Empirical coefficients from Thorlabs datasheet
b     = 2.5617244E-4;
c     = 2.1400943E-6;
d     = -7.2405219E-8;

denom = a + b*log_ratio + c*log_ratio.^2 + d*log_ratio.^3;
T     = denom.^-1;  % Temp in Kelvin
TC    = T - 273.15; % Temp in Celsius


```

```
figure
plot(Vin,TC,'b-','LineWidth',2)
set(gca,'XTick',0.5:0.1:2);

str   = sprintf('Thermistor Temperature (100uA bias current)');
title(str);
ylabel('Temperature (C)','FontSize',15,'FontWeight','bold');
xlabel('Monitor Voltage (V)','FontSize',15,'FontWeight','bold');
grid on
set(gca,'FontSize',23)
set(gca,'LineWidth',1)
```

While each of the two doubling systems has its own optimization peculiarities, daily small tweaks to the input 922 nm alignment, cavity temperature, and TA current are required to maintain adequate power levels. The Zeeman cavity is the more stable of the pair, and adjusting the current of the TA associated with it is typically sufficient to maintain the desired power. The MOT cavity is more fickle. Cavity temperature is another parameter available for tuning that I have found to impact the daily power output. At the time of writing, a stable mode with approximately 110 mW of 461 nm power could be achieved at around 18.25 C (1.350 V on the monitor BNC). Going warmer in temperature, the 461 nm power decreases monotonically. Going colder increases the power up to a point, then the cavity jumps to a lower-power mode.

A.2.2 Possible Future MOT TA Fiber Hardware

Although not yet implemented at the the time of writing, we also considered hardware that could be used to eliminate the ~ 2 m free-space path between the MOT/Zeeman IR AOM, and the MOT tapered amplifier. Reducing this path length by fiber coupling the beam could present a potential source of great improvement if alignment from scratch is necessary. For that reason, the information gathered is documented here.

To begin, it is helpful to have an idea of the beam-mode that would best match to the TA. This can be obtained by observing the light propagating backwards out of the input of the un-seeded TA. The poor mode quality (see figure A.5) of such a beam is typical for tapered amplifiers.

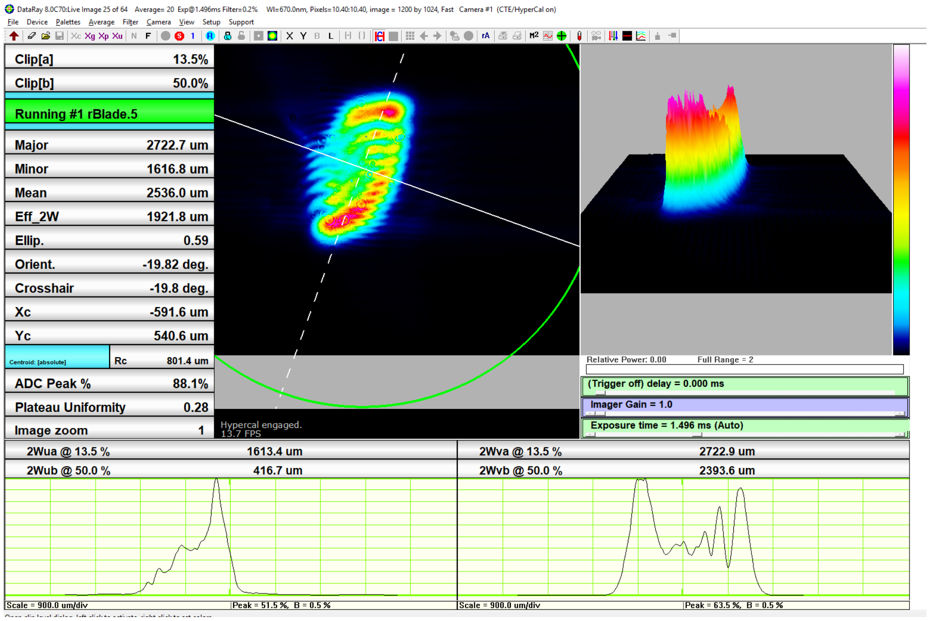

DataRay 8.0C70:Live Image 25 of 64 Average= 20 Exp@1.496ms Filter=0.2% Wl=670.0nm, Pixels=10.40:10.40, image = 1200 by 1024, Fast Camera #1 (CTE/HyperCal on)

Clip[a] 13.5%
Clip[b] 50.0%
Running #1 rBlade.5
Major 2722.7 um
Minor 1616.8 um
Mean 2536.0 um
Eff_2W 1921.8 um
Ellip. 0.59
Orient. -19.82 deg.
Crosshair -19.8 deg.
Xc -591.6 um
Yc 540.6 um
Centroid: [absolute]
Rc 801.4 um
ADC Peak % 88.1%
Plateau Uniformity 0.28
Image zoom 1

Hypercal engaged.
13.7 FPS

Relative Power: 0.00 Full Range = 2
(Trigger off) delay = 0.000 ms
Imager Gain = 1.0
Exposure time = 1.496 ms (Auto)

2Wua @ 13.5 % 1613.4 um
2Wub @ 50.0 % 416.7 um
2Wva @ 13.5 % 2722.9 um
2Wvb @ 50.0 % 2393.6 um

Scale = 900.0 um/div
Peak = 51.5 %, B = 0.5 %
Scale = 900.0 um/div
Peak = 63.5 %, B = 0.5 %

Figure A.4: Sample image of beam coming backwards out of the input of the unseeded TA. Detector at 41.5 cm from the TA's input face.

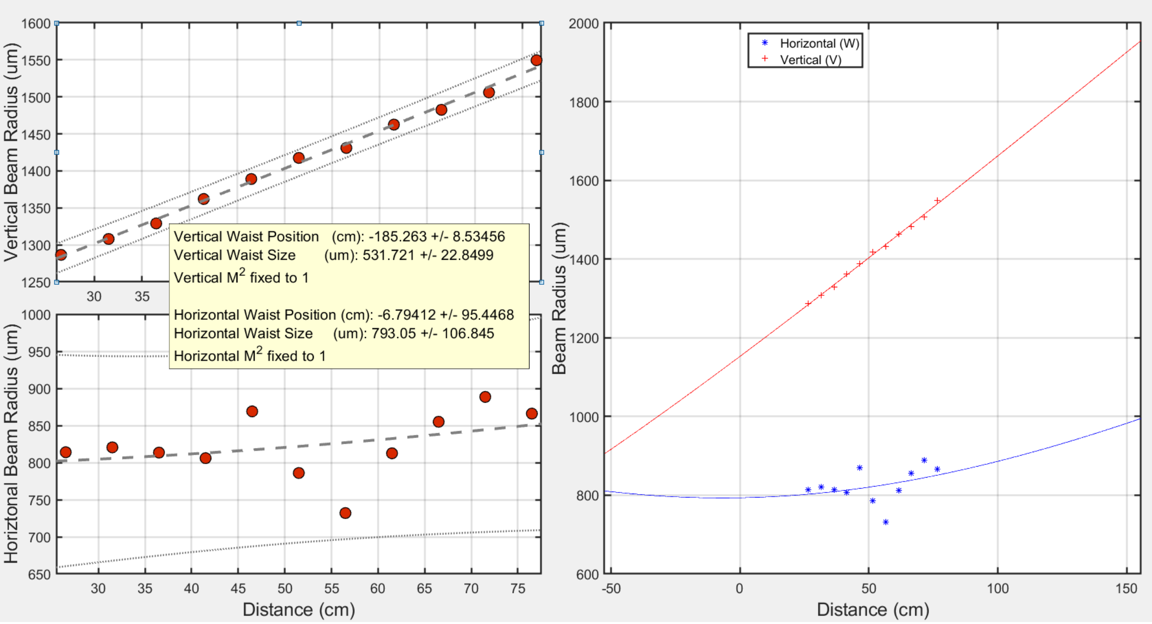

Figure A.5: Beam profile of beam coming backwards out of the input of the un-seeded MOT TA. Zero distance is the TA's input face. Increasing distance is towards the ECDL head.

Figure A.6 is a profile of the zeroth order (MOT path) beam from the AOM that splits the Zeeman and MOT 922 nm light paths. There are no lenses in this measurement. Zero distance is the first face of the AOM that the beam encounters after leaving the 922 nm fiber output launcher. In the current configuration, the beam propagates through a +500 mm spherical lens and across the optical table towards the MOT TA.

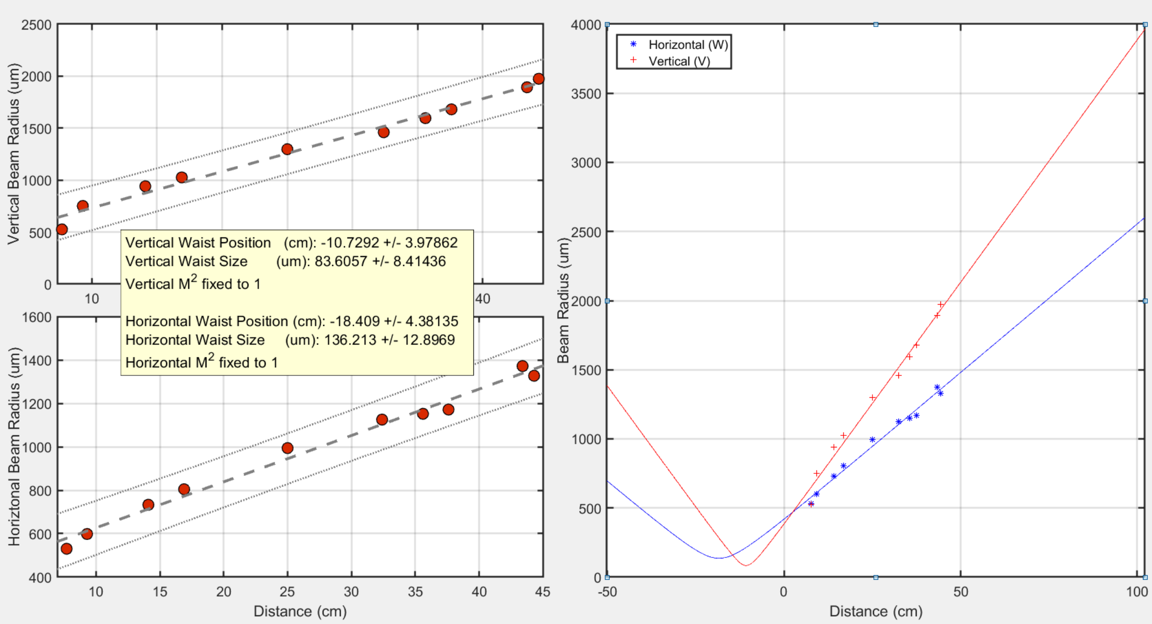

Vertical Waist Position (cm): -10.7292 +/- 3.97862
Vertical Waist Size (um): 83.6057 +/- 8.41436
Vertical M^2 fixed to 1

Horizontal Waist Position (cm): -18.409 +/- 4.38135
Horizontal Waist Size (um): 136.213 +/- 12.8969
Horizontal M^2 fixed to 1

Figure A.6: Beam profile of the zeroth order (MOT path) beam from the AOM that splits the Zeeman and MOT 922nm light paths. Zero distance is the first face of the AOM that the beam encounters after leaving the 922nm fiber output launcher. This profile is after the AOM and includes no lenses.

Armed with a profile of the beam that would be coupled into a fiber bridging the existing $\sim$ 2m path length, and a rough idea of what beam would match the TA (fig. A.5), we can make hardware (collimator and fiber) choices. These choices are aided by a theoretical approximation of a fiber input collimator's output (or optimal input) beam diameter d based on the light wavelength λ, the focal length of the collimating lens f, and the $1/e^2$ mode field diameter MFD of the fiber:

$$d \approx 4\lambda \frac{f}{\pi \cdot MFD} \tag{A.1}$$

The beam coming from the AOM is conveniently accessible at about 25cm from the AOM (reference location defined in caption of fig. A.6), where the beam has sizes of $\omega_H = 1$mm and $\omega_V = 1.25$mm. Propagating this beam through a f=+500mm horizontal cylindrical lens at 25cm, and a f=+300mm vertical cylindrical lens at 44.5cm will roughly match (d ∼2.4mm) a Thorlabs brand PM780-HP (NA=0.12, MFD=5.3um) fiber mated to a CFC-11X-B adjustable input collimator (f=11mm, MFD=4.3um, θ_{div}=0.022°). Further adjustments are possible via the distance between the fiber tip and collimator's internal lens, this is a sufficient starting point should the decision to fiber couple the beam be made in the future.

For the fiber output (towards MOT TA), a Thorlabs brand CFC-8X-B collimator (f=7.5mm, MFD=4.3um, θ_{div}=0.033°) will produce d ≈1.6mm. This will match the smaller of the two axes of the TA beam, and cylindrical lenses can be used to optimize the larger axis.

A.3 Infinite Sample and Hold Circuit

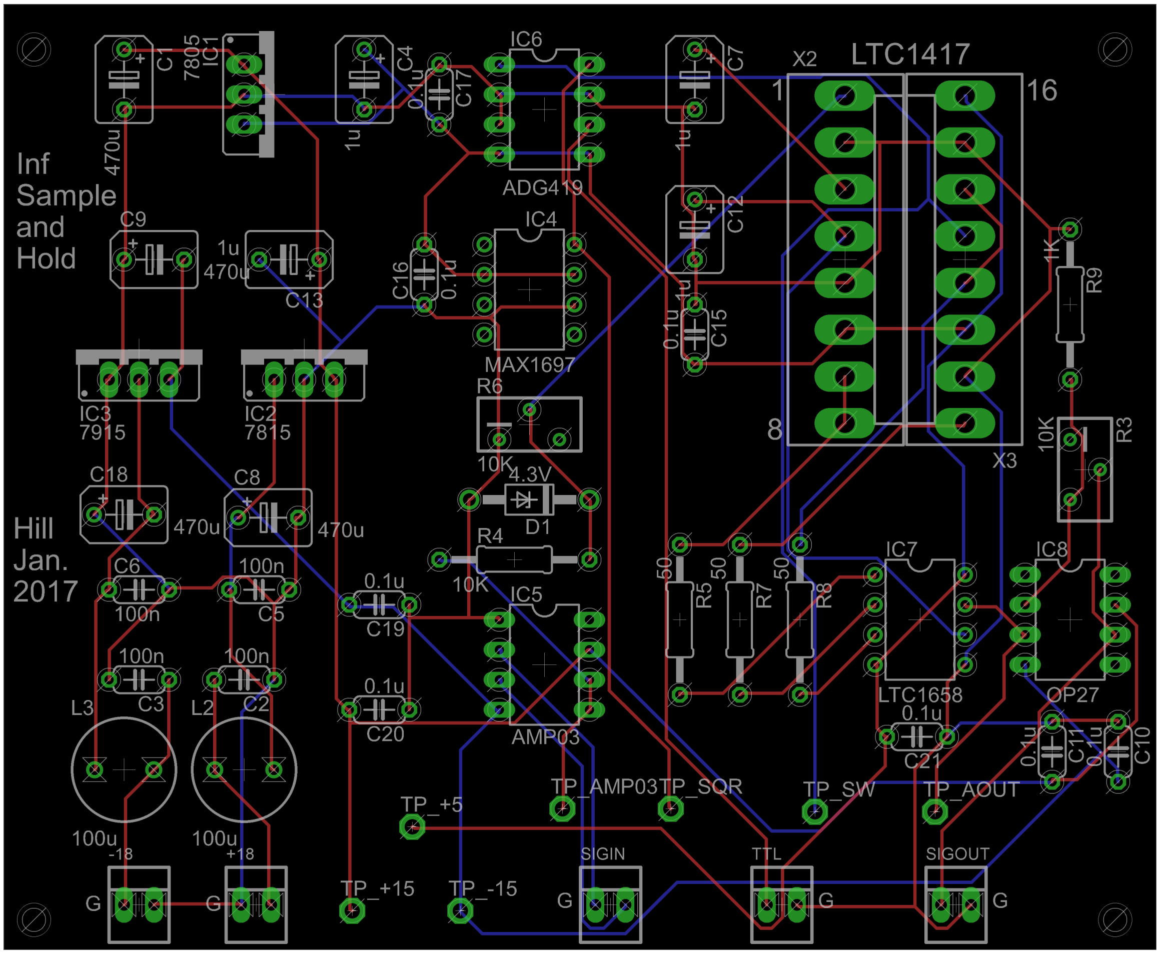

Figure A.7: Printed circuit board for the infinite sample and hold device. Note that the LCT1417 did not have a through-hole option at this time, so required a breakout board to convert the surface-mount SSOP16 package to DIP.

A.4 National Instruments c-RIO FPGA Experimental Control

Since its inception, the Neutral apparatus has used *Spincore Pulseblaster* units to distribute its TTL experimental timing signals, and hand-wired individual ADG149 chips for logic. As the system grew, we saw a need for more input/outputs channels, as well as the ability to develop more complex and flexible logic configurations. The National Instruments (NI) cRIO-9063 system is a real-time control unit with an embedded FPGA controller. We chose the system for the control-system upgrade because of its versatility and ease of configuration. Furthermore, NI supports a LabView FPGA programming environment which was more readily integrated into our existing control routines and a low-level FPGA language would have been[4]. The unit has four expansion bays, into which various modules (e.g. motor driving, analog and digital IO, counters, etc.) can be inserted. We chose to begin with with two modules one with 32 digital in/out channels and one with 16 analog output channels.

The high-density channels on the modules are individually broken out via adapters with screw-terminals to convenient BNC connectors on a rack-mountable front panel. The 16 analog output channels do so after passing through OPA633 buffer amplifiers. The buffers not only increase the current output capability of each channel, they serve as a layer of protection. It is preferential to have an easily replaced DIP chip in-line during possible over-current or high transient voltage situations rather than the bare module channel themselves. Additionally, there is a 1MHz low-pass filter on each channel for noise reduction. Note that all 32 digital channels share a common ground.

The initial implementation has only used a fraction of the system's capabilities, focusing on simple boolean logic, TTL-controled switching, static analog voltages, and linear ramps. The two remaining expansion bays and existing codebase serve as a strong platform to expand future capabilities as needed such as more complicated timing or data-acquisition routines.

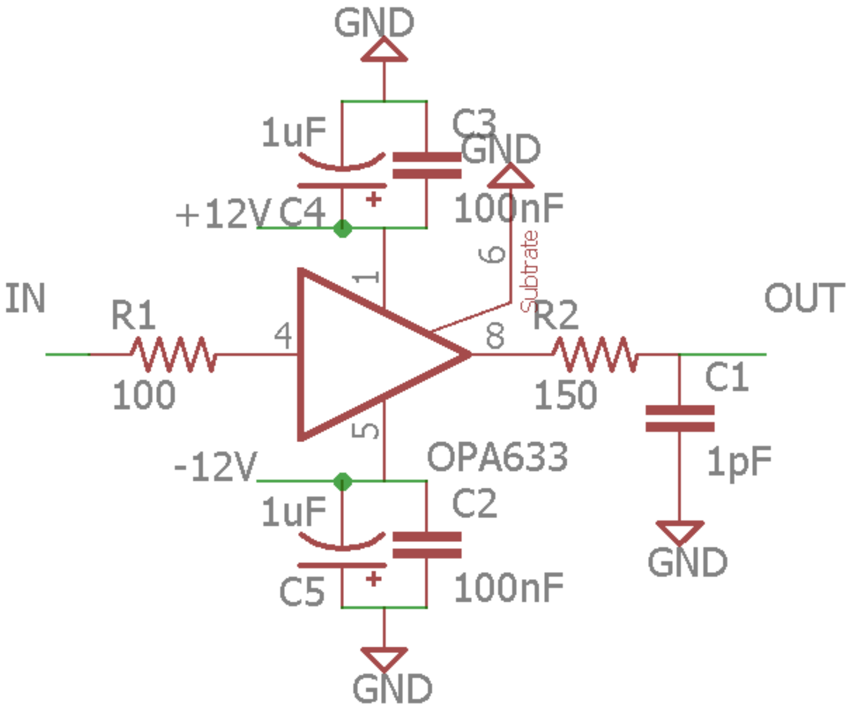

Figure A.8: Schematic of the buffer amplifier in-line on each of the 16 analog output channels. The buffer serves as a current source, and as a means of protecting the cRIO module.

A.5 PA Excitation Laser

Optimizing the PA excitation laser for peak power output can be a challenge given the number of parameters involved. A typical optimization routine involves peaking up the IR light from the diode into the TA, and from there into the doubling cavity. Cleaning the internal mirrors had little effect on the power except for one notable exception. Cleaning the incoupling mirror of the SHG cavity (possibly for the first time ever) increased the visible wavelength optical power output by 30%. The general technique is to observe the 922 nm SHG cavity mode spectrum, and maximize the difference between the dominant mode, and all others. The overall power output is also moderately sensitive to the TA and SHG temperatures, as controlled by their respective electronics modules.

When struggling to lock the cavity (or to lock to the intensity peak value), the PDH-PID parameters can be adjusted to best match the ideal PDH error signal shape given in the user manual. The PID electronics module also has a minimum intensity setting potentiometer that can be used to prevent the laser from locking to bad modes. If set too high, however, this can prevent it from locking to anything at all. The potentiometer is accessible from the side of the PID module when removed or mounted in an extension bracket.

For reference, a typical parameter set is as follows. Note that it can be challenging to reoptimize back to a given power after long periods of downtime (system completely off).

Master Oscillator Operating Current (mA)	70
Master Oscillator Threshold Current (mA)	26
922 nm Power After Diode (mW)	27
922 nm Power After TA (mW)	325
922 nm Power Into SHG Cavity (mW)	315
461 nm Power Output (mW)	63
Master Oscillator TEC Setpoint (C)	20.3
SHG Crystal TEC Setpoint (C)	32.2
TA Current Setpoint (mA)	1841

Table A.1: Summary reference of PA laser parameters.

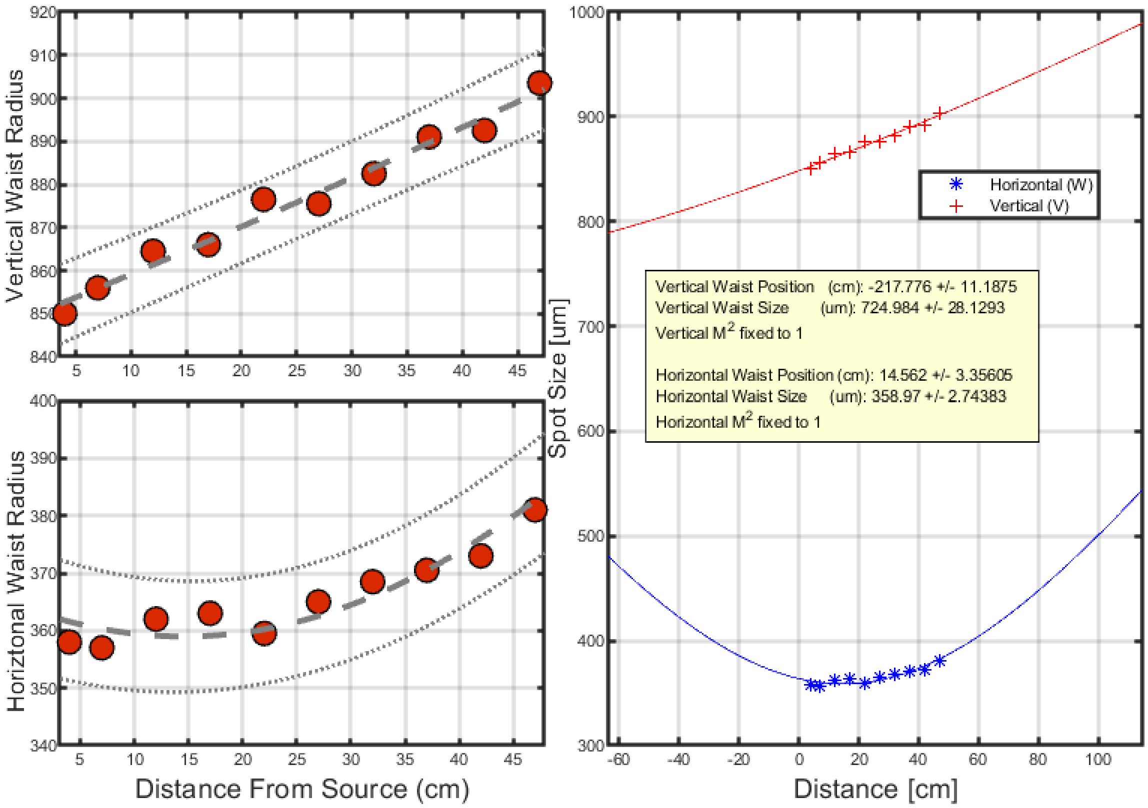

Figure A.9: Profile of PA laser's bare output. Zero distance in the plot corresponds to the output aperture of the laser's external housing, after which there are no optical elements included.

A.6 Shutter Driver

Mechanical shutters constructed from spinning-disk hard drives are a popular tool in atomic physics because of their simplicity, low-cost, and robustness [70]. For the PA excitation beam, I made an equally cheap and simple driver that actuates the shutter bidirectionally depending on the state of a TTL input. The shutter is capable of operating on a ms timescale, limited by the drive, and is based on the IXYS IXDF604PI MOSFET driver integrated circuit. Up to the operating limits of the shutter's coil, adjusting the drive current via the power resistor or supply voltage tunes the speed of operation. Decoupling capacitors and further noise isolation circuitry can be included, though these were not necessary for this application. The integrated circuit draws at most 10 μA from the TTL line.

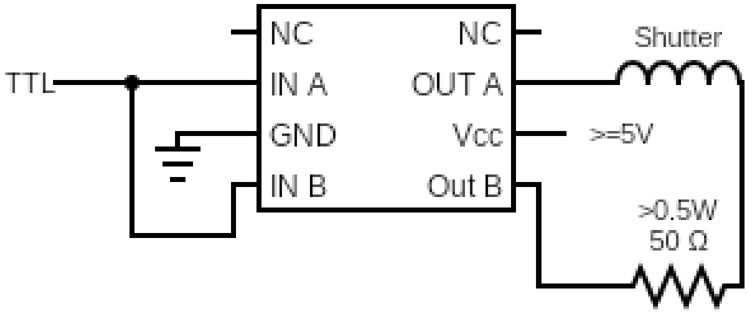

Figure A.10: Circuit diagram for a shutter driver base on the IXYS IXDF604PI MOSFET driver integrated circuit.